

# Seismic wave detectability on Venus using ground deformation sensors, infrasound sensors on balloons and airglow imagers

Raphael F. Garcia<sup>1</sup>, Iris van Zelst<sup>2</sup>, Taichi Kawamura<sup>3</sup>, Sven Peter Näsholm<sup>4</sup>, Anna Catherine Horleston<sup>5</sup>, Sara Klaasen<sup>6</sup>, Maxence Lefevre<sup>7</sup>, Céline Marie Solberg<sup>8</sup>, Krystyna T. Smolinski<sup>9</sup>, Ana-Catalina Plesa<sup>2</sup>, Quentin Brissaud<sup>10</sup>, Julia S. Maia<sup>11</sup>, Simon C. Stähler<sup>12</sup>, Philippe Lognonné<sup>13</sup>, Mark Paul Panning<sup>14</sup>, Anna Gülcher<sup>15</sup>, Richard Ghail<sup>16</sup>, and Barbara De Toffoli<sup>17</sup>

<sup>1</sup>Institut Supérieur de l'Aéronautique et de l'Espace, ISAE-SUPAERO

<sup>2</sup>German Aerospace Center

<sup>3</sup>Université Paris Cité, Institut de physique du globe de Paris, CNRS

<sup>4</sup>NORSAR

<sup>5</sup>University of Bristol

<sup>6</sup>Swiss Federal Institute of Technology in Zurich

<sup>7</sup>Sorbonne Université

<sup>8</sup>NOSAR

<sup>9</sup>ETH Zürich

<sup>10</sup>Norwegian Seismic Array (NORSAR)

<sup>11</sup>DLR DLR Institute of Planetary Research

<sup>12</sup>Eidgenössische Technische Hochschule Zürich

<sup>13</sup>Université Paris Cité, Institute de physique de globe de Paris, CNRS

<sup>14</sup>JPL

<sup>15</sup>California Institute of Technology; NASA Jet Propulsion Laboratory; ETH Zürich

<sup>16</sup>Royal Holloway University of London

<sup>17</sup>INAF-IAPS

April 11, 2024

## Abstract

The relatively unconstrained internal structure of Venus is a missing piece in our understanding of the Solar System formation and evolution. To determine the seismic structure of Venus' interior, the detection of seismic waves generated by venusquakes is crucial, as recently shown by the new seismic and geodetic constraints on Mars' interior obtained by the InSight mission. In the next decades multiple missions will fly to Venus to explore its tectonic and volcanic activity, but they will not be able to conclusively report on seismicity or detect actual seismic waves.

Looking towards the next fleet of Venus missions in the future, various concepts to measure seismic waves have already been explored in the past decades. These detection methods include typical geophysical ground sensors already deployed on Earth, the Moon, and Mars; pressure sensors on balloons; and airglow imagers on orbiters to detect ground motion, the infrasound signals generated by seismic waves, and the corresponding airglow variations in the upper atmosphere.

Here, we provide a first comparison between the detection capabilities of these different measurement techniques and recent estimates of Venus' seismic activity.

In addition, we discuss the performance requirements and measurement durations required to detect seismic waves with the

various detection methods. As such, our study clearly presents the advantages and limitations of the different seismic wave detection techniques and can be used to drive the design of future mission concepts aiming to study the seismicity of Venus.

1           **Seismic wave detectability on Venus using ground**  
2           **deformation sensors, infrasound sensors on balloons**  
3           **and airglow imagers**

4           **Raphael F. Garcia<sup>1</sup>, Iris van Zelst<sup>2,3</sup>, Taichi Kawamura<sup>4</sup>, Sven Peter**  
5           **Näsholm<sup>5,6</sup>, Anna Horleston<sup>7</sup>, Sara Klaasen<sup>8</sup>, Maxence Lefèvre<sup>9</sup>, Celine Marie**  
6           **Solberg<sup>5</sup>, Krystyna T. Smolinski<sup>8</sup>, Ana-Catalina Plesa<sup>2</sup>, Quentin Brissaud<sup>6</sup>,**  
7           **Julia S. Maia<sup>2</sup>, Simon C. Stähler<sup>8</sup>, Philippe Lognonné<sup>4</sup>, Mark Panning<sup>10</sup>,**  
8           **Anna Gülcher<sup>10,11</sup>, Richard Ghail<sup>12</sup>, Barbara De Toffoli<sup>13,14</sup>**

9           <sup>1</sup>Institut Supérieur de l'Aéronautique et de l'Espace ISAE-SUPAERO, Université de Toulouse

10           <sup>2</sup>Institute of Planetary Research, German Aerospace Center (DLR), Berlin, Germany

11           <sup>3</sup>Centre of Astronomy and Astrophysics, Technical University of Berlin, Berlin, Germany

12           <sup>4</sup>Université Paris Cité, Institut de physique du globe de Paris, CNRS, Paris, France

13           <sup>5</sup>Department of Informatics, University of Oslo, Oslo, Norway

14           <sup>6</sup>NORSAR, Kjeller, Norway

15           <sup>7</sup>School of Earth Sciences, University of Bristol, Bristol, UK

16           <sup>8</sup>ETH Zürich, Switzerland

17           <sup>9</sup>LATMOS/IPSL, Sorbonne Université, UVSQ Université Paris-Saclay, CNRS, Paris, France

18           <sup>10</sup>Jet Propulsion Laboratory, California Institute of Technology, Pasadena, USA

19           <sup>11</sup>Seismological Laboratory, California Institute of Technology, Pasadena, USA

20           <sup>12</sup>Royal Holloway, University of London, London, UK

21           <sup>13</sup>INAF, Istituto di Astrofisica e Planetologia Spaziali, Rome, Italy

22           <sup>14</sup>Department of Geosciences, University of Padova, Padova, Italy

23           **Key Points:**

- 24           • The capabilities of various measurement concepts to detect quakes on Venus are  
25           estimated and compared to recent Venus seismicity estimates
- 26           • Ground sensors are limited by their short measurement duration, but also by a  
27           minimum noise level that may be below atmosphere induced noise
- 28           • Atmospheric seismology concepts are limited to large quake magnitudes, and air-  
29           glow imagers are favored relative to balloon measurements

---

Corresponding author: Raphaël F. Garcia, [raphael.garcia@isae-supero.fr](mailto:raphael.garcia@isae-supero.fr)

**Abstract**

The relatively unconstrained internal structure of Venus is a missing piece in our understanding of the Solar System formation and evolution. To determine the seismic structure of Venus' interior, the detection of seismic waves generated by venusquakes is crucial, as recently shown by the new seismic and geodetic constraints on Mars' interior obtained by the InSight mission. In the next decades multiple missions will fly to Venus to explore its tectonic and volcanic activity, but they will not be able to conclusively report on seismicity or detect actual seismic waves. Looking towards the next fleet of Venus missions in the future, various concepts to measure seismic waves have already been explored in the past decades. These detection methods include typical geophysical ground sensors already deployed on Earth, the Moon, and Mars; pressure sensors on balloons; and airglow imagers on orbiters to detect ground motion, the infrasound signals generated by seismic waves, and the corresponding airglow variations in the upper atmosphere. Here, we provide a first comparison between the detection capabilities of these different measurement techniques and recent estimates of Venus' seismic activity. In addition, we discuss the performance requirements and measurement durations required to detect seismic waves with the various detection methods. As such, our study clearly presents the advantages and limitations of the different seismic wave detection techniques and can be used to drive the design of future mission concepts aiming to study the seismicity of Venus.

**Plain Language Summary**

We do not really know what the interior of Venus looks like. Even the first-order structure of the size of Venus' core is plagued with large uncertainties. For other planets, such as the Earth and Mars, the interior structure is much better constrained. This is largely thanks to the seismological investigations performed on these planets that revealed their interior structure by studying the seismic waves caused by quakes. In the next decades, new missions will fly to Venus to explore its tectonic and volcanic activity, but they will not be able to detect any seismic waves. In order to help design future mission concepts, we discuss instruments that could record seismic waves, as already used on the Earth, the Moon, and Mars; instruments on balloons that could float in the Venusian atmosphere; and instruments on spacecrafts that monitor the variations of atmospheric emissions caused by seismic waves originating at the surface. We compare all these different techniques with each other and with recent estimates of Venus' seismic activity to see which of them works best in different scenarios.

**1 Introduction**

The internal structures of the planets are key information to better understand the formation and the evolution of our Solar System. Although Venus is similar to Earth in terms of size and mass, our knowledge of its internal structure is limited due to its slow rotation, which hinders the determination of its moment of inertia (Margot et al., 2021) and creates large error bars on Love number estimates (Dumoulin et al., 2017). The detection and characterization of seismic waves is the best tool to infer the internal structure of planets (Lognonné et al., 2023). However, the deployment of long-duration geophysical instrumentation, which demonstrated its capabilities during the InSight mission on Mars (Stähler et al., 2021; Durán, Khan, Ceylan, Zenhäusern, et al., 2022; Durán, Khan, Ceylan, Charalambous, et al., 2022; Drilleau et al., 2022; Samuel et al., 2023; Lognonné et al., 2023) is not possible on Venus due to its harsh surface conditions. At the same time, there is a growing number of studies that have presented evidence that Venus is volcanically and tectonically active at present (Smrekar et al., 2010; Gülcher et al., 2020; Byrne et al., 2021; Van Zelst, 2022; Smrekar et al., 2023; Herrick & Hensley, 2023) indicating that the planet is probably also seismically active. Indeed, recent estimates of

80 Venus' seismicity indicate that Venus could host hundreds of quakes per year with  $M_w \geq$   
 81 5 when Venus is assumed to be moderately active and potentially be as seismically ac-  
 82 tive as the Earth in its most extreme end-member scenario (Van Zelst et al., 2024).

83 Despite the compelling arguments in favor of monitoring seismic wave propagation  
 84 in Venus, none of the three missions scheduled by ESA and NASA to visit Venus in the  
 85 next decade (i.e., the EnVision (Widemann et al., 2022), VERITAS (Smrekar et al., 2022),  
 86 and DAVINCI+ (Garvin et al., 2022) missions) are targeting the detection of seismic waves.  
 87 This is primarily due to the challenges associated with conducting such measurements  
 88 for Venus. Over the past decade, various measurement concepts have been explored, falling  
 89 into three main categories: (i) ground deformation instruments deployed on the planet's  
 90 surface, (ii) infrasound sensors mounted on balloon platforms, and (iii) airglow imagers  
 91 on board orbiters (Stevenson et al., 2015). The concepts for ground surface deployment  
 92 of seismic sensors are limited by the high atmospheric surface temperature ( $\approx 740$  K) in  
 93 the absence of high temperature electronics. This limits the measurement duration to  
 94 a total amount of approximately one day (Kremic et al., 2020). Seismic infrasound de-  
 95 tection methods concern themselves with the low attenuation of upward-propagating in-  
 96 frasound waves created by seismic waves below 1 Hz (Garcia et al., 2005). These infra-  
 97 sounds conserve the dispersion features of seismic surface waves during their upward prop-  
 98 agation (Lognonné et al., 2016). These two properties allow us to assume that the in-  
 99 frasound created by seismic surface waves retains all the properties of seismic surface waves  
 100 that are necessary to determine the seismic velocity profile in the first hundreds of kilo-  
 101 meters depth of the planet, as it was done by InSight on Mars (Kim et al., 2022; Car-  
 102 rasco et al., 2023; Xu et al., 2023). Two different concepts based on the detection of seis-  
 103 mic infrasound have been investigated thoroughly in the past decade. First, pressure sen-  
 104 sors on board of balloon platforms have been studied (Stevenson et al., 2015; Krishnamoor-  
 105 thy & Bowman, 2023). Their capabilities to detect and characterise seismic waves have  
 106 been demonstrated theoretically and have even been observed on Earth recently for the  
 107 first time (Brissaud et al., 2021; Garcia et al., 2022). Secondly, airglow emission varia-  
 108 tions induced by seismically generated tsunami waves have been observed on Earth (Makela  
 109 et al., 2011; Occhipinti et al., 2011) and the sensitivity of airglow emissions to gravity  
 110 waves has been observed in Venus atmosphere (Garcia et al., 2009). Indeed, mission con-  
 111 cepts targeted to the observation of seismically-induced variations of  $1.27 \mu\text{m}$  nightglow  
 112 and  $4.3 \mu\text{m}$  dayglow in Venus' atmosphere have been developed (Stevenson et al., 2015;  
 113 Sutin et al., 2018).

114 The purpose of this study is to perform a first comparison between the capabili-  
 115 ties of all these diverse measurement techniques and the most recent estimates of Venus  
 116 seismicity. For each observation technique, we also discuss the minimum performance  
 117 and measurement duration. We focus on globally observable seismic waves for events of  
 118 moment magnitude larger than 3 ( $M_W > 3$ ).

## 119 **2 Estimating seismic wave detection capabilities of different observa-** 120 **tion concepts**

### 121 **2.1 Seismic signal estimates**

122 In the absence of internal structure models of Venus that are directly constrained  
 123 by data, the currently-used internal structure models of Venus are constrained by plan-  
 124 etary formation and geodynamic models, solar abundance estimates, and physical assump-  
 125 tions, and rely on the adaptation of Earth models to Venus conditions (Zharkov, 1983;  
 126 Gudkova & Zharkov, 2020). As a consequence, these models present a large uncertainty  
 127 in terms of both seismic velocities and seismic attenuation parameters. This is why we  
 128 choose to base our estimates of seismic wave amplitudes and frequency content on Earth's  
 129 scaling relations, rather than performing complex computations in highly uncertain mod-  
 130 els of the Venusian interior. Because seismic surface waves show the highest amplitude

131 for shallow quakes on Earth, we will assume that these waves are also dominating the  
 132 seismic signal on Venus in the quake magnitude range considered in this study, i.e., mo-  
 133 ment magnitudes larger than 3.0. In addition, since the dispersion of seismic surface waves  
 134 is strongly dependent on the seismic structure of the crust and the top of the mantle,  
 135 the observation of these waves is critical to constrain the structure of the first hundreds  
 136 of kilometers of Venus' interior. The definition of surface-wave magnitude,  $M_S$ , shows  
 137 a direct link with the amplitude of the seismic surface Rayleigh waves around the 20 s  
 138 period:

$$M_S = \log_{10} \left( \frac{A_d}{T_S} \right) + 1.66 \log_{10}(\Delta) + 3.3, \quad (1)$$

139 where  $M_S$  is the surface wave magnitude,  $A_d$  the vertical ground displacement in  $\mu m$ ,  
 140  $T_S$  is the period considered for measuring  $A_d$ , and  $\Delta$  is the epicentral distance of the quake  
 141 in degrees (Bormann & Dewey, 2012). We will use this relation to determine the am-  
 142 plitude of the surface Rayleigh waves as a function of distance for a given surface wave  
 143 magnitude.

## 144 2.2 Atmosphere effects and parameters

145 The detectability of infrasound by balloon platforms and airglow imagers is sen-  
 146 sitive to the amplitude of the source and atmospheric path effects (Garcia et al., 2005).  
 147 In particular, attenuation processes on Venus can strongly dampen and disperse the in-  
 148 frasound energy. To assess the impact of attenuation on acoustic waves, we determine  
 149 the energy loss vs. altitude for a vertically propagating planar wave. In the frequency  
 150 range of interest (0.01–1 Hz), the attenuation of infrasound in the Venusian atmosphere  
 151 is dominated by CO<sub>2</sub> relaxation effects (Bass & Chambers, 2001; Petculescu, 2016), al-  
 152 though some contributions are also expected from sulfuric acid (H<sub>2</sub>SO<sub>4</sub>) droplet-related  
 153 processes, primarily in the cloudy 45 to 70 km altitude regime (Trahan & Petculescu,  
 154 2020).

155 We compute atmospheric parameters using the Venus Climate Database (VCD)  
 156 (Gilli et al., 2017, 2021; Martinez et al., 2023) to estimate the attenuation due to CO<sub>2</sub>  
 157 relaxation,  $\alpha_{CO_2}(z)$ . We extract a single vertical profile of specific heats, and sound speed  
 158 is extracted at the equator at midday local time. From this VCD profile, we then use  
 159 the approach described in Garcia et al. (2017) to extract the CO<sub>2</sub> relaxation frequency  
 160 and relaxation strength, as well as the sound speed as a function of altitude. In low-attenuation  
 161 scenarios, it is appropriate to sum the attenuation contributions from CO<sub>2</sub> and H<sub>2</sub>SO<sub>4</sub>  
 162 (Nachman et al., 1990), to obtain the total attenuation  $\alpha_{tot}(z) = \alpha_{CO_2}(z) + \alpha_{H_2SO_4}(z)$ .  
 163 In Figure 1, we use these estimates to explore the amplitude loss using a plane-wave as-  
 164 sumption, focusing on acoustic waves at periods from 1 to 50 s from the ground up to  
 165 140 km altitude. A significant increase in attenuation occurs in the cloud layers, where  
 166 strong diffusion-mediated phase changes occur due to sulfuric acid droplets (Petculescu,  
 167 2016). Yet, our estimates suggest that attenuation has an insignificant impact on acous-  
 168 tic waves of periods larger than 1 second up to the bottom of the airglow layer IR1. At  
 169 the altitude of airglow layer IR2, longer-period waves of interest for airglow (10 s to 50 s  
 170 period) are not damped much. However, at this altitude, a significant energy loss of  $\sim 50\%$   
 171 is predicted, which dramatically reduces the likelihood of detection for 1 s period waves.  
 172 Note that this analysis assumes linear acoustics and takes neither nonlinear propagation  
 173 nor wave-breaking effects into account.

## 174 2.3 Estimating the minimum number of events per magnitude per year

175 In this section, we provide detection thresholds that can be directly compared to  
 176 seismicity estimates (Van Zelst et al., 2024). To do so, we estimate the requirements to  
 177 detect at least one event larger than a given magnitude during the full mission duration.

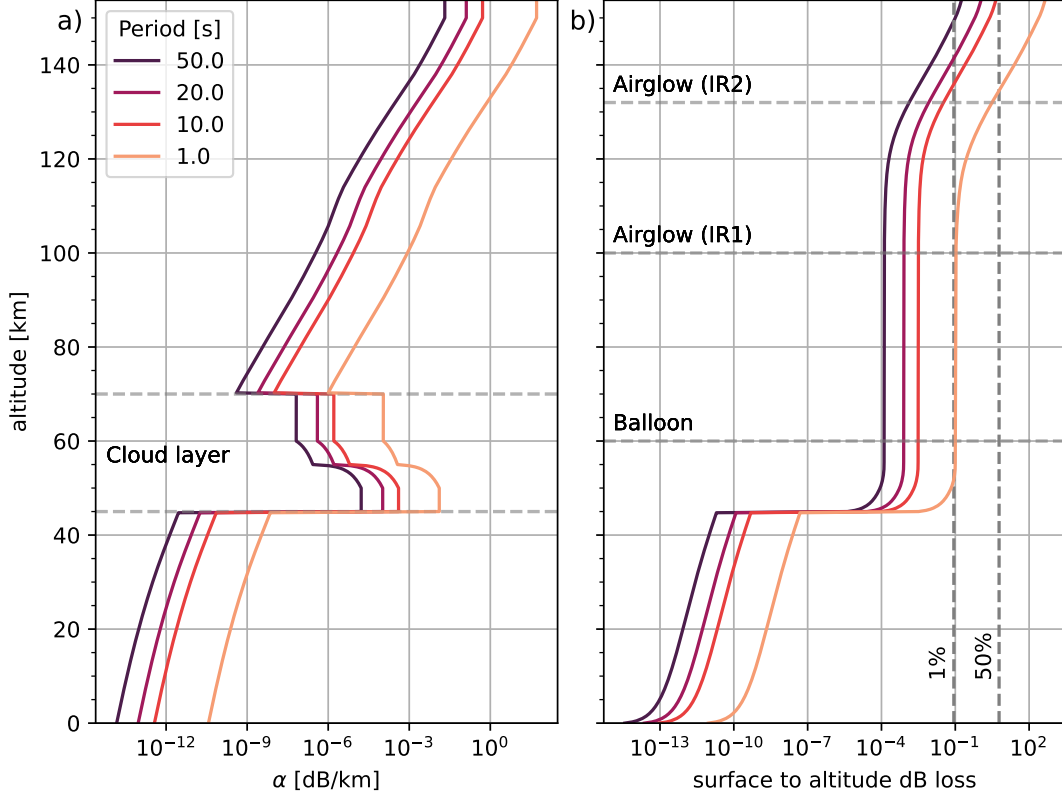


**Figure 1.** (a) plane-wave infrasound attenuation ( $\alpha$  in dB/km) based on a Venus Climate Database (VCD) atmospheric profile, including both the  $\alpha_{\text{H}_2\text{SO}_4}$  and the  $\alpha_{\text{CO}_2}$  contributions, and the sulfuric acid cloud contributions given in Trahan and Petculescu (2020). We consider wave periods from 1 to 50 s. (b) The total loss (in dB) due to the attenuation in (a), integrated from the ground up to the given altitude. The two vertical dashed lines indicate accumulated amplitude losses of 1% and 50%.

178 Assuming the seismic events to be Poisson distributed and setting our desired probabil-  
 179 ity of detection at 63% yields the following relation for a signal-to-noise ratio threshold  
 180 of one:

$$N_m^{\min}(M_S) = \frac{1}{T_m} \frac{S_P}{S_m(M_S)}, \quad (2)$$

181 where  $T_m$  is time in Earth years,  $S_P$  is the surface area of Venus, and  $*_m$  signifies method  
 182  $m$ :  $s$  for seismometer,  $r$  for ground rotation sensor,  $d$  for ground Distributed Acoustic  
 183 Sensing (DAS),  $b$  for pressure sensors on board balloons and  $a$  for airglow imagers. Us-  
 184 ing this relation, the surface area  $S_m(M_S)$  over which a quake of a given surface-wave  
 185 magnitude  $M_S$  can be detected by a given method is investigated in the following sec-  
 186 tions.

187 This relation is only valid statistically with a 63% confidence interval if we assume  
 188 that the seismic events have a Poisson distribution. Moreover, it is assumed that the seis-  
 189 mic event probability is homogeneous over the Venus surface, which is unrealistic, but  
 190 a starting point at a time when no actual mission concept is evaluated. Our estimates  
 191 thus provide a lower bound of the detection limits of each measurement concept.

192 In order to estimate  $\frac{S_P}{S_m(M_S)}$ , we need to estimate a maximum distance  $\Delta_m(M_S)$ ,  
 193 usually in degrees, at which the event can be detected for the different methods, within  
 194 a signal-to-noise ratio larger than a given value  $\text{SNR}_{\min}$ . Knowing this number, the sur-  
 195 face area ratio is

$$\frac{S_P}{S_m(M_S)} = \frac{4\pi}{2\pi(1 - \cos(\Delta_m(M_S)))}, \quad (3)$$

196 with  $\Delta_m(M_S)$  the maximum epicentral distance at which you can expect to detect the  
 197 quake.

198 Usually, the noise levels of the instruments are provided in Power of Amplitude Spectral  
 199 Density (ASD) in physical unit over square root of hertz ( $\text{ASD}_n$ ). In contrast, the  
 200 signal amplitude terms in Equation 1 are provided at a given period ( $T_S$ ), and consequently  
 201 the signal amplitude on the instrument is also in physical units at a given period ( $A_m$ ).  
 202 In order to compare these two numbers, we convert the amplitude spectral density val-  
 203 ues into root-mean-square values, under the conservative hypothesis that we filter the  
 204 signals over a bandwidth of 1/3 octave ( $\pm 11.5\%$ ) around the central frequency  $f_S = \frac{1}{T_S}$ .  
 205 As a consequence, the root-mean-square noise amplitude is defined by the product of the  
 206 amplitude spectral density times the square root of the frequency bandwidth, assuming  
 207 that the noise power is constant over the bandwidth (Bormann, 2002):

$$N_{\text{rms}} = \text{ASD}_n \sqrt{\frac{0.23}{T_S}}. \quad (4)$$

208 As a consequence, the maximum epicentral distance at which you can expect to detect  
 209 a quake of magnitude  $M_S$  ( $\Delta_m(M_S)$ ) is defined by equating the signal-to-noise ratio to  
 210 its minimum value  $\text{SNR}_{\min}$ , fixed here to 3:

$$\frac{A_m(\Delta_m(M_S))}{N_{\text{rms}}} = \text{SNR}_{\min}. \quad (5)$$

211 In conclusion, in order to estimate  $N_m^{\min}(M_S)$ , i.e., the minimum number of events per  
 212 year, as a function of surface wave magnitude, to measure at least 1 event of this type  
 213 by a given method, one needs to invert the above equations to get the maximum distance  
 214 at which an event can be detected by a given method  $\Delta_m(M_S)$ , and then compute  $N_m^{\min}(M_S)$   
 215 through Equations 3 and 2. However, because the relation of Equation 1 holds only for  
 216 teleseismic distances, and because we need the waves to be separated in time in order  
 217 to analyze them properly, we impose  $\Delta_m(M_S) > 3^\circ$ . This restriction sets the lower-bound  
 218 limit on the  $M_S$  values.

## 219 **2.4 Detection capabilities of various observation concepts**

### 220 **2.4.1 Quake detection by landed seismometer**

221 Due to the high surface temperatures on Venus and the limited amount of solar en-  
 222 ergy that reaches the surface, deploying instruments on the ground is challenging. With  
 223 conventional electronics, surface landers lasted less than two hours on the Venusian sur-  
 224 face in the past (Kerzhanovich & Marov, 1983; Moroz, 1983). However, to be able to de-  
 225 termine global seismicity levels, several Earth days of active monitoring would proba-  
 226 bly be required at minimum.

227 Recent advances in high-temperature electronics (Wilson et al., 2016; Kremic et  
 228 al., 2020; Glass et al., 2020) have made long-lived landers a possibility for the coming  
 229 decades, using silicon carbide (SiC) seismometers. These SiC integrated circuits have been  
 230 demonstrated to provide 60 functioning days in high-fidelity simulated Venusian surface  
 231 conditions (Hunter et al., 2021; Chen et al., 2019; Neudeck et al., 2018). However, the

232 development of the associated electronics coping with the harsh Venus conditions is still  
233 required.

234 Memory is another issue with Venusian surface conditions. Depending on power  
235 availability, data storage and transmission could be difficult. Tian et al. (2023) designed  
236 a low-memory algorithm to circumvent this issue that triggers transmission during earth-  
237 quakes and avoids transmission during wind and other noise events (Tian et al., 2023).

238 Only a handful of probes recorded data at the surface of Venus. Only VENERA-  
239 9 and 10 directly measured the wind for 49 min and 90 s, respectively (Avduevskii et  
240 al., 1977), and VENERA-13 and 14 indirectly measured the wind speed (Ksanfomaliti  
241 et al., 1983). The amplitudes of the measured wind speeds are less than  $2 \text{ m s}^{-1}$  below  
242 100 m height (Lorenz, 2016), with a higher probability for values below  $0.5 \text{ m s}^{-1}$ .

243 Simulations with a global circulation model showed the diurnal cycle of the Plan-  
244 etary Boundary Layer (PBL) activity is correlated with the diurnal cycle of surface winds  
245 (Lebonnois et al., 2018), with downward katabatic winds at night and upward anabatic  
246 winds during the day along the slopes of high-elevation terrains. With a high-resolution  
247 model, Lefèvre et al. (2024) confirmed this diurnal cycle of the surface wind. The resolved  
248 large-scale horizontal wind at 10 m above the local surface is above  $1 \text{ m s}^{-1}$  in the moun-  
249 tains in the equatorial region and below  $0.5 \text{ m s}^{-1}$  in the low plains.

250 Lefèvre (2022) used a turbulent-resolving model to quantify the turbulent activ-  
251 ity at the surface of Venus. At noon, the height of the PBL varies from 1.5 km in the  
252 plains to 7 km in the high terrains by the equator. This difference is due to the impact  
253 of the anabatic winds. This difference in PBL height at noon, results in a difference in  
254 turbulent horizontal winds amplitude, reaching  $2 \text{ m s}^{-1}$  for the high terrain compared  
255 to between 1 and  $1.5 \text{ m s}^{-1}$  in the plains. At night, when the impact of the slope winds  
256 is weaker, the height of the PBL is almost the same around 500 m, resulting in horizon-  
257 tal winds amplitude below  $0.5 \text{ m s}^{-1}$ . Placing a seismometer in the low plain, and record-  
258 ing signals by night, seems to be the optimal plan to limit the noise of the atmosphere.

259 Lorenz (2012) roughly quantified the wind noise at the surface of Venus. With an  
260 atmospheric density of  $65 \text{ kg/m}^3$ , a wind speed of  $0.25 \text{ m s}^{-1}$  is comparable in terms of  
261 dynamic pressure to wind speeds of  $20 \text{ m s}^{-1}$  on Mars, which were regularly observed  
262 during the daytime by InSight (Banfield et al., 2020) The corresponding seismic ampli-  
263 tude is 120.0 nm. Atmospheric noise could therefore limit seismic detection, and shield-  
264 ing the instrument might be necessary.

265 Venera-14 reportedly detected Venusian microseisms with a geophone in only an  
266 hour of operation (Ksanfomaliti et al., 1982). The amplitude of the signals are consis-  
267 tent with ‘noisy’ environments on Earth (Lorenz & Panning, 2018), i.e. from  $\sim 10^{-8}$  to  
268  $10^{-6} \text{ m/s}^2/\sqrt{\text{Hz}}$  which roughly spans the space between the low and high noise mod-  
269 els for Earth (Peterson, 1993). Therefore, surface-wind noise on Venus must be properly  
270 quantified. In addition, it is important to note that for high-quality seismic measurements,  
271 the wind speed and pressure should be monitored continuously.

272 The Brownian noise of a Short Period (SP) sensor comparable to the InSight sen-  
273 sor (Lognonné et al., 2019) in a vacuum is modeled to have an acceleration noise den-  
274 sity of  $\sqrt{\frac{k_B T \alpha}{m}}$  where  $k_B$  is Boltzmann’s constant,  $T$  the absolute temperate,  $\alpha$  the damp-  
275 ing constant, and  $m$  the proof mass (Mimoun et al., 2017). For a standard SP, the proof  
276 mass is 0.8 g. Recalculating from Mimoun et al. (2017) with  $T = 740 \text{ K}$ , gives a noise  
277 of  $4.37 \cdot 10^{-10} \text{ m/s}^2/\sqrt{\text{Hz}}$ . If not in a vacuum, the suspension noise also includes a vis-  
278 cous damping term which could contribute. At 740 K, this additional term reaches  $3.3 \cdot$   
279  $10^{-9} \text{ m/s}^2/\sqrt{\text{Hz}}$ , giving a total suspension noise of  $3.77 \cdot 10^{-9} \text{ m/s}^2/\sqrt{\text{Hz}}$ , lower than  
280 the atmospheric noise. Other sensor noise sources should also be considered and prop-  
281 erly calculated for the Venusian environment, such as digitizer/acquisition noise, ther-

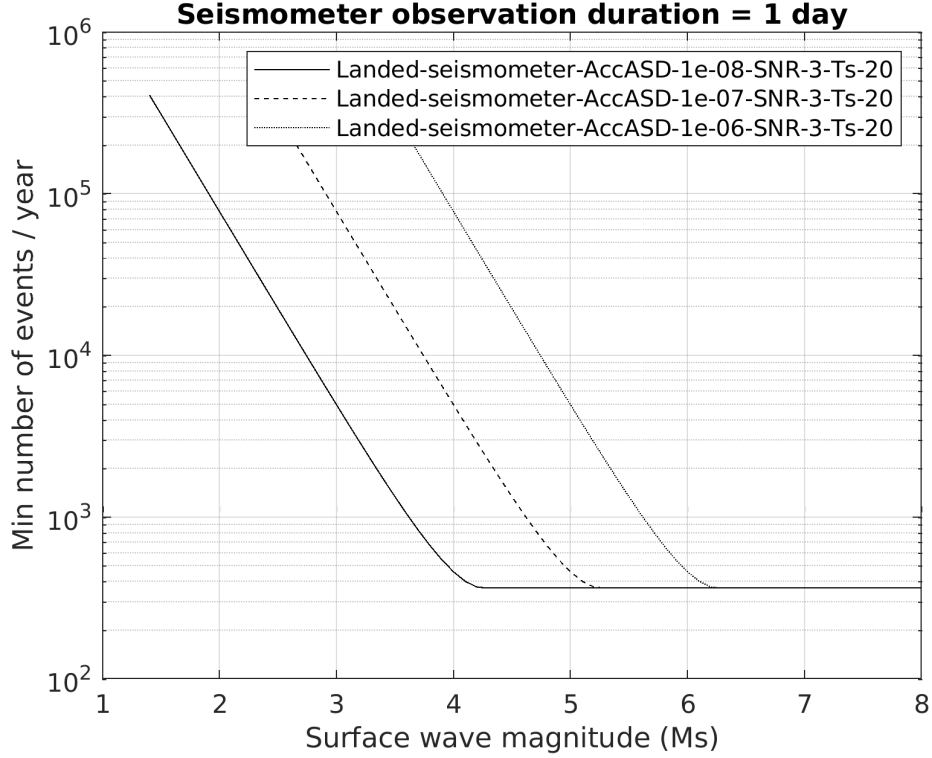


**Figure 2.** Minimum number of events per year as a function of surface wave magnitude required on the surface of Venus to measure at least one event of this magnitude during a seismometer observation duration of 1 day. Results are provided for different noise levels:  $10^{-8}$  (plain line) and  $10^{-7}$  (dashed line),  $10^{-6}$  (dotted line)  $\text{m/s}^{-2}/\sqrt{\text{Hz}}$  at 20 s period.

mal noise, noise from wind on the sensor, and atmospheric noise/noise of the lander itself.

With an  $SNR_{min}$  set to 3 and a period  $T_s$  of 20 s,  $\Delta_m(M_S)$  can be estimated for a given magnitude from Equations 1 and 5 as:

$$\log_{10}(\Delta_m(M_S)) = \frac{M_s - 3.3 - \log_{10}\left(\frac{SNR_{min} N_{rms}}{T_s}\right)}{1.66}. \quad (6)$$

Following Equations 2 and 3, the minimum number of events for each magnitude on the surface of Venus to result in at least one detection during the mission lifetime is shown in Figure 2. For the lowest noise level estimated to be  $10^{-8} \text{ m/s}^2/\sqrt{\text{Hz}}$ , global detection is possible for surface wave magnitudes above  $M_s = 4.3$ . For a higher noise level, this limit increases to  $M_s = 5.3$  for  $10^{-7} \text{ m/s}^2/\sqrt{\text{Hz}}$  and to  $M_s = 6.3$  for  $10^{-6} \text{ m/s}^2/\sqrt{\text{Hz}}$ . Under our idealized conditions, events above this threshold need to occur just once during the mission to be detectable, which creates the lower limit of 365 events per year in fig. 2.

#### 2.4.2 Quake detection with DAS on the surface

Distributed Acoustic Sensing (DAS) is an emerging technology in the field of Earth geophysics, and has been applied in increasingly remote and harsh locations on Earth,

297 such as glaciers (Walter et al., 2020; Hudson et al., 2021), volcanoes (Klaasen et al., 2021;  
 298 Jousset et al., 2022; Klaasen et al., 2023) and submarine environments (Cheng et al., 2021;  
 299 Lior et al., 2021). It employs a fiber-optic cable that is interrogated with laser pulses,  
 300 resulting in seismic deformation measurements at a high spatial and temporal resolu-  
 301 tion along the cable. We refer the reader to Zhan (2020), and Lindsey and Martin (2021)  
 302 for more in-depth descriptions of DAS and its applications on Earth. We optimistically  
 303 propose to extend the use of DAS beyond Earth, and to visualize the hypothetical de-  
 304 tection capabilities of DAS on Venus.

305 We follow the procedures as outlined in Section 2.3 to obtain the detection capa-  
 306 bilities for DAS on Venus, as shown in Figure 3. We estimate the minimum number of  
 307 required events per year based on parameters and assumptions similar to the ones used  
 308 for the landed seismometer in Section 2.4.1. On top of the noise estimates of  $10^{-8}$ ,  $10^{-7}$   
 309 and  $10^{-6}$   $\text{m/s}^2/\sqrt{\text{Hz}}$ , we also use the noise-floor in strain as reported by the iDAS Ca-  
 310 rina from Silixa, as an example of the self-noise of an interrogator currently on the mar-  
 311 ket. The noise estimates in  $\text{m/s}^2/\sqrt{\text{Hz}}$  are transformed from ground acceleration to strain  
 312 using the plane-wave assumption (Daley et al., 2016; Wang et al., 2018; Näsholm et al.,  
 313 2022), assuming an apparent velocity of seismic surface waves of 2250 m/s, which cor-  
 314 responds to an approximate Rayleigh wave velocity in mid-oceanic ridge basaltic mate-  
 315 rial at 20 second period (as suggested for Venus; Surkov et al., 1984) with a Poisson ra-  
 316 tio of 0.25:

$$\epsilon = aT_S/V_R, \quad (7)$$

317 where  $\epsilon$  is the strain,  $a$  is the acceleration in  $\text{m/s}^2$  which is linked to a given quake mag-  
 318 nitude by Equation 1,  $T_S$  is the period of the wave in s, and  $V_R$  is the Rayleigh wave ve-  
 319 locity in m/s. The entire calculation is then based on the values in strain; the native unit  
 320 of a DAS interrogator.

321 While the calculation based on different noise estimates paints an optimistic pic-  
 322 ture, we emphasize that a DAS deployment on Venus is at the moment not feasible due  
 323 to several obstacles, such as (i) the current instrumental capacities, (ii) deployment op-  
 324 tions, (iii) cable coupling conditions, and (iv) unknown cable locations. The instruments  
 325 currently on the market are not able to operate under the pressure and temperature at  
 326 the surface of Venus. However, some experiments have demonstrated the ability of spe-  
 327 cialized gold-coated optical fibers to survive and function with low attenuation at tem-  
 328 peratures up to 773 K for up to 900 hours (Jacobsen et al., 2018), with optical fiber man-  
 329 ufacturers also quoting operating temperatures up to 973 K (e.g. (Heracle, 2023)). The  
 330 development of high-temperature and corrosion-resistant fibers is an area of active re-  
 331 search, for example within the oil and gas industry (Reinsch & Hennings, 2010; Stolov  
 332 & OFS, 2019)). Alternative fiber optic sensing systems are also already in development  
 333 for structural health monitoring on future spacecraft (Chan et al., 2015; Parker et al.,  
 334 2024).

335 Assuming the further development of DAS instruments and their ability to oper-  
 336 ate on Venus, we are limited by the deployment of the cable. If the cable is released dur-  
 337 ing the landing, we are unable to control the exact layout and coupling conditions of the  
 338 cable, which will likely decrease the data quality and the consequent conclusions that  
 339 can be drawn from the data. If the cable is not buried and protected, other noise sources  
 340 are likely to overpower any seismic signals - a phenomenon observed on Earth with at-  
 341 mospheric noise, in submarine environments with strong currents (Lior et al., 2021), or  
 342 on Mars with the atmospheric wind and pressure noise (Mimoun et al., 2017). Addition-  
 343 ally, DAS yields single-component data, therefore a cable layout with varying angles and  
 344 directions is necessary to capture the complete wavefield and locate events. However, this  
 345 also requires exact geographical knowledge of the cable layout, which may be difficult

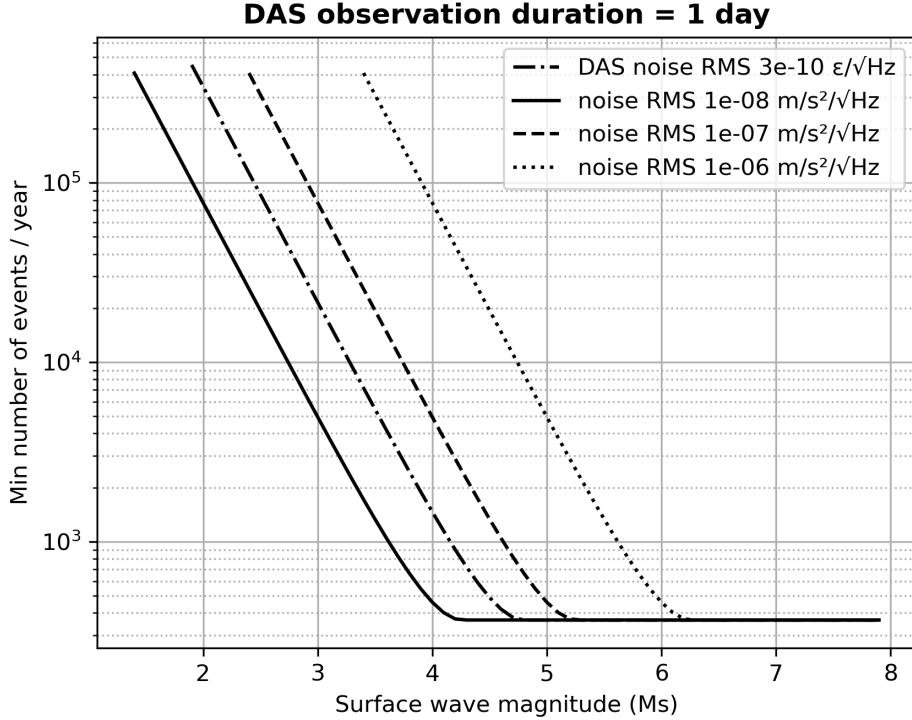


**Figure 3.** Minimum number of events per year as a function of surface wave magnitude required to measure at least one event of this magnitude during a DAS observation duration of 1 day. Results are provided for different noise levels:  $10^{-8}$  (plain line) and  $10^{-7}$  (dashed line),  $10^{-6}$  (dotted line)  $\text{m/s}^{-2}/\sqrt{\text{Hz}}$  at 20 s period. An estimate assuming that the noise floor is controlled by a typical self noise of a DAS interrogator (iDAS Carina of Silixa company) is provided as dotted-dashed lines.

346 to obtain on Venus due to the lack of a GPS network and difficulty capturing georeferenced images of the cable.  
347

348 Hence, in order to facilitate a DAS experiment on Venus, research primarily needs  
349 to focus on instrumental development and the feasibility of experimental deployment.  
350 The instrument needs to be able to operate its laser and conduct preliminary data analysis  
351 before sending the data back to orbit to avoid, in order to avoid a bottle neck caused  
352 by the large amounts of data produced by DAS experiments. Additionally, the cable needs  
353 to be deployed in such a fashion to guarantee atmospheric protection and good coupling  
354 with the ground, and would ideally have a well-known, and non-linear layout.

### 355 *2.4.3 Quake detection with ground rotation sensors*

356 The sensing of the ground rotations induced by seismic waves is an emerging field.  
357 The ground rotations allow for inferring the gradients of the seismic wavefield. These  
358 measurements allow seismologists to distinguish between various seismic waves (Sollberger  
359 et al., 2023), to correct for tilt effects on seismometers (Bernauer, Wassermann, & Igel,  
360 2020) and to infer anisotropy parameters (Noe et al., 2022). There are also many other  
361 applications for inverse problems and seismic source determination (Schmelzbach et al.,  
362 2018). This domain is currently limited by the self-noise level of the instruments (Bernauer

363 et al., 2021) and planetary applications are promising but mainly limited by the avail-  
 364 able instrumentation (Bernauer, Garcia, et al., 2020).

365 The currently available instruments are measuring the ground rotation speed in rad/s  
 366 ( $\omega$ ) along three perpendicular axis. With the same assumption as those used in the pre-  
 367 vious section to estimate the ground strain, this parameter can be linked to the ground  
 368 acceleration by the following equation

$$\omega = aT_S/(2\pi\lambda), \quad (8)$$

369 where  $\omega$  is the ground rotation in rad/s,  $a$  the acceleration in  $\text{m/s}^2$ ,  $T_S$  the period of the  
 370 surface wave in s, and  $\lambda$  the wavelength in meters which is computed assuming a sur-  
 371 face wave velocity of 2250 m/s.

372 We follow the procedures as outlined in Section 2.3 to obtain the detection capa-  
 373 bilities for ground rotation sensors on Venus as shown in Figure 4. We estimate the min-  
 374 imum number of required events per year based on parameters and assumptions simi-  
 375 lar to the ones used for the landed seismometer in Section 2.4.1. On top of the noise es-  
 376 timates of  $10^{-8}$ ,  $10^{-7}$  and  $10^{-6}$   $\text{m/s}^2/\sqrt{\text{Hz}}$ , we also use the noise-floor in rad/s as re-  
 377 ported for the BlueSeis3A sensor from the iXblue company ( $20 \text{ nrad/s}/\sqrt{\text{Hz}}$ ), as an ex-  
 378 ample of the self-noise of a rotation sensor on the market.

379 As observed in Figure 4, the event detection is limited by the self-noise of current  
 380 ground rotation instruments (Bernauer, Garcia, et al., 2020). As a consequence, even if  
 381 the ground rotation measurements present less deployment constraints than the DAS sys-  
 382 tems, the interest of such measurements is limited to large-amplitude signals, and thus  
 383 to large-amplitude quakes close to the instrument.

#### 384 **2.4.4 Quake detection by pressure sensors onboard balloons**

385 Stratospheric balloon flights on Earth present noise levels around  $0.05 \text{ Pa}/\sqrt{\text{Hz}}$  at  
 386 20 s period and  $0.01 \text{ Pa}/\sqrt{\text{Hz}}$  at 10 s period (Garcia et al., 2022). The amplitude of pres-  
 387 sure perturbations generated by a vertical displacement  $A_d$  (in  $\mu\text{m}$ ) at period  $T_S$  can be  
 388 computed using the following formula, assuming that the acoustic wave attenuation is  
 389 negligible (Garcia et al., 2005):

$$DP = \rho(z_b)c(z_b)\sqrt{\frac{\rho(0)c(0)}{\rho(z_b)c(z_b)}}\left(\frac{10^{-6}2\pi A_d}{T_S}\right) \quad (9)$$

390 in which  $\rho(z)$  and  $c(z)$  are the density and the sound speed at altitude  $z$  in the atmo-  
 391 sphere respectively. The product of the first two terms is the impedance conversion from  
 392 particle velocity to pressure at balloon altitude ( $z_b = 60 \text{ km}$ ). The third term is the  
 393 amplification factor for particle velocity from the ground to the balloon altitude. The  
 394 last term is the ground velocity of seismic waves in m/s at  $T_S$  period.

395 Using Equations 2, 3, 6, 5, 4 and 9 one can obtain the minimum number of events  
 396 per year required to measure at least 1 event of a given magnitude during the observa-  
 397 tion duration. The results are presented in Figure 5. This suggests a minimum amount  
 398 of events  $M_S = 6$  between 20 and 100 is required to detect at least one quake. Note  
 399 that at large magnitudes, the minimum number of events is limited to 4 per year, be-  
 400 cause the mission duration is 1/4 of a year.

#### 401 **2.4.5 Quake detection by Airglow measurements onboard orbiters**

402 Various studies pointed to the sensitivity of Venus' airglow emissions to pressure,  
 403 temperature and density variations induced by acoustic waves (Garcia et al., 2009; Steven-  
 404 son et al., 2015; López-Valverde et al., 2011). These studies mainly target two infrared

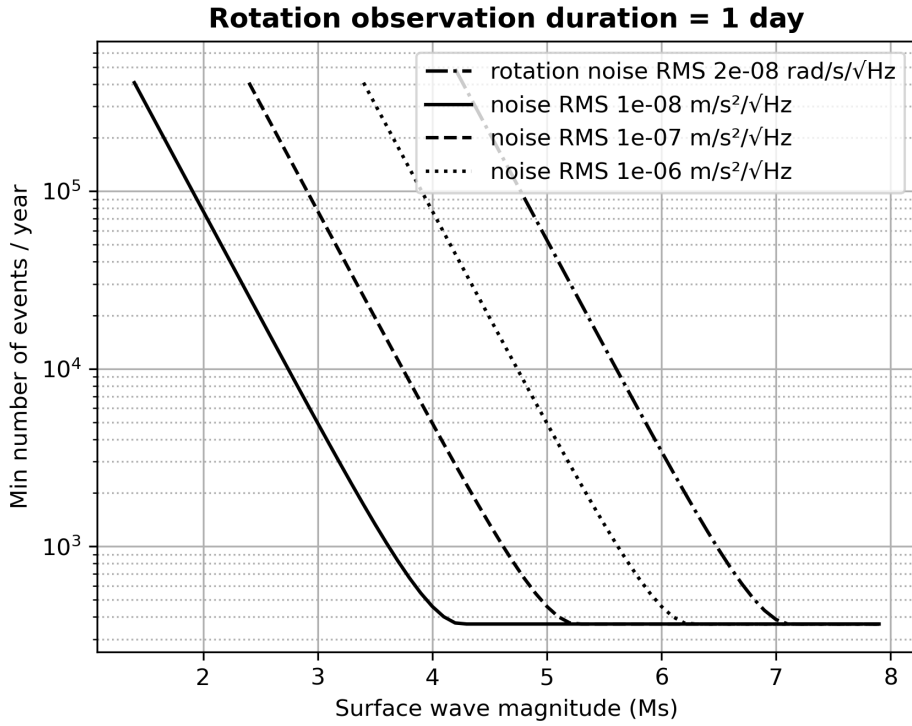


**Figure 4.** Minimum number of events per year as a function of surface wave magnitude required to measure at least one event of this magnitude during a ground rotation observation duration of 1 day. Results are provided for different noise levels:  $10^{-8}$  (plain line) and  $10^{-7}$  (dashed line),  $10^{-6}$  (dotted line)  $\text{m/s}^{-2}/\sqrt{\text{Hz}}$  at 20 s period. An estimate assuming that the noise floor is controlled by a typical self noise of a ground rotation instrument (BlueSeis-3A of iXblue company) is provided as dotted-dashed lines.

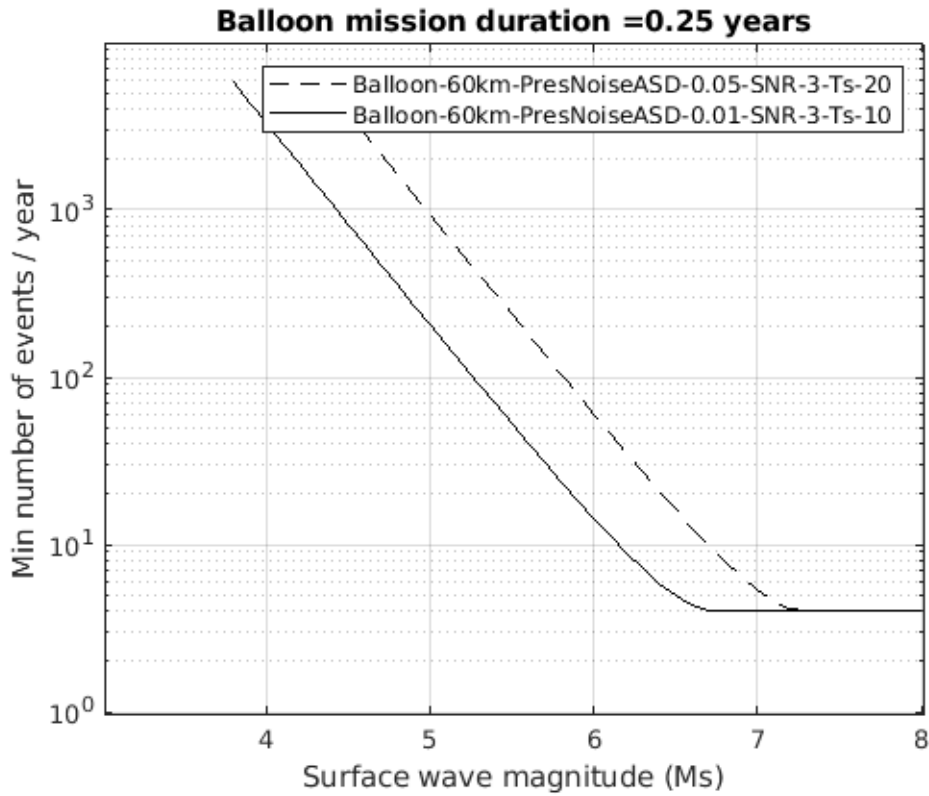


**Figure 5.** Minimum number of events per year as a function of surface wave magnitude required to measure at least one event of this magnitude during a balloon mission duration of 3 months. Results are provided at two different periods: 20 s (dashed line) and 10 s (plain line) because the noise level of pressure measurements varies significantly with frequency (from 0.05 to 0.01 Pa/ $\sqrt{\text{Hz}}$  going from 20 s to 10 s period).

405 airglows: nighttime airglow at 1.27  $\mu\text{m}$  and day time Non-Local Thermodynamical Equi-  
 406 librium emissions around 4.3  $\mu\text{m}$  (in fact two emission peaks at 4.28  $\mu\text{m}$  and 4.32  $\mu\text{m}$ ).  
 407 These studies paved the way to a dedicated mission concept studied at JPL/NASA (Sutin  
 408 et al., 2018). We will use this mission design, called VAMOS, in order to infer the de-  
 409 tection capabilities of airglow measurements in terms of the minimum number of events  
 410 per year required to detect at least one quake with this detection method. The concept  
 411 is targeting a continuous monitoring of the planet disk with a high sampling rate ( $> 1$   
 412 sample per second) camera orbiting on a circular equatorial orbit at a radius of 45,000  
 413 km with a period of approximately 29.2 hours.

414 As the measurement concept is different from a single point measurement by landed  
 415 seismometers or balloons, Equation 2 must be revised. First, because the airglow emis-  
 416 sions are localized only on a specific part of the planet, we must define this area as the  
 417 Observation Area ( $OA$ ) for a given airglow. For 1.27  $\mu\text{m}$  emission, this observation area  
 418 is centered on the equatorial point at 1:00 AM local time and covers an angular radius  
 419 of about  $60^\circ$  around that point, because it is in this region that we expect the largest  
 420 background emissions (Gérard et al., 2008). For simplicity, we assume that the center  
 421 point of this area is located at midnight local time. For 4.3  $\mu\text{m}$  emission, the observa-  
 422 tion area is centered on the equatorial point at 12:00 local time (midday) and covers an  
 423 angular radius of about  $70^\circ$  around that point. These emissions are proportional to solar  
 424 illumination, but polar regions and regions close to the terminator are conservatively  
 425 excluded because background emissions are low, and because more variability is expected  
 426 from gravity wave activity (Seiff & Kirk, 1991; Garcia et al., 2009; Gérard et al., 2014).

427 Then, another difference compared to single point measurements is that the ob-  
 428 servation area is not always visible in the camera images. To illustrate this, we use the  
 429 equatorial circular orbit of VAMOS to simplify the computations, although it still pro-  
 430 vides similar visibility statistics to other orbits at different ellipticity and inclination when  
 431 ensuring that the full disk is visible on more than 80% of the orbit period. In the full-  
 432 disk images of the planet, we conservatively consider that only points having an angu-  
 433 lar distance smaller than  $70^\circ$  for the center of the image (located at the equator) can be  
 434 used for observation because points close to the limb will have too much image distor-  
 435 tion. As a consequence, for a given local time position ( $\phi$  in longitude degrees) of the  
 436 center of the image (at the equator) relative to the center position of the visibility area  
 437 ( $\phi_0$ ) the visible observation area ( $VOA$ ) will be defined by the intersection of two spher-  
 438 ical caps (or solid angles) of size  $60^\circ$  (or  $70^\circ$ ) for the observation area and size  $70^\circ$  for  
 439 the imaging capability. Due to the rotation of the spacecraft around the planet, the size  
 440 of the visible observation area will vary as a function of the parameter  $\phi$ .

441 The function  $VOA(\Delta\phi)$ , with  $\Delta\phi = \phi - \phi_0$  is symmetric around zero. When this  
 442 area is zero (i.e., the observation area is not visible from the spacecraft) the correspond-  
 443 ing time period must be subtracted from the mission duration to define the observation  
 444 duration ( $T_m$  of Equation 2). When this area is non-zero, all the points in the area have  
 445 the capability of detecting seismic waves. Consequently, the surface  $S_m(M_S)$  of Equa-  
 446 tion 2 is much larger than for a single-point observation because it includes the whole  
 447 visible observation area  $VOA(\Delta\phi)$ , and extends it in both latitude and longitude direc-  
 448 tions by  $\Delta_m(M_S)$  degrees. When the surface of the visible observation area is non-zero,  
 449 the surface of the detection area is computed by the joint area of two spherical caps for  
 450 each surface wave magnitude ( $M_S$ ) and each longitude separation ( $\Delta\phi$ ) between the two  
 451 spherical caps (i.e., the visibility area and the image usable area). The average area over  
 452 all possible  $\Delta\phi$  values is then scaled to  $4\pi$  as in Equation 2. The observation duration  
 453 is reduced by the amount of time during which the visible observation area is zero.

454 Once these geometrical considerations have been taken into account, we still have  
 455 to compute the maximum distance at which a quake can be observed by a point in the  
 456 observation area  $\Delta_m(M_S)$ .

457 For the 1.27  $\mu\text{m}$  nighttime emissions, we need to convert the vertical particle ve-  
 458 locity in the acoustic wave into airglow emission and compare to the instrument noise.  
 459 The vertical particle velocity at the altitude of the maximum emission rate of the 1.27  $\mu\text{m}$   
 460 airglow ( $z_{IR1} = 100 \text{ km}$ ) is provided by:

$$A_v(z_{IR1}) = \sqrt{\frac{\rho(0)c(0)}{\rho(z_{IR1})c(z_{IR1})}} \left( \frac{10^{-6} A_d(0)}{2\pi T_S} \right) \quad (10)$$

461 where  $A_d(0)$  as function of surface wave magnitude is provided by inverting Equation 1.  
 462 The sensitivity of 1.27  $\mu\text{m}$  emissions is driven by the transport of the emitting molecules  
 463 under the vertical velocity  $A_v(z_{IR1})$  (Lognonné et al., 2016). The order of magnitude  
 464 of this sensitivity is about 3.0%/(m/s) at 20 s period and 6%/(m/s) at 50 s period at  
 465 100 km altitude (Sutin et al., 2018) In addition, the estimated noise level of an imag-  
 466 ing InfraRed (IR) camera targeting these emissions is about 0.5% of background emis-  
 467 sion level (Sutin et al., 2018).

468 For the 4.3  $\mu\text{m}$  daytime emission, we focus on the 4.28  $\mu\text{m}$  emission peak and as-  
 469 sume that the emission altitude is approximately 135 km and that these emissions present  
 470 a sensitivity of 1% per Kelvin variation of atmospheric temperature (López-Valverde et  
 471 al., 2011). In order to convert the vertical particle velocity  $A_v(z_{IR2})$  into temperature  
 472 perturbation (in Kelvin), we use the impedance at  $z_{IR2} = 135 \text{ km}$  altitude:

$$DP(z_{IR2}) = \rho(z_{IR2})c(z_{IR2})A_v(z_{IR2}) \quad (11)$$

$$= \rho(z_{IR2})c(z_{IR2}) \sqrt{\frac{\rho(0)c(0)}{\rho(z_{IR2})c(z_{IR2})}} \left( \frac{10^{-6} 2\pi A_d(0)}{T_S} \right) \quad (12)$$

473 which is similar to Equation 9 but at the altitude of the 4.28  $\mu\text{m}$  emission peak. Then,  
 474 we assume both the perfect gas law and the adiabatic nature of the acoustic wave per-  
 475 turbations in order to quantify the corresponding temperature changes through the fol-  
 476 lowing equation:

$$DT(z_{IR2}) = \frac{\gamma - 1}{\gamma} \frac{T(z_{IR2})}{P(z_{IR2})} DP(z_{IR2}), \quad (13)$$

477 where  $\gamma$  is the heat capacity ratio at altitude  $z_{IR2} = 135 \text{ km}$ , and  $T(z_{IR2})$  and  $P(z_{IR2})$   
 478 are the background temperature and pressure at this altitude, respectively. Finally, us-  
 479 ing the sensitivity of 1% per Kelvin of the 4.28  $\mu\text{m}$  emission, we obtain the expected sig-  
 480 nal in percentage of background emission (López-Valverde et al., 2011). Concerning the  
 481 instrument noise, we assume that the root-mean-square noise of the detector is about  
 482 0.125% of background emission (Sutin et al., 2018).

483 Gathering all these equations, we obtain the minimum number of events per year  
 484 for a mission duration of 2 years, and for the two infrared emissions. This result is shown  
 485 in Figure 6. The minimum surface magnitude that can be detected through these air-  
 486 glow emissions is between 4.5 and 5. However, we have a low variability of the minimum  
 487 number of events per year because of the large extent of the observation area.

#### 488 **2.4.6 Comparing the different seismic wave measurements concepts**

489 Figure 7 assembles the detection capabilities of all the different seismic wave mea-  
 490 surement concepts in the same figure, although the ground sensors in this figure are lim-  
 491 ited to seismometers, as the other ground measurement concepts are not yet technologi-  
 492 cally feasible. From this figure, it is clear that the airglow emissions are best designed  
 493 to detect quakes of surface wave magnitude larger than 5. In addition, the capability of

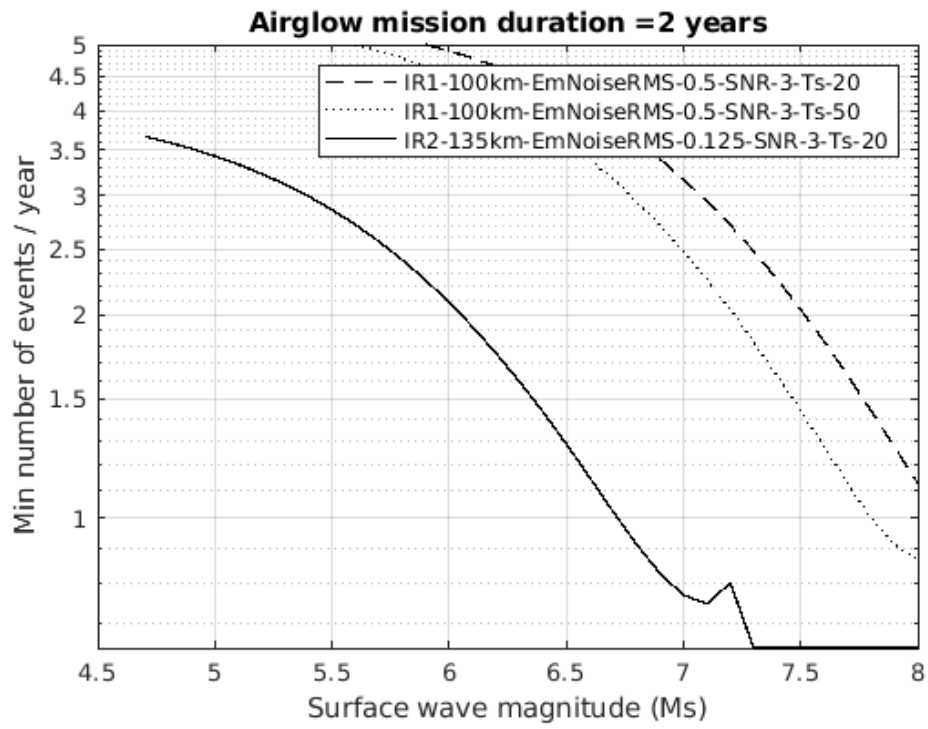


**Figure 6.** Minimum number of events per year as a function of surface wave magnitude required to measure at least one event of this magnitude during an airglow orbiter mission duration of 2 years. Results are provided for the two airglow emissions respectively at  $1.27 \mu\text{m}$  (dashed line at 20 s period, dotted line at 50 s period) and at  $4.28 \mu\text{m}$  (solid line).

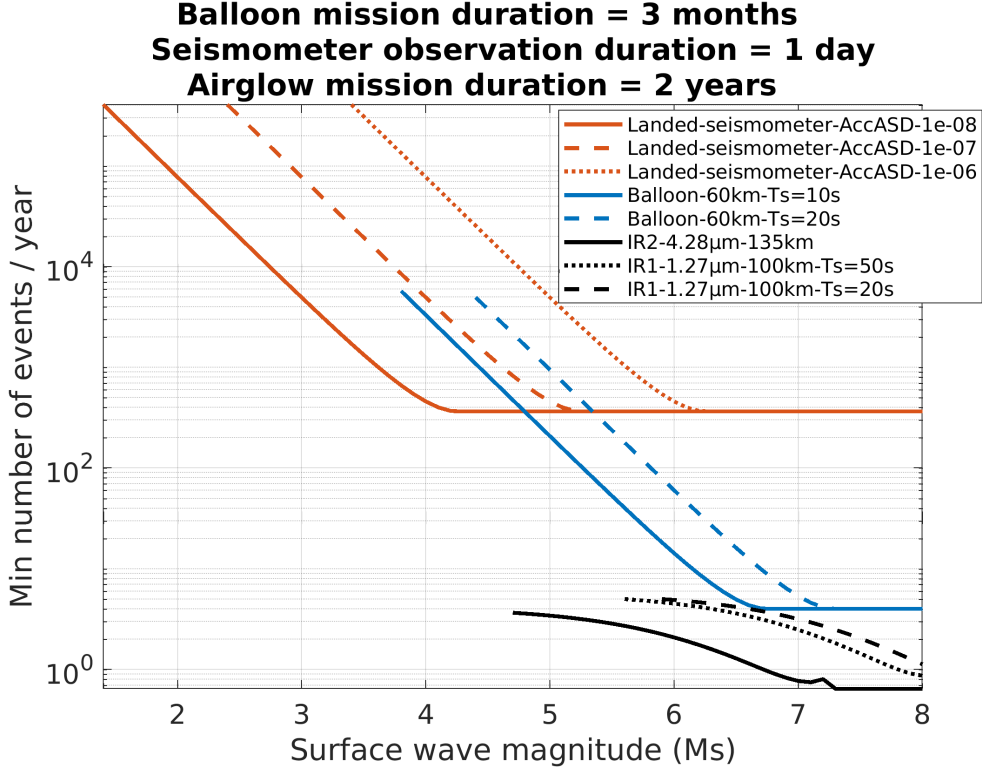


**Figure 7.** Minimum number of events per year as a function of surface wave magnitude required to measure at least one event of this magnitude for all the detection methods. Balloon estimates in blue, landed seismometers in brown, and airglow emissions in black.

494 such observations to track surface wave propagation on the images is opening more op-  
 495 portunities to image lateral variations in the crust and the lithosphere. However, due to  
 496 low-pass effects, induced by the vertical extent of airglow emission peaks and by the re-  
 497 sponse of airglow emissions to acoustic forcing, these observations are probably limited  
 498 to periods larger than 10 s (Lognonné et al., 2016; Sutin et al., 2018).

499 The balloon observations have a detection limit around 4.0–4.5 units of surface wave  
 500 magnitude and can detect all quakes with surface wave magnitude larger than 7. In ad-  
 501 dition, they can detect higher frequency signals, with a usable bandwidth mainly for pe-  
 502 riods between 0.5 s and 20 s. However, this observation mean suffers for its single point  
 503 measurement and from the short mission duration, estimated here to be 3 months.

504 Finally, for short duration deployment of a landed seismometer, the estimates present  
 505 a large variability due to the large uncertainties on the final noise level of such an instru-  
 506 ment. Assuming a noise level between  $10^{-7}$  and  $10^{-6}$   $\text{m/s}^2/\sqrt{\text{Hz}}$  at 20 s period, such  
 507 an instrument can detect all quakes of surface wave magnitude larger than 5 to 6. In ad-  
 508 dition, for small quakes close to the sensor, the bandwidth of such an instrument would  
 509 easily cover the 0.05–20 Hz. However, such a concept is strongly limited by the short ob-  
 510 servation duration, assumed here to be 1 day, such that it would allow us to investigate  
 511 only seismic events that are occurring more than 400 times per Earth year.

### 3 Comparing of detection capabilities with current seismicity estimates

Our estimates of detection capabilities are shown in figure 7 as a function of surface wave magnitude  $M_S$  which was defined following the IASPEI standard and corresponds to the definition of  $M_{S,20}$  by (Bormann et al., 2013). However, seismicity estimates are usually provided as a function of seismic moment magnitude  $M_W$  which is a better representation of the quake physics. In order to convert from  $M_S$  to  $M_W$ , we use the following relation defined by Bormann et al. (2013) for quake moment magnitudes smaller than 6.8 that are of our main interest:

$$M_W = 0.667 M_S + 2.18 \quad (14)$$

The error bar in this conversion is on the order of 0.3 magnitude unit, but even such large errors could in fact be smaller than the error we may have due to the unknown internal structure of Venus. Eventually, the moment magnitude is converted to the seismic moment  $M_0$  (in Nm) by the standard conversion formula  $M_W = \frac{2}{3}(\log_{10}(M_0) - 9.1)$ .

Once  $M_S$  has been converted into  $M_W$  or  $M_0$ , we can directly compare our detection limits of at least one quake with a signal-to-noise ratio larger than 3 over the mission duration with the Venus seismicity estimates by (Van Zelst et al., 2024). This comparison is presented in Figure 8.

The detection limits presented here should be taken with caution for two main reasons. First, the limitations presented in the next section induce an error bar on the order of one order of magnitude on these estimates. Secondly, we investigated mainly seismic signals around the 20 s period whereas the expected bandwidths of the different methods are different with an upper bound frequency of 10 Hz for ground sensors to 0.1 Hz for airglow observations.

Despite these limitations, a few interesting observations can be made in Figure 8. The ground-based sensors can be considered adequate for seismic wave detection if their noise level at 20 s period is below  $10^{-8} \text{ m/s}^2/\sqrt{\text{Hz}}$  and if they are deployed in an active seismic area that would allow us to detect quakes of magnitudes smaller than 4.0. The pressure sensors on balloon platforms allow for probing quake magnitudes in the 5.0 to 7.0 moment magnitude range and mainly for seismic signal frequencies in the 0.05 to 1 Hz range. Lastly, the airglow measurements have the lowest detection limits due to the low noise level and the long duration of the observations. In addition, the output movie of wave propagation would allow for determining the source location and investigating variations in seismic surface speeds over the planet that could be related to lateral heterogeneities in the shallow seismic wave structure of the crust. However, this measurement concept is limited to seismic moment magnitudes larger than 5.5 and to wave periods larger than 5 s.

### 4 Limitations

Our analysis operated under certain assumptions that leave room for future improvements and exploration.

First, the spatial dependence of seismicity estimates is not taken into account in our estimates of quake detectability, despite the likelihood that certain areas on Venus exhibit higher seismic activity compared to others. Even if this issue is not so critical for airglow measurements that will cover a large part of the planet surface, it is obvious that ground sensor deployments should target the most active regions in order to improve their detection capabilities. The balloon missions are also expected to cover more equatorial regions than polar regions due to deployment and mission duration constraints.

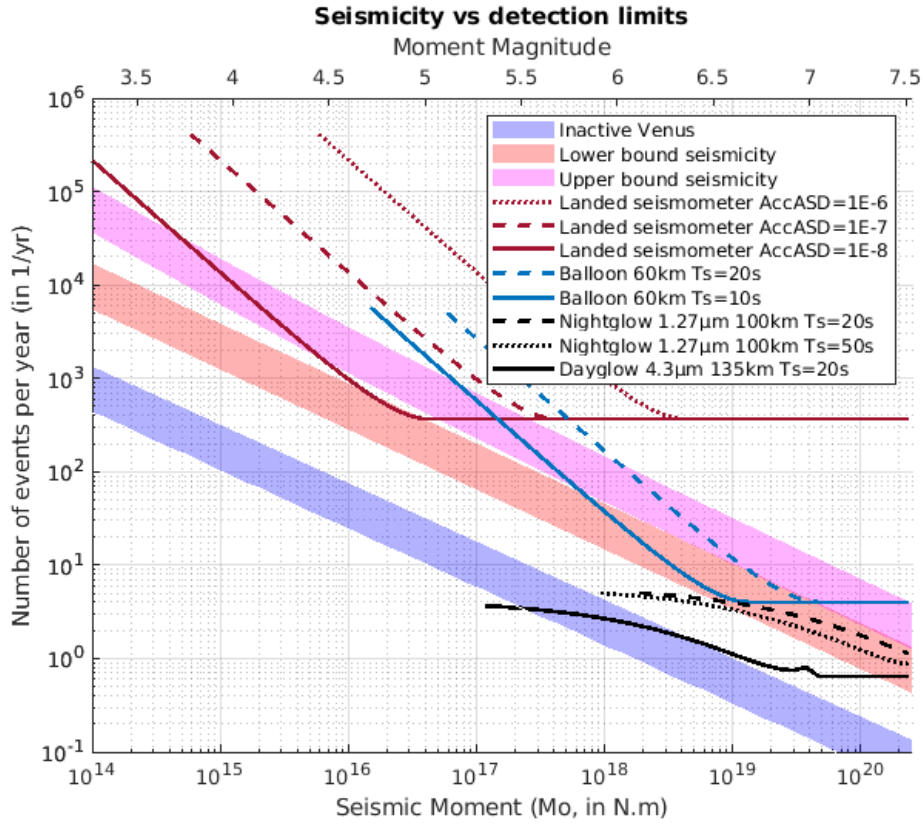


**Figure 8.** Minimum number of events per year as a function of seismic moment (in N·m) on the bottom and moment magnitude on top required to measure at least one event of this magnitude for all the detection methods (lines) compared to end-member Venus seismicity estimates (shaded areas) by Van Zelst et al. (2024): an inactive Venus (blue), lower bound active Venus (red) and upper bound active Venus (magenta). Balloon estimates are in dark blue, landed seismometers in brown, and airglow emissions in black.

557 A second important limitation is the uncertainty on the noise levels of each mea-  
 558 surement concept. Even though we consider reasonable assumptions on these numbers  
 559 and provided estimates for different noise levels, detailed noise models of these measure-  
 560 ment concepts are required to fully validate our analysis. Mimoun et al. (2017) provides  
 561 an example of a detailed noise model for a seismometer instrument. An inherent diffi-  
 562 culty to the noise model exercise is that the mission parameters (lander size, instrument  
 563 performance parameters, etc.) must be known in order for the analysis to be valid.

564 Lastly, the method used to relate ground movements to quake magnitude and the  
 565 frequencies considered here (periods between 10 and 50 seconds) are mainly relevant for  
 566 quake moment magnitudes between 4.0 and 6.8 (Bormann et al., 2013). For quake mo-  
 567 ment magnitudes smaller than 4.0, other methods and frequency ranges should be con-  
 568 sidered.

## 569 5 Conclusion

570 Our study provides a first estimate of the detection capabilities of long period seis-  
 571 mic surface waves on Venus by various measurement concepts: ground sensors includ-  
 572 ing seismometers, DAS, and rotation sensors; infrasound sensors on balloons; and air-  
 573 glow imagers onboard orbiters. We also compare these estimates with recent predictions  
 574 of Venus seismicity. The airglow measurement concept appears to be most relevant in  
 575 light of the current estimates of seismicity, but it is limited to moment magnitudes larger  
 576 than 5.5 and wave periods larger than 5 s. We find that a minimum measurement du-  
 577 ration of two years ensures a good probability to detect large magnitude quakes. Infra-  
 578 sound sensors onboard balloons must ensure an overall noise level below  $10^{-2}$  Pa/ $\sqrt{\text{Hz}}$   
 579 at 10 s period and a measurement duration in the order of a month to obtain a good prob-  
 580 ability of quake detection. The ground sensors are strongly limited by their measurement  
 581 duration but also by their noise, mainly due to instrument self-noise for potential ground  
 582 rotation sensors, and noise induced by the installation or environment for seismometers  
 583 and potential DAS fiber measurements that would be effective only with an overall ac-  
 584 celeration noise level at 20 s period below  $10^{-8}$  m/s<sup>2</sup>/ $\sqrt{\text{Hz}}$ . Uncertainties ranging up to  
 585 one order of magnitude impact these detection limit estimates due to limitations that  
 586 could be improved in various directions by future studies. Potential directions of improve-  
 587 ments would be to take into account the geographical distribution of quakes, a full mod-  
 588 eling of the amplitude of seismic and infrasound waves, detailed noise models of the mea-  
 589 surement concepts... Rather than definitively concluding on one measurement concept,  
 590 our study allows us to enhance the advantages and limitations of each measurement con-  
 591 cept and can drive requirements on future mission concepts that would deploy such mea-  
 592 surement tools.

593 Despite the recent selection of various space missions to Venus, none of these will  
 594 target the detection and characterization of seismic waves to investigate Venus' inter-  
 595 nal structure in better detail. The most realistic programmatic scenario for the imple-  
 596 mentation of any of the measurement concepts described in this study in the next decade  
 597 is therefore the deployment of such concepts by a small satellite as a piggyback payload  
 598 on one of these missions.

## 599 Open Research

600 All the codes and input data used to create the figures in this article are available  
 601 at the following zenodo repository <https://zenodo.org/records/10943310> (DOI: 10.5281/zen-  
 602 odo.10943310).

## Author contributions

Conceptualization: RFG, IvZ, KTS  
 Data curation:  
 Formal Analysis: RFG, SK, TK  
 Funding acquisition: IvZ  
 Investigation: RFG, SPN, QB  
 Methodology: RFG, SS  
 Project administration: IvZ  
 Resources: ML  
 Software: RFG, TK, SK, CMS  
 Supervision:  
 Validation: SPN, ML, CMS, QB  
 Visualization: RFG, SK, CMS, SPN  
 Writing – original draft: RFG, SK, SPN, QB, ML, AH, TK, KTS, CMS  
 Writing – review & editing: AG, SPN, IvZ, BDT, QB, ML, JM, ACP, AH, SS, PL, MP, KTS

## Acknowledgements

This research was supported by the International Space Science Institute (ISSI) in Bern, Switzerland through ISSI International Team project #566: “Seismicity on Venus: Prediction & Detection”, led by Iris van Zelst. RFG acknowledges funding by CNES through APR project “VenusGeox”. IvZ, JM, and ACP acknowledge the financial support and endorsement from the DLR Management Board Young Research Group Leader Program and the Executive Board Member for Space Research and Technology. IvZ also gratefully acknowledges the support by the Deutsche Forschungsgemeinschaft (DFG, German Research Foundation), Project-ID 263649064 – TRR 170. SPN, CMS, and QB acknowledge support from the Research Council of Norway basic research program FRIPRO through the project “Airborne Inversion of Rayleigh waves” under Contract 335903. ML acknowledges funding from the European Union’s Horizon Europe research and innovation program under the Marie Skłodowska-Curie grant agreement 101110489/MuSICA-V. AG acknowledges support by the Swiss National Science Foundation Postdoc Mobility Grant P500PN\_21729 and by the Jet Propulsion Laboratory, California Institute of Technology, under contract (80NM0018D0004) with the National Aeronautics and Space Administration. A.H. is funded by the UK Space Agency under grant numbers ST/W002523/1, ST/W002949/1 and ST/Y005597/1.

## References

- Avduevskii, V. S., Vishnevetskii, S. L., Golov, I. A., Karpeiskii, I. I., Lavrov, A. D., Likhushin, V. I., . . . Pronina, N. N. (1977). Measurement of wind velocity on the surface of Venus during the operation of stations Venera 9 and Venera 10. *Cosmic Research*, *14*(5), 710–713.
- Banfield, D., Spiga, A., Newman, C., Forget, F., Lemmon, M., Lorenz, R., . . . Banerdt, W. B. (2020, February). The atmosphere of Mars as observed by InSight. *Nature Geoscience*, *13*(3), 190-198. doi: 10.1038/s41561-020-0534-0
- Bass, H. E., & Chambers, J. P. (2001, May). Absorption of sound in the Martian atmosphere. *Acoustical Society of America Journal*, *109*(5), 2371–2371. doi: 10.1121/1.4744345
- Bernauer, F., Behnen, K., Wassermann, J., Egdorf, S., Igel, H., Donner, S., . . . Brokesova, J. (2021, January). Rotation, strain, and translation sensors performance tests with active seismic sources. *Sensors*, *21*(1), 264. doi: 10.3390/s21010264
- Bernauer, F., Garcia, R. F., Murdoch, N., Dehant, V., Sollberger, D., Schmelzbach,

- 653 C., ... de Raucourt, S. (2020, December). Exploring planets and asteroids  
654 with 6DoF sensors: Utopia and realism. *Earth, Planets and Space*, 72(1), 191.  
655 doi: 10.1186/s40623-020-01333-9
- 656 Bernauer, F., Wassermann, J., & Igel, H. (2020, September). Dynamic tilt correc-  
657 tion using direct rotational motion measurements. *Seismological Research Let-  
658 ters*, 91(5), 2872–2880. doi: 10.1785/0220200132
- 659 Bormann, P. (2002). *New manual of seismological observatory practice*. Geo-  
660 Forschungszentrum. doi: 10.2312/GFZ.NMSOP-2\_ch4
- 661 Bormann, P., & Dewey, J. W. (2012). The new IASPEI standards for determining  
662 magnitudes from digital data and their relation to classical magnitudes..
- 663 Bormann, P., Wendt, S., & DiGiacomo, D. (2013). Seismic sources and source pa-  
664 rameters. In *New manual of seismological observatory practice 2 (nmsop2)* (pp.  
665 1–259). Deutsches GeoForschungszentrum GFZ. doi: 10.2312/GFZ.NMSOP-2  
666 \_ch3
- 667 Brissaud, Q., Krishnamoorthy, S., Jackson, J. M., Bowman, D. C., Komjathy, A.,  
668 Cutts, J. A., ... Izraelevitz, G. J., J. S. and Walsh (2021). The first detec-  
669 tion of an earthquake from a balloon using its acoustic signature. *Geophysical  
670 Research Letters*, 48(12). doi: 10.1029/2021gl093013
- 671 Byrne, P. K., Ghail, R. C., Şengör, A. M. C., James, P. B., Klimczak, C., &  
672 Solomon, S. C. (2021). A globally fragmented and mobile lithosphere on  
673 venus. *Proceedings of the National Academy of Sciences*, 118(26). doi:  
674 10.1073/pnas.2025919118
- 675 Carrasco, S., Knapmeyer-Endrun, B., Margerin, L., Xu, Z., Joshi, R., Schimmel,  
676 M., ... Banerdt, W. B. (2023, August). Constraints for the Martian crustal  
677 structure from Rayleigh waves ellipticity of large seismic events. *Geophysical  
678 Research Letters*, 50(16), e2023GL104816. doi: 10.1029/2023GL104816
- 679 Chan, H. M., Parker, A. R., Piazza, A., & Richards, W. L. (2015). Fiber-optic  
680 sensing system: overview, development and deployment in flight at nasa. In  
681 *2015 IEEE Avionics and Vehicle Fiber-Optics and Photonics Conference (AVFOP)*  
682 (pp. 71–73).
- 683 Chen, L., Neudeck, P. G., Meredith, R. D., Lukco, D., Spry, D. J., Nakley, L. M., ...  
684 Hunter, G. W. (2019). Sixty earth-day test of a prototype Pt/HTCC alumina  
685 package in a simulated Venus environment. *Journal of microelectronics and  
686 electronic packaging*, 16(2), 78–83. doi: 10.4071/imaps.873073
- 687 Cheng, F., Chi, B., Lindsey, N. J., Dawe, T. C., & Ajo-Franklin, J. B. (2021). Uti-  
688 lizing distributed acoustic sensing and ocean bottom fiber optic cables for  
689 submarine structural characterization. *Scientific reports*, 11(1), 5613. doi:  
690 10.1038/s41598-021-84845-y
- 691 Daley, T., Miller, D., Dodds, K., Cook, P., & Freifeld, B. (2016). Field testing of  
692 modular borehole monitoring with simultaneous distributed acoustic sensing  
693 and geophone vertical seismic profiles at Citronelle, Alabama. *Geophysical  
694 Prospecting*, 64(5), 1318–1334. doi: 10.1111/1365-2478.12324
- 695 Drilleau, M., Samuel, H., Garcia, R. F., Rivoldini, A., Perrin, C., Michaut, C., ...  
696 Banerdt, W. B. (2022, September). Marsquake locations and 1-D seismic  
697 models for Mars from InSight data. *Journal of Geophysical Research (Planets)*,  
698 127(9), e07067. doi: 10.1029/2021JE007067
- 699 Dumoulin, C., Tobie, G., Verhoeven, O., Rosenblatt, P., & Rambaux, N. (2017,  
700 June). Tidal constraints on the interior of Venus. *Journal of Geophysical  
701 Research (Planets)*, 122(6), 1338–1352. doi: 10.1002/2016JE005249
- 702 Durán, C., Khan, A., Ceylan, S., Charalambous, C., Kim, D., Drilleau, M., ...  
703 Giardini, D. (2022, November). Observation of a Core-Diffracted P-Wave  
704 From a Farside Impact With Implications for the Lower-Mantle Struc-  
705 ture of Mars. *Geophysical Research Letters*, 49(21), e2022GL100887. doi:  
706 10.1029/2022GL100887
- 707 Durán, C., Khan, A., Ceylan, S., Zenhäusern, G., Stähler, S., Clinton, J. F., &

- 708 Giardini, D. (2022, April). Seismology on Mars: An analysis of direct,  
709 reflected, and converted seismic body waves with implications for interior  
710 structure. *Physics of the Earth and Planetary Interiors*, *325*, 106851. doi:  
711 10.1016/j.pepi.2022.106851
- 712 Garcia, R. F., Brissaud, Q., Rolland, L., Martin, R., Komatitsch, D., Spiga,  
713 A., ... Banerdt, B. (2017). Finite-difference modeling of acoustic and  
714 gravity wave propagation in Mars atmosphere: application to infrasounds  
715 emitted by meteor impacts. *Space Science Reviews*, *211*, 547–570. doi:  
716 10.1007/s11214-016-0324-6
- 717 Garcia, R. F., Drossart, P., Piccioni, G., López-Valverde, M., & Occhipinti, G.  
718 (2009, March). Gravity waves in the upper atmosphere of Venus revealed by  
719 CO<sub>2</sub> nonlocal thermodynamic equilibrium emissions. *Journal of Geophysical*  
720 *Research (Planets)*, *114*, E00B32. doi: 10.1029/2008JE003073
- 721 Garcia, R. F., Klotz, A., Hertzog, A., Martin, R., G erier, S., Kassarian, E., ... Mi-  
722 moun, D. (2022, August). Infrasound from large earthquakes recorded on a  
723 network of balloons in the stratosphere. *Geophysical Research Letters*, *49*(15).  
724 doi: 10.1029/2022gl098844
- 725 Garcia, R. F., Lognonn e, P. H., & Bonnin, X. (2005). Detecting atmospheric pertur-  
726 bations produced by Venus quakes. *Geophysical Research Letters*, *32*(16), 1–4.  
727 doi: 10.1029/2005GL023558
- 728 Garvin, J. B., Getty, S. A., Arney, G. N., Johnson, N. M., Kohler, E., Schwer,  
729 K. O., ... Zolotov, M. (2022). Revealing the mysteries of venus: The  
730 davinci mission. *The Planetary Science Journal*, *3*(5), 117. Retrieved from  
731 <http://dx.doi.org/10.3847/PSJ/ac63c2> doi: 10.3847/psj/ac63c2
- 732 G erard, J. C., Saglam, A., Piccioni, G., Drossart, P., Cox, C., Erard, S., ...  
733 S anchez-Lavega, A. (2008, January). Distribution of the O<sub>2</sub> infrared night-  
734 glow observed with VIRTIS on board Venus Express. *Geophysical Research*  
735 *Letters*, *35*(2), L02207. doi: 10.1029/2007GL032021
- 736 G erard, J. C., Soret, L., Piccioni, G., & Drossart, P. (2014). Latitudinal  
737 structure of the Venus O<sub>2</sub> infrared airglow: A signature of small-scale dy-  
738 namical processes in the upper atmosphere. *Icarus*, *236*, 92–103. doi:  
739 10.1016/j.icarus.2014.03.028
- 740 Gilli, G., Lebonnois, S., Gonz alez-Galindo, F., L opez-Valverde, M. A., Stolzenbach,  
741 A., Lef evre, F., ... Lott, F. (2017). Thermal structure of the upper atmo-  
742 sphere of Venus simulated by a ground-to-thermosphere GCM. *Icarus*, *281*,  
743 55–72. doi: 10.1016/j.icarus.2016.09.016
- 744 Gilli, G., Navarro, T., Lebonnois, S., Quirino, D., Silva, V., Stolzenbach, A., ...  
745 Schubert, G. (2021). Venus upper atmosphere revealed by a GCM: II. Model  
746 validation with temperature and density measurements. *Icarus*, *366*, 114432.  
747 doi: 10.1016/j.icarus.2021.114432
- 748 Glass, D. E., Jones, J.-P., Shevade, A. V., Bhakta, D., Raub, E., Sim, R., & Bugga,  
749 R. V. (2020). High temperature primary battery for Venus surface missions.  
750 *Journal of Power Sources*, *449*, 227492. doi: 10.1016/j.jpowsour.2019.227492
- 751 Gudkova, T. V., & Zharkov, V. N. (2020, March). Models of the internal structure  
752 of the Earth-like Venus. *Solar System Research*, *54*(1), 20–27. doi: 10.1134/  
753 S0038094620010049
- 754 G ulcher, A. J. P., Gerya, T. V., Mont esi, L. G. J., & Munch, J. (2020). Corona  
755 structures driven by plume–lithosphere interactions and evidence for on-  
756 going plume activity on Venus. *Nature Geoscience*, *13*(8), 547–554. doi:  
757 10.1038/s41561-020-0606-1
- 758 Heracle. (2023, 11). *Step Index Multimode Fibers Metal Coated Series: Gold*. Re-  
759 trieved from [https://www.heracle.de/products/step-index-multimode](https://www.heracle.de/products/step-index-multimode-fibers-metal-coated-series-gold/?lang=en)  
760 [-fibers-metal-coated-series-gold/?lang=en](https://www.heracle.de/products/step-index-multimode-fibers-metal-coated-series-gold/?lang=en)
- 761 Herrick, R., & Hensley, S. (2023). Surface changes observed on a Venusian volcano  
762 during the Magellan mission. *Science*, *379*(6638), 1205–1208. doi: 10.1126/

- 763 science.abm7735
- 764 Hudson, T. S., Baird, A. F., Kendall, J.-M., Kufner, S.-K., Brisbourne, A. M.,  
 765 Smith, A. M., . . . Clarke, A. (2021). Distributed acoustic sensing (DAS)  
 766 for natural microseismicity studies: A case study from Antarctica. *Journal of*  
 767 *Geophysical Research: Solid Earth*, *126*(7), e2020JB021493.
- 768 Hunter, G., Kremic, T., & Neudeck, P. G. (2021). High temperature electron-  
 769 ics for Venus surface applications: A summary of recent technical advances.  
 770 In *Bulletin of the american astronomical society* (Vol. 53, p. 399). doi:  
 771 10.3847/25c2cfcb.e3883e19
- 772 Jacobsen, W., Soufiane, A., & D’Urso, J. (2018). 500° c-rated optical fibers for high  
 773 temperature applications. In *80th eage conference and exhibition 2018* (Vol.  
 774 2018, pp. 1–5).
- 775 Jousset, P., Currenti, G., Schwarz, B., Chalari, A., Tilmann, F., Reinsch, T.,  
 776 . . . Krawczyk, C. M. (2022). Fibre optic distributed acoustic sensing  
 777 of volcanic events. *Nature communications*, *13*(1), 1753. doi: 10.1038/  
 778 s41467-022-29184-w
- 779 Kerzhanovich, V. V., & Marov, M. I. (1983). The atmospheric dynamics of Venus  
 780 according to Doppler measurements by the Venera entry probes. In *Venus* (pp.  
 781 766–778). The University of Arizona Press.
- 782 Kim, D., Banerdt, W. B., Ceylan, S., Giardini, D., Lekić, V., Lognonné, P., . . . Pan-  
 783 ning, M. P. (2022, October). Surface waves and crustal structure on Mars.  
 784 *Science*, *378*(6618), 417–421. doi: 10.1126/science.abq7157
- 785 Klaasen, S., Paitz, P., Lindner, N., Dettmer, J., & Fichtner, A. (2021). Dis-  
 786 tributed acoustic sensing in volcano-glacial environments—Mount Meager,  
 787 British Columbia. *Journal of Geophysical Research: Solid Earth*, *126*(11),  
 788 e2021JB022358. doi: 10.1029/2021JB022358
- 789 Klaasen, S., Thrastarson, S., Çubuk-Sabuncu, Y., Jónsdóttir, K., Gebraad, L.,  
 790 Paitz, P., & Fichtner, A. (2023). Subglacial volcano monitoring with  
 791 fibre-optic sensing: Grímsvötn, Iceland. *Volcanica*, *6*(2), 301–311. doi:  
 792 10.30909/vol.06.02.301311
- 793 Kremic, T., Ghail, R., Gilmore, M., Hunter, G., Kiefer, W., Limaye, S., . . . Wilson,  
 794 C. (2020). Long-duration Venus lander for seismic and atmospheric science.  
 795 *Planetary Space Science*, *190*, 104961. doi: 10.1016/j.pss.2020.104961
- 796 Krishnamoorthy, S., & Bowman, D. C. (2023, January). A “Floatilla” of Airborne  
 797 Seismometers for Venus. *Geophysical Research Letters*, *50*(2), e2022GL100978.  
 798 doi: 10.1029/2022GL100978
- 799 Ksanfomaliti, L. V., Goroshkova, N. V., & Khondyrev, V. K. (1983). Wind velocity  
 800 on the Venus surface from acoustic measurements. *Kosmicheskie Issledovaniia*,  
 801 *21*, 218–224.
- 802 Ksanfomaliti, L. V., Zubkova, V. M., Morozov, N. A., & Petrova, N. A. (1982). Mi-  
 803 croseisms at the Venera 13 and Venera 14 landing sites. *Pisma v Astronomich-*  
 804 *eskii Zhurnal*, *8*, 444–447.
- 805 Lebonnois, S., Schubert, G., Forget, F., & Spiga, A. (2018, November). Planetary  
 806 boundary layer and slope winds on Venus. *Icarus*, *314*, 149–158. doi: 10.1016/  
 807 j.icarus.2018.06.006
- 808 Lefèvre, M. (2022). Venus boundary layer dynamics: Eolian transport and convective  
 809 vortex. *Icarus*, *387*, 115167. doi: 10.1016/j.icarus.2022.115167
- 810 Lefèvre, M., Spiga, A., Lebonnois, S., & Forget, F. (2024). Control of the surface  
 811 temperature on Venus by slope winds. *To be Submitted*.
- 812 Lindsey, N. J., & Martin, E. R. (2021). Fiber-optic seismology. *Annual Review*  
 813 *of Earth and Planetary Sciences*, *49*, 309–336. doi: 10.1146/annurev-earth  
 814 -072420-065213
- 815 Lior, I., Sladen, A., Rivet, D., Ampuero, J.-P., Hello, Y., Becerril, C., . . . others  
 816 (2021). On the detection capabilities of underwater distributed acoustic sens-  
 817 ing. *Journal of Geophysical Research: Solid Earth*, *126*(3), e2020JB020925.

- 818 Lognonné, P., Banerdt, W. B., Clinton, J., Garcia, R. F., Giardini, D., Knapmeyer-  
819 Endrun, B., . . . Pike, W. T. (2023, May). Mars seismology. *Annual*  
820 *Review of Earth and Planetary Sciences*, *51*, 643–670. doi: 10.1146/  
821 annurev-earth-031621-073318
- 822 Lognonné, P., Banerdt, W. B., Giardini, D., Pike, W. T., Christensen, U., Laudet,  
823 P., . . . Wookey, J. (2019, January). SEIS: Insight’s seismic experiment  
824 for internal structure of Mars. *Space Science Reviews*, *215*(1), 12. doi:  
825 10.1007/s11214-018-0574-6
- 826 Lognonné, P., Karakostas, F., Rolland, L., & Nishikawa, Y. (2016, August). Mod-  
827 eling of atmospheric-coupled Rayleigh waves on planets with atmosphere:  
828 From Earth observation to Mars and Venus perspectives. *The Journal of the*  
829 *Acoustical Society of America*, *140*(2), 1447–1468. doi: 10.1121/1.4960788
- 830 López-Valverde, M. A., López-Puertas, M., Funke, B., Gilli, G., Garcia-Comas, M.,  
831 Drossart, P., . . . Formisano, V. (2011, August). Modeling the atmospheric  
832 limb emission of CO<sub>2</sub> at 4.3 μm in the terrestrial planets. *Planetary and Space*  
833 *Science*, *59*(10), 988–998. doi: 10.1016/j.pss.2010.02.001
- 834 Lorenz, R. D. (2012). Planetary seismology—expectations for lander and wind noise  
835 with application to Venus. *Planetary and Space Science*, *62*(1), 86–96. doi: 10  
836 .1016/j.pss.2011.12.010
- 837 Lorenz, R. D. (2016). Surface winds on Venus: Probability distribution from in-situ  
838 measurements. *Icarus*, *264*, 311–315. doi: 10.1016/j.icarus.2015.09.036
- 839 Lorenz, R. D., & Panning, M. P. (2018). Empirical recurrence rates for ground mo-  
840 tion signals on planetary surfaces. *Icarus*, *303*, 273–279. doi: 10.1016/j.icarus  
841 .2017.10.008
- 842 Makela, J. J., Lognonné, P., Hébert, H., Gehrels, T., Rolland, L., Allgeyer, S., . . .  
843 Lamouroux, J. (2011, July). Imaging and modeling the ionospheric air-  
844 glow response over Hawaii to the tsunami generated by the Tohoku earth-  
845 quake of 11 March 2011. *Geophysical Research Letters*, *38*(13), L00G02. doi:  
846 10.1029/2011GL047860
- 847 Margot, J.-L., Campbell, D. B., Giorgini, J. D., Jao, J. S., Snedeker, L. G., Ghigo,  
848 F. D., & Bonsall, A. (2021). Spin state and moment of inertia of venus. *Nature*  
849 *Astronomy*, *5*(7), 676–683. Retrieved from [http://dx.doi.org/10.1038/  
850 s41550-021-01339-7](http://dx.doi.org/10.1038/s41550-021-01339-7) doi: 10.1038/s41550-021-01339-7
- 851 Martinez, A., Lebonnois, S., Millour, E., Pierron, T., Moisan, E., Gilli, G., &  
852 Lefèvre, F. (2023). Exploring the variability of the venusian thermosphere with  
853 the IPSL Venus GCM. *Icarus*, *389*, 115272. doi: 10.1016/j.icarus.2022.115272
- 854 Mimoun, D., Murdoch, N., Lognonné, P., Hurst, K., Pike, W. T., Hurley, J., . . .  
855 Banerdt, W. B. (2017, October). The noise model of the SEIS seismometer of  
856 the InSight mission to Mars. *Space Science Reviews*, *211*(1–4), 383–428. doi:  
857 10.1007/s11214-017-0409-x
- 858 Moroz, V. I. (1983). Summary of preliminary results of the Venera 13 and Venera 14  
859 missions. In *Venus* (pp. 45–68). The University of Arizona Press.
- 860 Nachman, A. I., Smith III, J. F., & Waag, R. C. (1990). An equation for acous-  
861 tic propagation in inhomogeneous media with relaxation losses. *The Journal of*  
862 *the Acoustical Society of America*, *88*(3), 1584–1595. doi: 10.1121/1.400317
- 863 Näsholm, S. P., Iranpour, K., Wuestefeld, A., Dando, B. D., Baird, A. F., & Oye, V.  
864 (2022). Array signal processing on distributed acoustic sensing data: Direc-  
865 tivity effects in slowness space. *Journal of Geophysical Research: Solid Earth*,  
866 *127*(2), e2021JB023587. doi: 10.1029/2021JB023587
- 867 Neudeck, P. G., Spry, D. J., Krasowski, M. J., Prokop, N. F., Beheim, G. M., Chen,  
868 L.-Y., & Chang, C. W. (2018). Year-long 500° C operational demonstration  
869 of up-scaled 4H-SiC JFET integrated circuits. *Journal of Microelectronics and*  
870 *Electronic Packaging*, *15*(4), 163–170.
- 871 Noe, S., Yuan, S., Montagner, J. P., & Igel, H. (2022, May). Anisotropic elastic  
872 parameter estimation from multicomponent ground-motion observations: a

- 873 theoretical study. *Geophysical Journal International*, 229(2), 1462–1473. doi:  
874 10.1093/gji/ggac006
- 875 Occhipinti, G., Coisson, P., Makela, J. J., Allgeyer, S., Kherani, A., Hebert, H., &  
876 Lognonné, P. (2011, July). Three-dimensional numerical modeling of tsunami-  
877 related internal gravity waves in the Hawaiian atmosphere. *Earth, Planets and*  
878 *Space*, 63(7), 847–851. doi: 10.5047/eps.2011.06.051
- 879 Parker, A. R., Chan, H. M., Lopez-Zepeda, J., & Schallhorn, P. A. (2024). Design,  
880 fabrication, testing and validation of a ruggedized fiber optics sensing system  
881 (foss) for launch application. In *Aiaa scitech 2024 forum* (p. 2268).
- 882 Petculescu, A. (2016). Acoustic properties in the low and middle atmospheres of  
883 mars and venus. *The Journal of the Acoustical Society of America*, 140(2),  
884 1439–1446. doi: <https://doi.org/10.1121/1.4960784>
- 885 Peterson, J. (1993). *Observation and modeling of background seismic noise*. U.S.  
886 Geol. Surv. Open-File Rept. 92-322. Albuquerque.
- 887 Reinsch, T., & Hennings, J. (2010). Temperature-dependent characterization of  
888 optical fibres for distributed temperature sensing in hot geothermal wells. *Mea-*  
889 *surement Science and Technology*, 21(9), 094022.
- 890 Samuel, H., Drilleau, M., Rivoldini, A., Xu, Z., Huang, Q., Garcia, R. F., ...  
891 Banerdt, W. B. (2023, October). Geophysical evidence for an enriched  
892 molten silicate layer above Mars’s core. *Nature*, 622(7984), 712–717. doi:  
893 10.1038/s41586-023-06601-8
- 894 Schmelzbach, C., Donner, S., Igel, H., Sollberger, D., Taufiqurrahman, T., Bernauer,  
895 F., ... Robertsson, J. (2018, May). Advances in 6C seismology: Appli-  
896 cations of combined translational and rotational motion measurements in  
897 global and exploration seismology. *Geophysics*, 83(3), WC53–WC69. doi:  
898 10.1190/geo2017-0492.1
- 899 Seiff, A., & Kirk, D. B. (1991). Waves in Venus’ middle and upper atmosphere; Im-  
900 plication of Pioneer Venus probe data above the clouds. *Journal of Geophysical*  
901 *Research*, 96(A7), 11021–11032. doi: 10.1029/91JA01101
- 902 Smrekar, S., Hensley, S., Nybakken, R., Wallace, M., Perkovic-Martin, D., You, T.-  
903 H., ... Mazarico, E. (2022). VERITAS (Venus Emissivity, Radio Science,  
904 InSAR, Topography, and Spectroscopy): A discovery mission. In *2022 ieee*  
905 *aerospace conference (aero)*. IEEE. Retrieved from [http://dx.doi.org/](http://dx.doi.org/10.1109/aero53065.2022.9843269)  
906 [10.1109/aero53065.2022.9843269](http://dx.doi.org/10.1109/aero53065.2022.9843269) doi: 10.1109/aero53065.2022.9843269
- 907 Smrekar, S. E., Ostberg, C., & O’Rourke, J. G. (2023). Earth-like lithospheric thick-  
908 ness and heat flow on Venus consistent with active rifting. *Nature Geoscience*,  
909 16(1), 13–18. doi: 10.1038/s41561-022-01068-0
- 910 Smrekar, S. E., Stofan, E. R., Mueller, N., Treiman, A., Elkins-Tanton, L., Helbert,  
911 J., ... Drossart, P. (2010). Recent hotspot volcanism on Venus from VIRTIS  
912 emissivity data. *Science*, 328(5978), 605–608. doi: 10.1126/science.1186785
- 913 Sollberger, D., Bradley, N., Edme, P., & Robertsson, J. O. A. (2023, July). Efficient  
914 wave type fingerprinting and filtering by six-component polarization analysis.  
915 *Geophysical Journal International*, 234(1), 25–39. doi: 10.1093/gji/ggad071
- 916 Stähler, S. C., Khan, A., Banerdt, W. B., Lognonné, P., Giardini, D., Ceylan, S., ...  
917 Smrekar, S. E. (2021, July). Seismic detection of the martian core. *Science*,  
918 373(6553), 443–448. doi: 10.1126/science.abi7730
- 919 Stevenson, D., Cutts, J., MimounDavid, Arrowsmith, S., Banerdt, B., Blom, P., ...  
920 Tsai, V. (2015, April). *Probing the interior structure of Venus* (Tech. Rep.).  
921 Keck Institute for Space Studies: Venus Seismology Study Team.
- 922 Stolov, A., & OFS. (2019, 1). *Testing Optical Fiber: Undersea and Downhole Ap-*  
923 *plications*. Retrieved from [https://www.photonics.com/Articles/Testing](https://www.photonics.com/Articles/Testing-Optical-Fiber-Undersea-and-Downhole/p5/v170/i1115/a64288)  
924 [\\_Optical-Fiber-Undersea-and-Downhole/p5/v170/i1115/a64288](https://www.photonics.com/Articles/Testing-Optical-Fiber-Undersea-and-Downhole/p5/v170/i1115/a64288)
- 925 Surkov, Y. A., Barsukov, V., Moskalyeva, L., Kharyukova, V., & Kemurdzhian, A.  
926 (1984). New data on the composition, structure, and properties of Venus rock  
927 obtained by Venera 13 and Venera 14. *Journal of Geophysical Research: Solid*

- 928 *Earth*, 89(S02), B393–B402.
- 929 Sutin, B. M., Cutts, J., Didion, A. M., Drilleau, M., Grawe, M., Helbert, J., ...  
 930 Wallace, M. (2018, July). VAMOS: a SmallSat mission concept for re-  
 931 mote sensing of Venusian seismic activity from orbit. In M. Lystrup,  
 932 H. A. MacEwen, G. G. Fazio, N. Batalha, N. Siegler, & E. C. Tong (Eds.),  
 933 *Space telescopes and instrumentation 2018: Optical, infrared, and millimeter*  
 934 *wave* (Vol. 10698, p. 106985T). doi: 10.1117/12.2309439
- 935 Tian, Y., Herrick, R. R., West, M. E., & Kremic, T. (2023). Mitigating Power and  
 936 Memory Constraints on a Venusian Seismometer. *Seismological Research Let-*  
 937 *ters*, 94(1), 159–171. doi: 10.1785/0220220085
- 938 Trahan, A. J., & Petculescu, A. (2020). Absorption of infrasound in the lower and  
 939 middle clouds of Venus. *The Journal of the Acoustical Society of America*,  
 940 148(1), 141–152. doi: 10.1121/10.0001520
- 941 Van Zelst, I. (2022). Comment on “Estimates on the frequency of volcanic erup-  
 942 tions on Venus” by Byrne & Krishnamoorthy (2022). *Journal of Geophysical*  
 943 *Research: Planets*, 127(12), e2022JE007448. doi: 10.1029/2022JE007448
- 944 Van Zelst, I., Maia, J., Plesa, A.-C., Ghail, R., & Spühler, M. (2024). Estimates on  
 945 the possible annual seismicity of Venus [preprint]. *EarthArXiv*. doi: 10.31223/  
 946 X5DQ0C
- 947 Walter, F., Gräff, D., Lindner, F., Paitz, P., Köpffi, M., Chmiel, M., & Fichtner,  
 948 A. (2020). Distributed acoustic sensing of microseismic sources and wave  
 949 propagation in glaciated terrain. *Nature communications*, 11(1), 2436. doi:  
 950 10.1038/s41467-020-15824-6
- 951 Wang, H. F., Zeng, X., Miller, D. E., Fratta, D., Feigl, K. L., Thurber, C. H., &  
 952 Mellors, R. J. (2018). Ground motion response to an ML 4.3 earthquake using  
 953 co-located distributed acoustic sensing and seismometer arrays. *Geophysical*  
 954 *Journal International*, 213(3), 2020–2036. doi: 10.1093/gji/ggy102
- 955 Widemann, T., Straume-Lindner, A. G., Ocampo, A., Voirin, T., Carter, L., Hens-  
 956 ley, S., ... Dumoulin, C. (2022). EnVision: a nominal science phase spanning  
 957 six Venus sidereal days (four earth years). In *Agu fall meeting abstracts* (Vol.  
 958 2022, pp. P55B–05).
- 959 Wilson, C. F., Zetterling, C.-M., & Pike, W. T. (2016). Venus long-life surface pack-  
 960 age. White paper submitted in response to ESA’s call for new scientific ideas.  
 961 *arXiv e-prints*, arXiv:1611.03365. doi: 10.48550/arXiv.1611.03365
- 962 Xu, Z., Broquet, A., Fuji, N., Kawamura, T., Lognonné, P., Montagner, J.-P., ...  
 963 Banerdt, W. B. (2023, April). Investigation of Martian regional crustal struc-  
 964 ture near the dichotomy using S1222a surface-wave group velocities. *Geophysi-*  
 965 *cal Research Letters*, 50(8), e2023GL103136. doi: 10.1029/2023GL103136
- 966 Zhan, Z. (2020). Distributed acoustic sensing turns fiber-optic cables into sensitive  
 967 seismic antennas. *Seismological Research Letters*, 91(1), 1–15. doi: 10.1785/  
 968 0220190112
- 969 Zharkov, V. N. (1983, October). Models of the internal structure of Venus. *Moon*  
 970 *and Planets*, 29(2), 139–175. doi: 10.1007/BF00928322

1           **Seismic wave detectability on Venus using ground**  
2           **deformation sensors, infrasound sensors on balloons**  
3           **and airglow imagers**

4           **Raphael F. Garcia<sup>1</sup>, Iris van Zelst<sup>2,3</sup>, Taichi Kawamura<sup>4</sup>, Sven Peter**  
5           **Näsholm<sup>5,6</sup>, Anna Horleston<sup>7</sup>, Sara Klaasen<sup>8</sup>, Maxence Lefèvre<sup>9</sup>, Celine Marie**  
6           **Solberg<sup>5</sup>, Krystyna T. Smolinski<sup>8</sup>, Ana-Catalina Plesa<sup>2</sup>, Quentin Brissaud<sup>6</sup>,**  
7           **Julia S. Maia<sup>2</sup>, Simon C. Stähler<sup>8</sup>, Philippe Lognonné<sup>4</sup>, Mark Panning<sup>10</sup>,**  
8           **Anna Gülcher<sup>10,11</sup>, Richard Ghail<sup>12</sup>, Barbara De Toffoli<sup>13,14</sup>**

9           <sup>1</sup>Institut Supérieur de l'Aéronautique et de l'Espace ISAE-SUPAERO, Université de Toulouse

10           <sup>2</sup>Institute of Planetary Research, German Aerospace Center (DLR), Berlin, Germany

11           <sup>3</sup>Centre of Astronomy and Astrophysics, Technical University of Berlin, Berlin, Germany

12           <sup>4</sup>Université Paris Cité, Institut de physique du globe de Paris, CNRS, Paris, France

13           <sup>5</sup>Department of Informatics, University of Oslo, Oslo, Norway

14           <sup>6</sup>NORSAR, Kjeller, Norway

15           <sup>7</sup>School of Earth Sciences, University of Bristol, Bristol, UK

16           <sup>8</sup>ETH Zürich, Switzerland

17           <sup>9</sup>LATMOS/IPSL, Sorbonne Université, UVSQ Université Paris-Saclay, CNRS, Paris, France

18           <sup>10</sup>Jet Propulsion Laboratory, California Institute of Technology, Pasadena, USA

19           <sup>11</sup>Seismological Laboratory, California Institute of Technology, Pasadena, USA

20           <sup>12</sup>Royal Holloway, University of London, London, UK

21           <sup>13</sup>INAF, Istituto di Astrofisica e Planetologia Spaziali, Rome, Italy

22           <sup>14</sup>Department of Geosciences, University of Padova, Padova, Italy

23           **Key Points:**

- 24           • The capabilities of various measurement concepts to detect quakes on Venus are  
25           estimated and compared to recent Venus seismicity estimates
- 26           • Ground sensors are limited by their short measurement duration, but also by a  
27           minimum noise level that may be below atmosphere induced noise
- 28           • Atmospheric seismology concepts are limited to large quake magnitudes, and air-  
29           glow imagers are favored relative to balloon measurements

---

Corresponding author: Raphaël F. Garcia, [raphael.garcia@isae-supero.fr](mailto:raphael.garcia@isae-supero.fr)

**Abstract**

The relatively unconstrained internal structure of Venus is a missing piece in our understanding of the Solar System formation and evolution. To determine the seismic structure of Venus' interior, the detection of seismic waves generated by venusquakes is crucial, as recently shown by the new seismic and geodetic constraints on Mars' interior obtained by the InSight mission. In the next decades multiple missions will fly to Venus to explore its tectonic and volcanic activity, but they will not be able to conclusively report on seismicity or detect actual seismic waves. Looking towards the next fleet of Venus missions in the future, various concepts to measure seismic waves have already been explored in the past decades. These detection methods include typical geophysical ground sensors already deployed on Earth, the Moon, and Mars; pressure sensors on balloons; and airglow imagers on orbiters to detect ground motion, the infrasound signals generated by seismic waves, and the corresponding airglow variations in the upper atmosphere. Here, we provide a first comparison between the detection capabilities of these different measurement techniques and recent estimates of Venus' seismic activity. In addition, we discuss the performance requirements and measurement durations required to detect seismic waves with the various detection methods. As such, our study clearly presents the advantages and limitations of the different seismic wave detection techniques and can be used to drive the design of future mission concepts aiming to study the seismicity of Venus.

**Plain Language Summary**

We do not really know what the interior of Venus looks like. Even the first-order structure of the size of Venus' core is plagued with large uncertainties. For other planets, such as the Earth and Mars, the interior structure is much better constrained. This is largely thanks to the seismological investigations performed on these planets that revealed their interior structure by studying the seismic waves caused by quakes. In the next decades, new missions will fly to Venus to explore its tectonic and volcanic activity, but they will not be able to detect any seismic waves. In order to help design future mission concepts, we discuss instruments that could record seismic waves, as already used on the Earth, the Moon, and Mars; instruments on balloons that could float in the Venusian atmosphere; and instruments on spacecrafts that monitor the variations of atmospheric emissions caused by seismic waves originating at the surface. We compare all these different techniques with each other and with recent estimates of Venus' seismic activity to see which of them works best in different scenarios.

**1 Introduction**

The internal structures of the planets are key information to better understand the formation and the evolution of our Solar System. Although Venus is similar to Earth in terms of size and mass, our knowledge of its internal structure is limited due to its slow rotation, which hinders the determination of its moment of inertia (Margot et al., 2021) and creates large error bars on Love number estimates (Dumoulin et al., 2017). The detection and characterization of seismic waves is the best tool to infer the internal structure of planets (Lognonné et al., 2023). However, the deployment of long-duration geophysical instrumentation, which demonstrated its capabilities during the InSight mission on Mars (Stähler et al., 2021; Durán, Khan, Ceylan, Zenhäusern, et al., 2022; Durán, Khan, Ceylan, Charalambous, et al., 2022; Drilleau et al., 2022; Samuel et al., 2023; Lognonné et al., 2023) is not possible on Venus due to its harsh surface conditions. At the same time, there is a growing number of studies that have presented evidence that Venus is volcanically and tectonically active at present (Smrekar et al., 2010; Gülcher et al., 2020; Byrne et al., 2021; Van Zelst, 2022; Smrekar et al., 2023; Herrick & Hensley, 2023) indicating that the planet is probably also seismically active. Indeed, recent estimates of

80 Venus' seismicity indicate that Venus could host hundreds of quakes per year with  $M_w \geq$   
 81 5 when Venus is assumed to be moderately active and potentially be as seismically ac-  
 82 tive as the Earth in its most extreme end-member scenario (Van Zelst et al., 2024).

83 Despite the compelling arguments in favor of monitoring seismic wave propagation  
 84 in Venus, none of the three missions scheduled by ESA and NASA to visit Venus in the  
 85 next decade (i.e., the EnVision (Widemann et al., 2022), VERITAS (Smrekar et al., 2022),  
 86 and DAVINCI+ (Garvin et al., 2022) missions) are targeting the detection of seismic waves.  
 87 This is primarily due to the challenges associated with conducting such measurements  
 88 for Venus. Over the past decade, various measurement concepts have been explored, falling  
 89 into three main categories: (i) ground deformation instruments deployed on the planet's  
 90 surface, (ii) infrasound sensors mounted on balloon platforms, and (iii) airglow imagers  
 91 on board orbiters (Stevenson et al., 2015). The concepts for ground surface deployment  
 92 of seismic sensors are limited by the high atmospheric surface temperature ( $\approx 740$  K) in  
 93 the absence of high temperature electronics. This limits the measurement duration to  
 94 a total amount of approximately one day (Kremic et al., 2020). Seismic infrasound de-  
 95 tection methods concern themselves with the low attenuation of upward-propagating in-  
 96 frasound waves created by seismic waves below 1 Hz (Garcia et al., 2005). These infra-  
 97 sounds conserve the dispersion features of seismic surface waves during their upward prop-  
 98 agation (Lognonné et al., 2016). These two properties allow us to assume that the in-  
 99 frasound created by seismic surface waves retains all the properties of seismic surface waves  
 100 that are necessary to determine the seismic velocity profile in the first hundreds of kilo-  
 101 meters depth of the planet, as it was done by InSight on Mars (Kim et al., 2022; Car-  
 102 rasco et al., 2023; Xu et al., 2023). Two different concepts based on the detection of seis-  
 103 mic infrasound have been investigated thoroughly in the past decade. First, pressure sen-  
 104 sors on board of balloon platforms have been studied (Stevenson et al., 2015; Krishnamoor-  
 105 thy & Bowman, 2023). Their capabilities to detect and characterise seismic waves have  
 106 been demonstrated theoretically and have even been observed on Earth recently for the  
 107 first time (Brissaud et al., 2021; Garcia et al., 2022). Secondly, airglow emission varia-  
 108 tions induced by seismically generated tsunami waves have been observed on Earth (Makela  
 109 et al., 2011; Occhipinti et al., 2011) and the sensitivity of airglow emissions to gravity  
 110 waves has been observed in Venus atmosphere (Garcia et al., 2009). Indeed, mission con-  
 111 cepts targeted to the observation of seismically-induced variations of  $1.27 \mu\text{m}$  nightglow  
 112 and  $4.3 \mu\text{m}$  dayglow in Venus' atmosphere have been developed (Stevenson et al., 2015;  
 113 Sutin et al., 2018).

114 The purpose of this study is to perform a first comparison between the capabili-  
 115 ties of all these diverse measurement techniques and the most recent estimates of Venus  
 116 seismicity. For each observation technique, we also discuss the minimum performance  
 117 and measurement duration. We focus on globally observable seismic waves for events of  
 118 moment magnitude larger than 3 ( $M_W > 3$ ).

## 119 **2 Estimating seismic wave detection capabilities of different observa-** 120 **tion concepts**

### 121 **2.1 Seismic signal estimates**

122 In the absence of internal structure models of Venus that are directly constrained  
 123 by data, the currently-used internal structure models of Venus are constrained by plan-  
 124 etary formation and geodynamic models, solar abundance estimates, and physical assump-  
 125 tions, and rely on the adaptation of Earth models to Venus conditions (Zharkov, 1983;  
 126 Gudkova & Zharkov, 2020). As a consequence, these models present a large uncertainty  
 127 in terms of both seismic velocities and seismic attenuation parameters. This is why we  
 128 choose to base our estimates of seismic wave amplitudes and frequency content on Earth's  
 129 scaling relations, rather than performing complex computations in highly uncertain mod-  
 130 els of the Venusian interior. Because seismic surface waves show the highest amplitude

131 for shallow quakes on Earth, we will assume that these waves are also dominating the  
 132 seismic signal on Venus in the quake magnitude range considered in this study, i.e., mo-  
 133 ment magnitudes larger than 3.0. In addition, since the dispersion of seismic surface waves  
 134 is strongly dependent on the seismic structure of the crust and the top of the mantle,  
 135 the observation of these waves is critical to constrain the structure of the first hundreds  
 136 of kilometers of Venus' interior. The definition of surface-wave magnitude,  $M_S$ , shows  
 137 a direct link with the amplitude of the seismic surface Rayleigh waves around the 20 s  
 138 period:

$$M_S = \log_{10} \left( \frac{A_d}{T_S} \right) + 1.66 \log_{10}(\Delta) + 3.3, \quad (1)$$

139 where  $M_S$  is the surface wave magnitude,  $A_d$  the vertical ground displacement in  $\mu m$ ,  
 140  $T_S$  is the period considered for measuring  $A_d$ , and  $\Delta$  is the epicentral distance of the quake  
 141 in degrees (Bormann & Dewey, 2012). We will use this relation to determine the am-  
 142 plitude of the surface Rayleigh waves as a function of distance for a given surface wave  
 143 magnitude.

## 144 2.2 Atmosphere effects and parameters

145 The detectability of infrasound by balloon platforms and airglow imagers is sensi-  
 146 tive to the amplitude of the source and atmospheric path effects (Garcia et al., 2005).  
 147 In particular, attenuation processes on Venus can strongly dampen and disperse the in-  
 148 frasound energy. To assess the impact of attenuation on acoustic waves, we determine  
 149 the energy loss vs. altitude for a vertically propagating planar wave. In the frequency  
 150 range of interest (0.01–1 Hz), the attenuation of infrasound in the Venusian atmosphere  
 151 is dominated by CO<sub>2</sub> relaxation effects (Bass & Chambers, 2001; Petculescu, 2016), al-  
 152 though some contributions are also expected from sulfuric acid (H<sub>2</sub>SO<sub>4</sub>) droplet-related  
 153 processes, primarily in the cloudy 45 to 70 km altitude regime (Trahan & Petculescu,  
 154 2020).

155 We compute atmospheric parameters using the Venus Climate Database (VCD)  
 156 (Gilli et al., 2017, 2021; Martinez et al., 2023) to estimate the attenuation due to CO<sub>2</sub>  
 157 relaxation,  $\alpha_{CO_2}(z)$ . We extract a single vertical profile of specific heats, and sound speed  
 158 is extracted at the equator at midday local time. From this VCD profile, we then use  
 159 the approach described in Garcia et al. (2017) to extract the CO<sub>2</sub> relaxation frequency  
 160 and relaxation strength, as well as the sound speed as a function of altitude. In low-attenuation  
 161 scenarios, it is appropriate to sum the attenuation contributions from CO<sub>2</sub> and H<sub>2</sub>SO<sub>4</sub>  
 162 (Nachman et al., 1990), to obtain the total attenuation  $\alpha_{tot}(z) = \alpha_{CO_2}(z) + \alpha_{H_2SO_4}(z)$ .  
 163 In Figure 1, we use these estimates to explore the amplitude loss using a plane-wave as-  
 164 sumption, focusing on acoustic waves at periods from 1 to 50 s from the ground up to  
 165 140 km altitude. A significant increase in attenuation occurs in the cloud layers, where  
 166 strong diffusion-mediated phase changes occur due to sulfuric acid droplets (Petculescu,  
 167 2016). Yet, our estimates suggest that attenuation has an insignificant impact on acous-  
 168 tic waves of periods larger than 1 second up to the bottom of the airglow layer IR1. At  
 169 the altitude of airglow layer IR2, longer-period waves of interest for airglow (10 s to 50 s  
 170 period) are not damped much. However, at this altitude, a significant energy loss of ~50%  
 171 is predicted, which dramatically reduces the likelihood of detection for 1 s period waves.  
 172 Note that this analysis assumes linear acoustics and takes neither nonlinear propagation  
 173 nor wave-breaking effects into account.

## 174 2.3 Estimating the minimum number of events per magnitude per year

175 In this section, we provide detection thresholds that can be directly compared to  
 176 seismicity estimates (Van Zelst et al., 2024). To do so, we estimate the requirements to  
 177 detect at least one event larger than a given magnitude during the full mission duration.

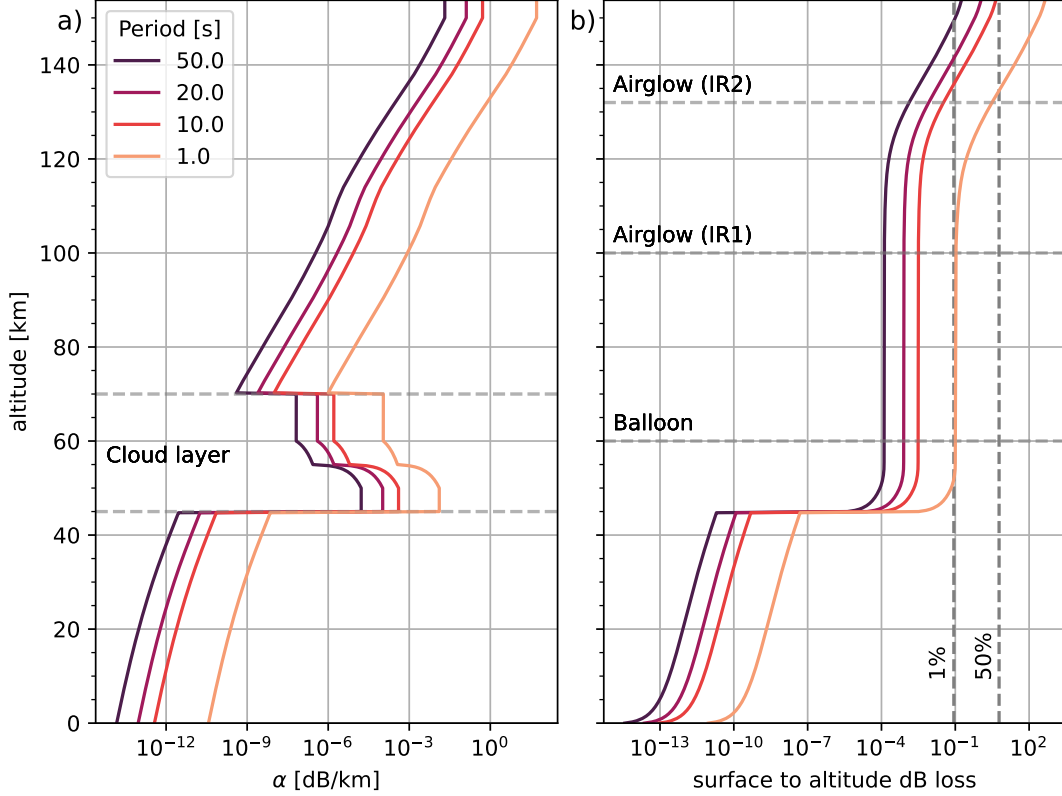


**Figure 1.** (a) plane-wave infrasound attenuation ( $\alpha$  in dB/km) based on a Venus Climate Database (VCD) atmospheric profile, including both the  $\alpha_{\text{H}_2\text{SO}_4}$  and the  $\alpha_{\text{CO}_2}$  contributions, and the sulfuric acid cloud contributions given in Trahan and Petculescu (2020). We consider wave periods from 1 to 50 s. (b) The total loss (in dB) due to the attenuation in (a), integrated from the ground up to the given altitude. The two vertical dashed lines indicate accumulated amplitude losses of 1% and 50%.

178 Assuming the seismic events to be Poisson distributed and setting our desired probabil-  
 179 ity of detection at 63% yields the following relation for a signal-to-noise ratio threshold  
 180 of one:

$$N_m^{\min}(M_S) = \frac{1}{T_m} \frac{S_P}{S_m(M_S)}, \quad (2)$$

181 where  $T_m$  is time in Earth years,  $S_P$  is the surface area of Venus, and  $*_m$  signifies method  
 182  $m$ :  $s$  for seismometer,  $r$  for ground rotation sensor,  $d$  for ground Distributed Acoustic  
 183 Sensing (DAS),  $b$  for pressure sensors on board balloons and  $a$  for airglow imagers. Us-  
 184 ing this relation, the surface area  $S_m(M_S)$  over which a quake of a given surface-wave  
 185 magnitude  $M_S$  can be detected by a given method is investigated in the following sec-  
 186 tions.

187 This relation is only valid statistically with a 63% confidence interval if we assume  
 188 that the seismic events have a Poisson distribution. Moreover, it is assumed that the seis-  
 189 mic event probability is homogeneous over the Venus surface, which is unrealistic, but  
 190 a starting point at a time when no actual mission concept is evaluated. Our estimates  
 191 thus provide a lower bound of the detection limits of each measurement concept.

192 In order to estimate  $\frac{S_P}{S_m(M_S)}$ , we need to estimate a maximum distance  $\Delta_m(M_S)$ ,  
 193 usually in degrees, at which the event can be detected for the different methods, within  
 194 a signal-to-noise ratio larger than a given value  $\text{SNR}_{\min}$ . Knowing this number, the sur-  
 195 face area ratio is

$$\frac{S_P}{S_m(M_S)} = \frac{4\pi}{2\pi(1 - \cos(\Delta_m(M_S)))}, \quad (3)$$

196 with  $\Delta_m(M_S)$  the maximum epicentral distance at which you can expect to detect the  
 197 quake.

198 Usually, the noise levels of the instruments are provided in Power of Amplitude Spectral  
 199 Density (ASD) in physical unit over square root of hertz ( $\text{ASD}_n$ ). In contrast, the  
 200 signal amplitude terms in Equation 1 are provided at a given period ( $T_S$ ), and consequently  
 201 the signal amplitude on the instrument is also in physical units at a given period ( $A_m$ ).  
 202 In order to compare these two numbers, we convert the amplitude spectral density val-  
 203 ues into root-mean-square values, under the conservative hypothesis that we filter the  
 204 signals over a bandwidth of 1/3 octave ( $\pm 11.5\%$ ) around the central frequency  $f_S = \frac{1}{T_S}$ .  
 205 As a consequence, the root-mean-square noise amplitude is defined by the product of the  
 206 amplitude spectral density times the square root of the frequency bandwidth, assuming  
 207 that the noise power is constant over the bandwidth (Bormann, 2002):

$$N_{\text{rms}} = \text{ASD}_n \sqrt{\frac{0.23}{T_S}}. \quad (4)$$

208 As a consequence, the maximum epicentral distance at which you can expect to detect  
 209 a quake of magnitude  $M_S$  ( $\Delta_m(M_S)$ ) is defined by equating the signal-to-noise ratio to  
 210 its minimum value  $\text{SNR}_{\min}$ , fixed here to 3:

$$\frac{A_m(\Delta_m(M_S))}{N_{\text{rms}}} = \text{SNR}_{\min}. \quad (5)$$

211 In conclusion, in order to estimate  $N_m^{\min}(M_S)$ , i.e., the minimum number of events per  
 212 year, as a function of surface wave magnitude, to measure at least 1 event of this type  
 213 by a given method, one needs to invert the above equations to get the maximum distance  
 214 at which an event can be detected by a given method  $\Delta_m(M_S)$ , and then compute  $N_m^{\min}(M_S)$   
 215 through Equations 3 and 2. However, because the relation of Equation 1 holds only for  
 216 teleseismic distances, and because we need the waves to be separated in time in order  
 217 to analyze them properly, we impose  $\Delta_m(M_S) > 3^\circ$ . This restriction sets the lower-bound  
 218 limit on the  $M_S$  values.

## 219 **2.4 Detection capabilities of various observation concepts**

### 220 **2.4.1 Quake detection by landed seismometer**

221 Due to the high surface temperatures on Venus and the limited amount of solar en-  
 222 ergy that reaches the surface, deploying instruments on the ground is challenging. With  
 223 conventional electronics, surface landers lasted less than two hours on the Venusian sur-  
 224 face in the past (Kerzhanovich & Marov, 1983; Moroz, 1983). However, to be able to de-  
 225 termine global seismicity levels, several Earth days of active monitoring would proba-  
 226 bly be required at minimum.

227 Recent advances in high-temperature electronics (Wilson et al., 2016; Kremic et  
 228 al., 2020; Glass et al., 2020) have made long-lived landers a possibility for the coming  
 229 decades, using silicon carbide (SiC) seismometers. These SiC integrated circuits have been  
 230 demonstrated to provide 60 functioning days in high-fidelity simulated Venusian surface  
 231 conditions (Hunter et al., 2021; Chen et al., 2019; Neudeck et al., 2018). However, the

232 development of the associated electronics coping with the harsh Venus conditions is still  
 233 required.

234 Memory is another issue with Venusian surface conditions. Depending on power  
 235 availability, data storage and transmission could be difficult. Tian et al. (2023) designed  
 236 a low-memory algorithm to circumvent this issue that triggers transmission during earth-  
 237 quakes and avoids transmission during wind and other noise events (Tian et al., 2023).

238 Only a handful of probes recorded data at the surface of Venus. Only VENERA-  
 239 9 and 10 directly measured the wind for 49 min and 90 s, respectively (Avduevskii et  
 240 al., 1977), and VENERA-13 and 14 indirectly measured the wind speed (Ksanfomaliti  
 241 et al., 1983). The amplitudes of the measured wind speeds are less than  $2 \text{ m s}^{-1}$  below  
 242 100 m height (Lorenz, 2016), with a higher probability for values below  $0.5 \text{ m s}^{-1}$ .

243 Simulations with a global circulation model showed the diurnal cycle of the Plan-  
 244 etary Boundary Layer (PBL) activity is correlated with the diurnal cycle of surface winds  
 245 (Lebonnois et al., 2018), with downward katabatic winds at night and upward anabatic  
 246 winds during the day along the slopes of high-elevation terrains. With a high-resolution  
 247 model, Lefèvre et al. (2024) confirmed this diurnal cycle of the surface wind. The resolved  
 248 large-scale horizontal wind at 10 m above the local surface is above  $1 \text{ m s}^{-1}$  in the moun-  
 249 tains in the equatorial region and below  $0.5 \text{ m s}^{-1}$  in the low plains.

250 Lefèvre (2022) used a turbulent-resolving model to quantify the turbulent activ-  
 251 ity at the surface of Venus. At noon, the height of the PBL varies from 1.5 km in the  
 252 plains to 7 km in the high terrains by the equator. This difference is due to the impact  
 253 of the anabatic winds. This difference in PBL height at noon, results in a difference in  
 254 turbulent horizontal winds amplitude, reaching  $2 \text{ m s}^{-1}$  for the high terrain compared  
 255 to between 1 and  $1.5 \text{ m s}^{-1}$  in the plains. At night, when the impact of the slope winds  
 256 is weaker, the height of the PBL is almost the same around 500 m, resulting in horizon-  
 257 tal winds amplitude below  $0.5 \text{ m s}^{-1}$ . Placing a seismometer in the low plain, and record-  
 258 ing signals by night, seems to be the optimal plan to limit the noise of the atmosphere.

259 Lorenz (2012) roughly quantified the wind noise at the surface of Venus. With an  
 260 atmospheric density of  $65 \text{ kg/m}^3$ , a wind speed of  $0.25 \text{ m s}^{-1}$  is comparable in terms of  
 261 dynamic pressure to wind speeds of  $20 \text{ m s}^{-1}$  on Mars, which were regularly observed  
 262 during the daytime by InSight (Banfield et al., 2020) The corresponding seismic ampli-  
 263 tude is 120.0 nm. Atmospheric noise could therefore limit seismic detection, and shield-  
 264 ing the instrument might be necessary.

265 Venera-14 reportedly detected Venusian microseisms with a geophone in only an  
 266 hour of operation (Ksanfomaliti et al., 1982). The amplitude of the signals are consis-  
 267 tent with ‘noisy’ environments on Earth (Lorenz & Panning, 2018), i.e. from  $\sim 10^{-8}$  to  
 268  $10^{-6} \text{ m/s}^2/\sqrt{\text{Hz}}$  which roughly spans the space between the low and high noise mod-  
 269 els for Earth (Peterson, 1993). Therefore, surface-wind noise on Venus must be properly  
 270 quantified. In addition, it is important to note that for high-quality seismic measurements,  
 271 the wind speed and pressure should be monitored continuously.

272 The Brownian noise of a Short Period (SP) sensor comparable to the InSight sen-  
 273 sor (Lognonné et al., 2019) in a vacuum is modeled to have an acceleration noise den-  
 274 sity of  $\sqrt{\frac{k_B T \alpha}{m}}$  where  $k_B$  is Boltzmann’s constant,  $T$  the absolute temperate,  $\alpha$  the damp-  
 275 ing constant, and  $m$  the proof mass (Mimoun et al., 2017). For a standard SP, the proof  
 276 mass is 0.8 g. Recalculating from Mimoun et al. (2017) with  $T = 740 \text{ K}$ , gives a noise  
 277 of  $4.37 \cdot 10^{-10} \text{ m/s}^2/\sqrt{\text{Hz}}$ . If not in a vacuum, the suspension noise also includes a vis-  
 278 cous damping term which could contribute. At 740 K, this additional term reaches  $3.3 \cdot$   
 279  $10^{-9} \text{ m/s}^2/\sqrt{\text{Hz}}$ , giving a total suspension noise of  $3.77 \cdot 10^{-9} \text{ m/s}^2/\sqrt{\text{Hz}}$ , lower than  
 280 the atmospheric noise. Other sensor noise sources should also be considered and prop-  
 281 erly calculated for the Venusian environment, such as digitizer/acquisition noise, ther-

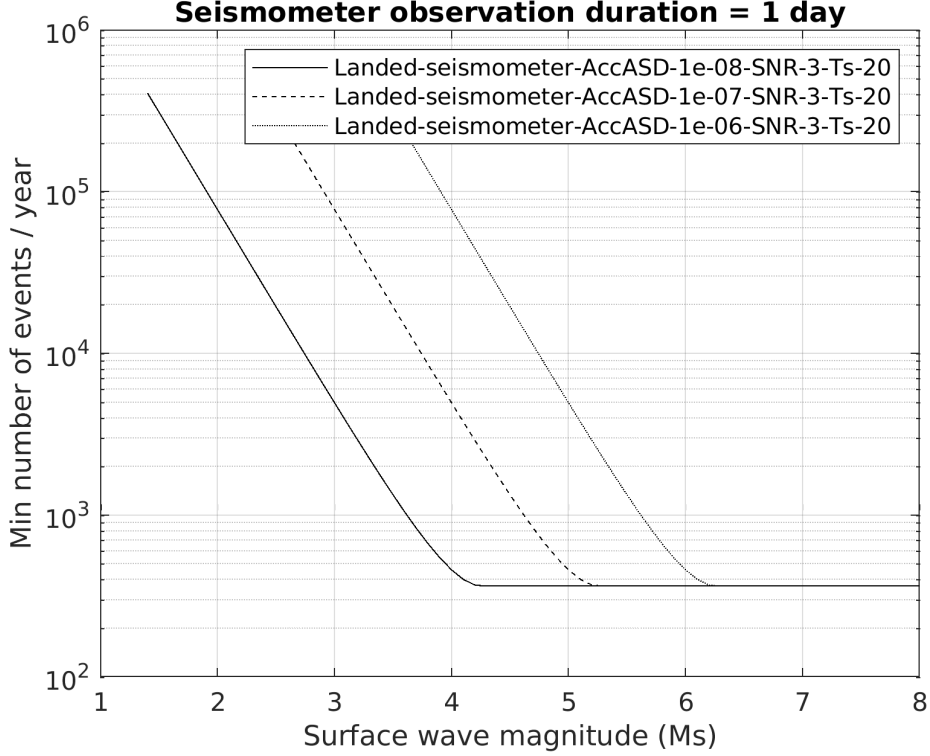


**Figure 2.** Minimum number of events per year as a function of surface wave magnitude required on the surface of Venus to measure at least one event of this magnitude during a seismometer observation duration of 1 day. Results are provided for different noise levels:  $10^{-8}$  (plain line) and  $10^{-7}$  (dashed line),  $10^{-6}$  (dotted line)  $\text{m/s}^{-2}/\sqrt{\text{Hz}}$  at 20 s period.

mal noise, noise from wind on the sensor, and atmospheric noise/noise of the lander itself.

With an  $SNR_{min}$  set to 3 and a period  $T_s$  of 20 s,  $\Delta_m(M_S)$  can be estimated for a given magnitude from Equations 1 and 5 as:

$$\log_{10}(\Delta_m(M_S)) = \frac{M_s - 3.3 - \log_{10}\left(\frac{SNR_{min} N_{rms}}{T_s}\right)}{1.66}. \quad (6)$$

Following Equations 2 and 3, the minimum number of events for each magnitude on the surface of Venus to result in at least one detection during the mission lifetime is shown in Figure 2. For the lowest noise level estimated to be  $10^{-8} \text{ m/s}^2/\sqrt{\text{Hz}}$ , global detection is possible for surface wave magnitudes above  $M_s = 4.3$ . For a higher noise level, this limit increases to  $M_s = 5.3$  for  $10^{-7} \text{ m/s}^2/\sqrt{\text{Hz}}$  and to  $M_s = 6.3$  for  $10^{-6} \text{ m/s}^2/\sqrt{\text{Hz}}$ . Under our idealized conditions, events above this threshold need to occur just once during the mission to be detectable, which creates the lower limit of 365 events per year in fig. 2.

#### 2.4.2 Quake detection with DAS on the surface

Distributed Acoustic Sensing (DAS) is an emerging technology in the field of Earth geophysics, and has been applied in increasingly remote and harsh locations on Earth,

such as glaciers (Walter et al., 2020; Hudson et al., 2021), volcanoes (Klaasen et al., 2021; Jousset et al., 2022; Klaasen et al., 2023) and submarine environments (Cheng et al., 2021; Lior et al., 2021). It employs a fiber-optic cable that is interrogated with laser pulses, resulting in seismic deformation measurements at a high spatial and temporal resolution along the cable. We refer the reader to Zhan (2020), and Lindsey and Martin (2021) for more in-depth descriptions of DAS and its applications on Earth. We optimistically propose to extend the use of DAS beyond Earth, and to visualize the hypothetical detection capabilities of DAS on Venus.

We follow the procedures as outlined in Section 2.3 to obtain the detection capabilities for DAS on Venus, as shown in Figure 3. We estimate the minimum number of required events per year based on parameters and assumptions similar to the ones used for the landed seismometer in Section 2.4.1. On top of the noise estimates of  $10^{-8}$ ,  $10^{-7}$  and  $10^{-6}$   $\text{m/s}^2/\sqrt{\text{Hz}}$ , we also use the noise-floor in strain as reported by the iDAS Carina from Silixa, as an example of the self-noise of an interrogator currently on the market. The noise estimates in  $\text{m/s}^2/\sqrt{\text{Hz}}$  are transformed from ground acceleration to strain using the plane-wave assumption (Daley et al., 2016; Wang et al., 2018; Näsholm et al., 2022), assuming an apparent velocity of seismic surface waves of 2250 m/s, which corresponds to an approximate Rayleigh wave velocity in mid-oceanic ridge basaltic material at 20 second period (as suggested for Venus; Surkov et al., 1984) with a Poisson ratio of 0.25:

$$\epsilon = aT_S/V_R, \quad (7)$$

where  $\epsilon$  is the strain,  $a$  is the acceleration in  $\text{m/s}^2$  which is linked to a given quake magnitude by Equation 1,  $T_S$  is the period of the wave in s, and  $V_R$  is the Rayleigh wave velocity in m/s. The entire calculation is then based on the values in strain; the native unit of a DAS interrogator.

While the calculation based on different noise estimates paints an optimistic picture, we emphasize that a DAS deployment on Venus is at the moment not feasible due to several obstacles, such as (i) the current instrumental capacities, (ii) deployment options, (iii) cable coupling conditions, and (iv) unknown cable locations. The instruments currently on the market are not able to operate under the pressure and temperature at the surface of Venus. However, some experiments have demonstrated the ability of specialized gold-coated optical fibers to survive and function with low attenuation at temperatures up to 773 K for up to 900 hours (Jacobsen et al., 2018), with optical fiber manufacturers also quoting operating temperatures up to 973 K (e.g. (Heracle, 2023)). The development of high-temperature and corrosion-resistant fibers is an area of active research, for example within the oil and gas industry (Reinsch & Hennings, 2010; Stolov & OFS, 2019)). Alternative fiber optic sensing systems are also already in development for structural health monitoring on future spacecraft (Chan et al., 2015; Parker et al., 2024).

Assuming the further development of DAS instruments and their ability to operate on Venus, we are limited by the deployment of the cable. If the cable is released during the landing, we are unable to control the exact layout and coupling conditions of the cable, which will likely decrease the data quality and the consequent conclusions that can be drawn from the data. If the cable is not buried and protected, other noise sources are likely to overpower any seismic signals - a phenomenon observed on Earth with atmospheric noise, in submarine environments with strong currents (Lior et al., 2021), or on Mars with the atmospheric wind and pressure noise (Mimoun et al., 2017). Additionally, DAS yields single-component data, therefore a cable layout with varying angles and directions is necessary to capture the complete wavefield and locate events. However, this also requires exact geographical knowledge of the cable layout, which may be difficult

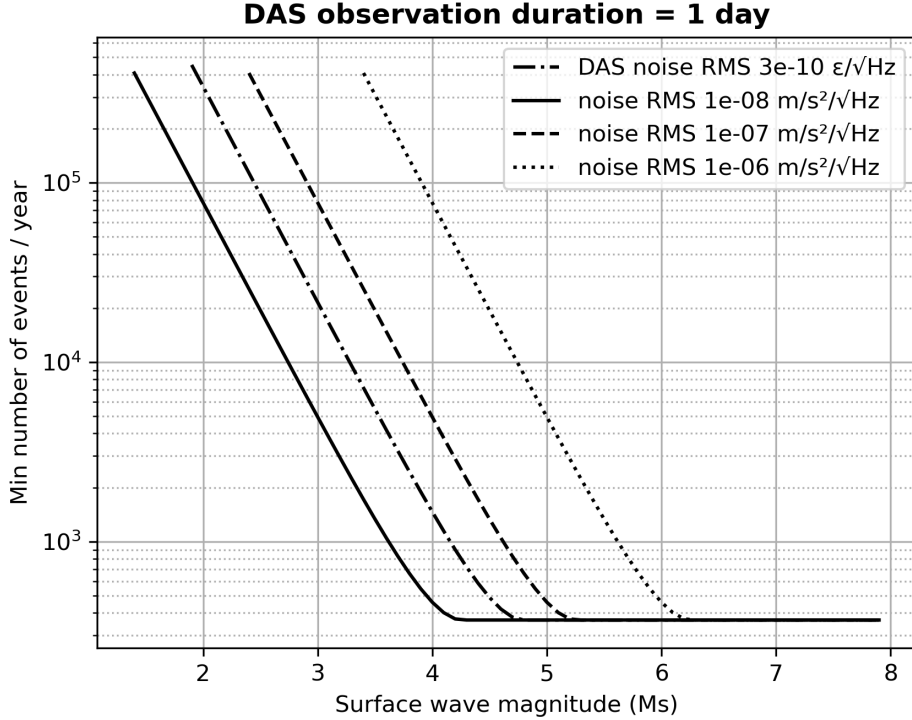


**Figure 3.** Minimum number of events per year as a function of surface wave magnitude required to measure at least one event of this magnitude during a DAS observation duration of 1 day. Results are provided for different noise levels:  $10^{-8}$  (plain line) and  $10^{-7}$  (dashed line),  $10^{-6}$  (dotted line)  $\text{m/s}^{-2}/\sqrt{\text{Hz}}$  at 20 s period. An estimate assuming that the noise floor is controlled by a typical self noise of a DAS interrogator (iDAS Carina of Silixa company) is provided as dotted-dashed lines.

346 to obtain on Venus due to the lack of a GPS network and difficulty capturing georeferenced images of the cable.  
347

348 Hence, in order to facilitate a DAS experiment on Venus, research primarily needs  
349 to focus on instrumental development and the feasibility of experimental deployment.  
350 The instrument needs to be able to operate its laser and conduct preliminary data analysis  
351 before sending the data back to orbit to avoid, in order to avoid a bottle neck caused  
352 by the large amounts of data produced by DAS experiments. Additionally, the cable needs  
353 to be deployed in such a fashion to guarantee atmospheric protection and good coupling  
354 with the ground, and would ideally have a well-known, and non-linear layout.

### 355 *2.4.3 Quake detection with ground rotation sensors*

356 The sensing of the ground rotations induced by seismic waves is an emerging field.  
357 The ground rotations allow for inferring the gradients of the seismic wavefield. These  
358 measurements allow seismologists to distinguish between various seismic waves (Sollberger  
359 et al., 2023), to correct for tilt effects on seismometers (Bernauer, Wassermann, & Igel,  
360 2020) and to infer anisotropy parameters (Noe et al., 2022). There are also many other  
361 applications for inverse problems and seismic source determination (Schmelzbach et al.,  
362 2018). This domain is currently limited by the self-noise level of the instruments (Bernauer

363 et al., 2021) and planetary applications are promising but mainly limited by the avail-  
 364 able instrumentation (Bernauer, Garcia, et al., 2020).

365 The currently available instruments are measuring the ground rotation speed in rad/s  
 366 ( $\omega$ ) along three perpendicular axis. With the same assumption as those used in the pre-  
 367 vious section to estimate the ground strain, this parameter can be linked to the ground  
 368 acceleration by the following equation

$$\omega = aT_S/(2\pi\lambda), \quad (8)$$

369 where  $\omega$  is the ground rotation in rad/s,  $a$  the acceleration in  $\text{m/s}^2$ ,  $T_S$  the period of the  
 370 surface wave in s, and  $\lambda$  the wavelength in meters which is computed assuming a sur-  
 371 face wave velocity of 2250 m/s.

372 We follow the procedures as outlined in Section 2.3 to obtain the detection capa-  
 373 bilities for ground rotation sensors on Venus as shown in Figure 4. We estimate the min-  
 374 imum number of required events per year based on parameters and assumptions simi-  
 375 lar to the ones used for the landed seismometer in Section 2.4.1. On top of the noise es-  
 376 timates of  $10^{-8}$ ,  $10^{-7}$  and  $10^{-6}$   $\text{m/s}^2/\sqrt{\text{Hz}}$ , we also use the noise-floor in rad/s as re-  
 377 ported for the BlueSeis3A sensor from the iXblue company ( $20 \text{ nrad/s}/\sqrt{\text{Hz}}$ ), as an ex-  
 378 ample of the self-noise of a rotation sensor on the market.

379 As observed in Figure 4, the event detection is limited by the self-noise of current  
 380 ground rotation instruments (Bernauer, Garcia, et al., 2020). As a consequence, even if  
 381 the ground rotation measurements present less deployment constraints than the DAS sys-  
 382 tems, the interest of such measurements is limited to large-amplitude signals, and thus  
 383 to large-amplitude quakes close to the instrument.

#### 384 **2.4.4 Quake detection by pressure sensors onboard balloons**

385 Stratospheric balloon flights on Earth present noise levels around  $0.05 \text{ Pa}/\sqrt{\text{Hz}}$  at  
 386 20 s period and  $0.01 \text{ Pa}/\sqrt{\text{Hz}}$  at 10 s period (Garcia et al., 2022). The amplitude of pres-  
 387 sure perturbations generated by a vertical displacement  $A_d$  (in  $\mu\text{m}$ ) at period  $T_S$  can be  
 388 computed using the following formula, assuming that the acoustic wave attenuation is  
 389 negligible (Garcia et al., 2005):

$$DP = \rho(z_b)c(z_b)\sqrt{\frac{\rho(0)c(0)}{\rho(z_b)c(z_b)}}\left(\frac{10^{-6}2\pi A_d}{T_S}\right) \quad (9)$$

390 in which  $\rho(z)$  and  $c(z)$  are the density and the sound speed at altitude  $z$  in the atmo-  
 391 sphere respectively. The product of the first two terms is the impedance conversion from  
 392 particle velocity to pressure at balloon altitude ( $z_b = 60 \text{ km}$ ). The third term is the  
 393 amplification factor for particle velocity from the ground to the balloon altitude. The  
 394 last term is the ground velocity of seismic waves in m/s at  $T_S$  period.

395 Using Equations 2, 3, 6, 5, 4 and 9 one can obtain the minimum number of events  
 396 per year required to measure at least 1 event of a given magnitude during the observa-  
 397 tion duration. The results are presented in Figure 5. This suggests a minimum amount  
 398 of events  $M_S = 6$  between 20 and 100 is required to detect at least one quake. Note  
 399 that at large magnitudes, the minimum number of events is limited to 4 per year, be-  
 400 cause the mission duration is 1/4 of a year.

#### 401 **2.4.5 Quake detection by Airglow measurements onboard orbiters**

402 Various studies pointed to the sensitivity of Venus' airglow emissions to pressure,  
 403 temperature and density variations induced by acoustic waves (Garcia et al., 2009; Steven-  
 404 son et al., 2015; López-Valverde et al., 2011). These studies mainly target two infrared

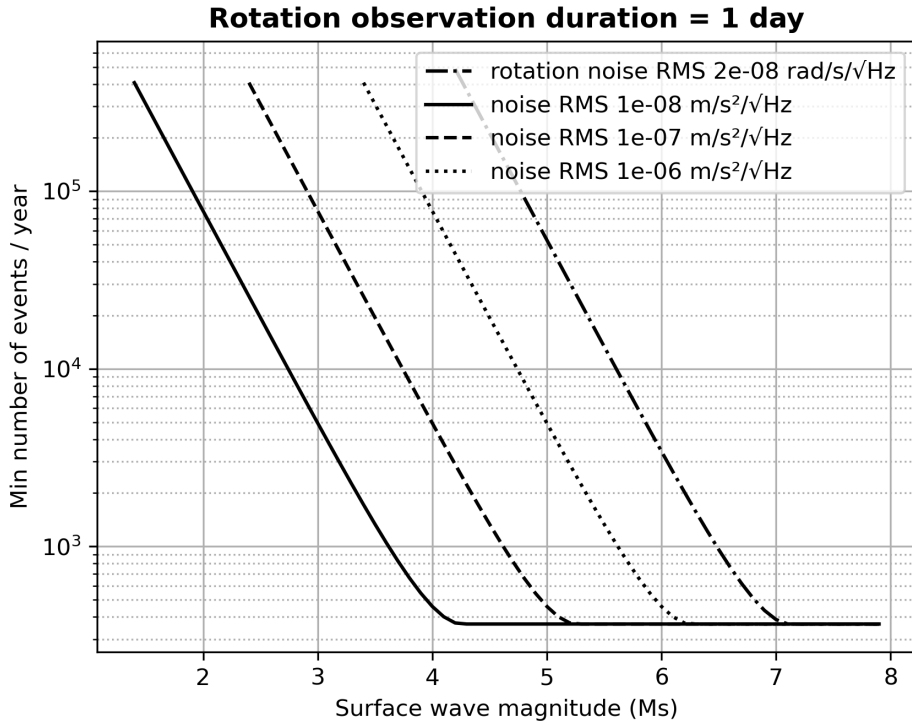


**Figure 4.** Minimum number of events per year as a function of surface wave magnitude required to measure at least one event of this magnitude during a ground rotation observation duration of 1 day. Results are provided for different noise levels:  $10^{-8}$  (plain line) and  $10^{-7}$  (dashed line),  $10^{-6}$  (dotted line)  $\text{m/s}^{-2}/\sqrt{\text{Hz}}$  at 20 s period. An estimate assuming that the noise floor is controlled by a typical self noise of a ground rotation instrument (BlueSeis-3A of iXblue company) is provided as dotted-dashed lines.

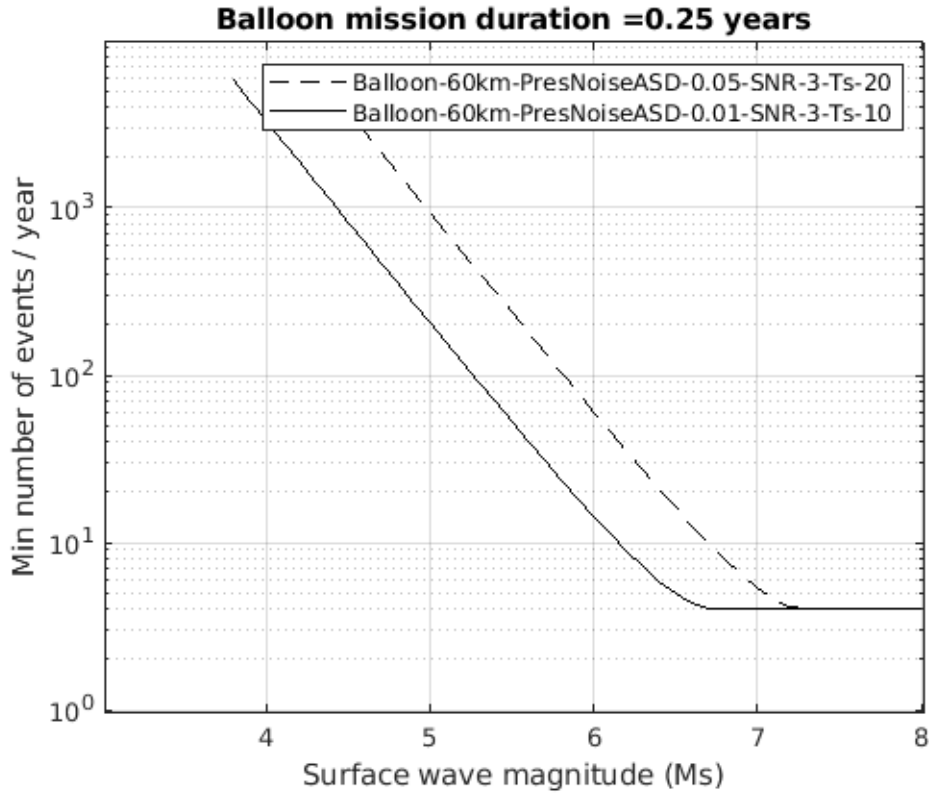


**Figure 5.** Minimum number of events per year as a function of surface wave magnitude required to measure at least one event of this magnitude during a balloon mission duration of 3 months. Results are provided at two different periods: 20 s (dashed line) and 10 s (plain line) because the noise level of pressure measurements varies significantly with frequency (from 0.05 to 0.01 Pa/ $\sqrt{\text{Hz}}$  going from 20 s to 10 s period).

405 airglows: nighttime airglow at 1.27  $\mu\text{m}$  and day time Non-Local Thermodynamical Equi-  
 406 librium emissions around 4.3  $\mu\text{m}$  (in fact two emission peaks at 4.28  $\mu\text{m}$  and 4.32  $\mu\text{m}$ ).  
 407 These studies paved the way to a dedicated mission concept studied at JPL/NASA (Sutin  
 408 et al., 2018). We will use this mission design, called VAMOS, in order to infer the de-  
 409 tection capabilities of airglow measurements in terms of the minimum number of events  
 410 per year required to detect at least one quake with this detection method. The concept  
 411 is targeting a continuous monitoring of the planet disk with a high sampling rate ( $> 1$   
 412 sample per second) camera orbiting on a circular equatorial orbit at a radius of 45,000  
 413 km with a period of approximately 29.2 hours.

414 As the measurement concept is different from a single point measurement by landed  
 415 seismometers or balloons, Equation 2 must be revised. First, because the airglow emis-  
 416 sions are localized only on a specific part of the planet, we must define this area as the  
 417 Observation Area ( $OA$ ) for a given airglow. For 1.27  $\mu\text{m}$  emission, this observation area  
 418 is centered on the equatorial point at 1:00 AM local time and covers an angular radius  
 419 of about  $60^\circ$  around that point, because it is in this region that we expect the largest  
 420 background emissions (Gérard et al., 2008). For simplicity, we assume that the center  
 421 point of this area is located at midnight local time. For 4.3  $\mu\text{m}$  emission, the observa-  
 422 tion area is centered on the equatorial point at 12:00 local time (midday) and covers an  
 423 angular radius of about  $70^\circ$  around that point. These emissions are proportional to solar  
 424 illumination, but polar regions and regions close to the terminator are conservatively  
 425 excluded because background emissions are low, and because more variability is expected  
 426 from gravity wave activity (Seiff & Kirk, 1991; Garcia et al., 2009; Gérard et al., 2014).

427 Then, another difference compared to single point measurements is that the ob-  
 428 servation area is not always visible in the camera images. To illustrate this, we use the  
 429 equatorial circular orbit of VAMOS to simplify the computations, although it still pro-  
 430 vides similar visibility statistics to other orbits at different ellipticity and inclination when  
 431 ensuring that the full disk is visible on more than 80% of the orbit period. In the full-  
 432 disk images of the planet, we conservatively consider that only points having an angu-  
 433 lar distance smaller than  $70^\circ$  for the center of the image (located at the equator) can be  
 434 used for observation because points close to the limb will have too much image distor-  
 435 tion. As a consequence, for a given local time position ( $\phi$  in longitude degrees) of the  
 436 center of the image (at the equator) relative to the center position of the visibility area  
 437 ( $\phi_0$ ) the visible observation area ( $VOA$ ) will be defined by the intersection of two spher-  
 438 ical caps (or solid angles) of size  $60^\circ$  (or  $70^\circ$ ) for the observation area and size  $70^\circ$  for  
 439 the imaging capability. Due to the rotation of the spacecraft around the planet, the size  
 440 of the visible observation area will vary as a function of the parameter  $\phi$ .

441 The function  $VOA(\Delta\phi)$ , with  $\Delta\phi = \phi - \phi_0$  is symmetric around zero. When this  
 442 area is zero (i.e., the observation area is not visible from the spacecraft) the correspond-  
 443 ing time period must be subtracted from the mission duration to define the observation  
 444 duration ( $T_m$  of Equation 2). When this area is non-zero, all the points in the area have  
 445 the capability of detecting seismic waves. Consequently, the surface  $S_m(M_S)$  of Equa-  
 446 tion 2 is much larger than for a single-point observation because it includes the whole  
 447 visible observation area  $VOA(\Delta\phi)$ , and extends it in both latitude and longitude direc-  
 448 tions by  $\Delta_m(M_S)$  degrees. When the surface of the visible observation area is non-zero,  
 449 the surface of the detection area is computed by the joint area of two spherical caps for  
 450 each surface wave magnitude ( $M_S$ ) and each longitude separation ( $\Delta\phi$ ) between the two  
 451 spherical caps (i.e., the visibility area and the image usable area). The average area over  
 452 all possible  $\Delta\phi$  values is then scaled to  $4\pi$  as in Equation 2. The observation duration  
 453 is reduced by the amount of time during which the visible observation area is zero.

454 Once these geometrical considerations have been taken into account, we still have  
 455 to compute the maximum distance at which a quake can be observed by a point in the  
 456 observation area  $\Delta_m(M_S)$ .

457 For the 1.27  $\mu\text{m}$  nighttime emissions, we need to convert the vertical particle ve-  
 458 locity in the acoustic wave into airglow emission and compare to the instrument noise.  
 459 The vertical particle velocity at the altitude of the maximum emission rate of the 1.27  $\mu\text{m}$   
 460 airglow ( $z_{IR1} = 100 \text{ km}$ ) is provided by:

$$A_v(z_{IR1}) = \sqrt{\frac{\rho(0)c(0)}{\rho(z_{IR1})c(z_{IR1})}} \left( \frac{10^{-6} A_d(0)}{2\pi T_S} \right) \quad (10)$$

461 where  $A_d(0)$  as function of surface wave magnitude is provided by inverting Equation 1.  
 462 The sensitivity of 1.27  $\mu\text{m}$  emissions is driven by the transport of the emitting molecules  
 463 under the vertical velocity  $A_v(z_{IR1})$  (Lognonné et al., 2016). The order of magnitude  
 464 of this sensitivity is about 3.0%/(m/s) at 20 s period and 6%/(m/s) at 50 s period at  
 465 100 km altitude (Sutin et al., 2018) In addition, the estimated noise level of an imag-  
 466 ing InfraRed (IR) camera targeting these emissions is about 0.5% of background emis-  
 467 sion level (Sutin et al., 2018).

468 For the 4.3  $\mu\text{m}$  daytime emission, we focus on the 4.28  $\mu\text{m}$  emission peak and as-  
 469 sume that the emission altitude is approximately 135 km and that these emissions present  
 470 a sensitivity of 1% per Kelvin variation of atmospheric temperature (López-Valverde et  
 471 al., 2011). In order to convert the vertical particle velocity  $A_v(z_{IR2})$  into temperature  
 472 perturbation (in Kelvin), we use the impedance at  $z_{IR2} = 135 \text{ km}$  altitude:

$$DP(z_{IR2}) = \rho(z_{IR2})c(z_{IR2})A_v(z_{IR2}) \quad (11)$$

$$= \rho(z_{IR2})c(z_{IR2}) \sqrt{\frac{\rho(0)c(0)}{\rho(z_{IR2})c(z_{IR2})}} \left( \frac{10^{-6} 2\pi A_d(0)}{T_S} \right) \quad (12)$$

473 which is similar to Equation 9 but at the altitude of the 4.28  $\mu\text{m}$  emission peak. Then,  
 474 we assume both the perfect gas law and the adiabatic nature of the acoustic wave per-  
 475 turbations in order to quantify the corresponding temperature changes through the fol-  
 476 lowing equation:

$$DT(z_{IR2}) = \frac{\gamma - 1}{\gamma} \frac{T(z_{IR2})}{P(z_{IR2})} DP(z_{IR2}), \quad (13)$$

477 where  $\gamma$  is the heat capacity ratio at altitude  $z_{IR2} = 135 \text{ km}$ , and  $T(z_{IR2})$  and  $P(z_{IR2})$   
 478 are the background temperature and pressure at this altitude, respectively. Finally, us-  
 479 ing the sensitivity of 1% per Kelvin of the 4.28  $\mu\text{m}$  emission, we obtain the expected sig-  
 480 nal in percentage of background emission (López-Valverde et al., 2011). Concerning the  
 481 instrument noise, we assume that the root-mean-square noise of the detector is about  
 482 0.125% of background emission (Sutin et al., 2018).

483 Gathering all these equations, we obtain the minimum number of events per year  
 484 for a mission duration of 2 years, and for the two infrared emissions. This result is shown  
 485 in Figure 6. The minimum surface magnitude that can be detected through these air-  
 486 glow emissions is between 4.5 and 5. However, we have a low variability of the minimum  
 487 number of events per year because of the large extent of the observation area.

#### 488 **2.4.6 Comparing the different seismic wave measurements concepts**

489 Figure 7 assembles the detection capabilities of all the different seismic wave mea-  
 490 surement concepts in the same figure, although the ground sensors in this figure are lim-  
 491 ited to seismometers, as the other ground measurement concepts are not yet technologi-  
 492 cally feasible. From this figure, it is clear that the airglow emissions are best designed  
 493 to detect quakes of surface wave magnitude larger than 5. In addition, the capability of

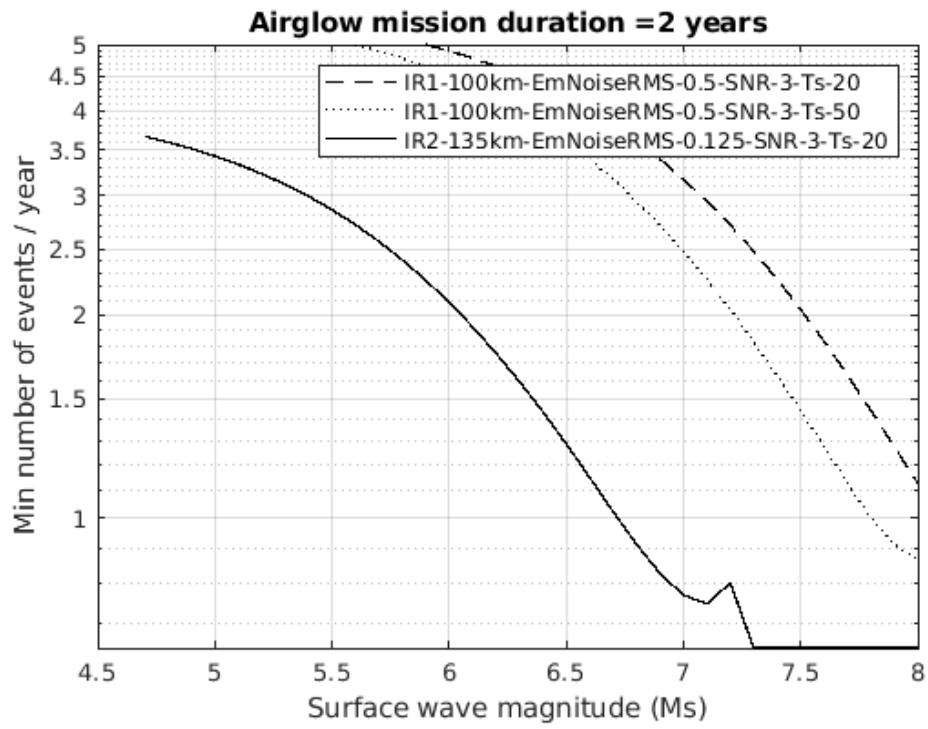


**Figure 6.** Minimum number of events per year as a function of surface wave magnitude required to measure at least one event of this magnitude during an airglow orbiter mission duration of 2 years. Results are provided for the two airglow emissions respectively at  $1.27 \mu\text{m}$  (dashed line at 20 s period, dotted line at 50 s period) and at  $4.28 \mu\text{m}$  (solid line).

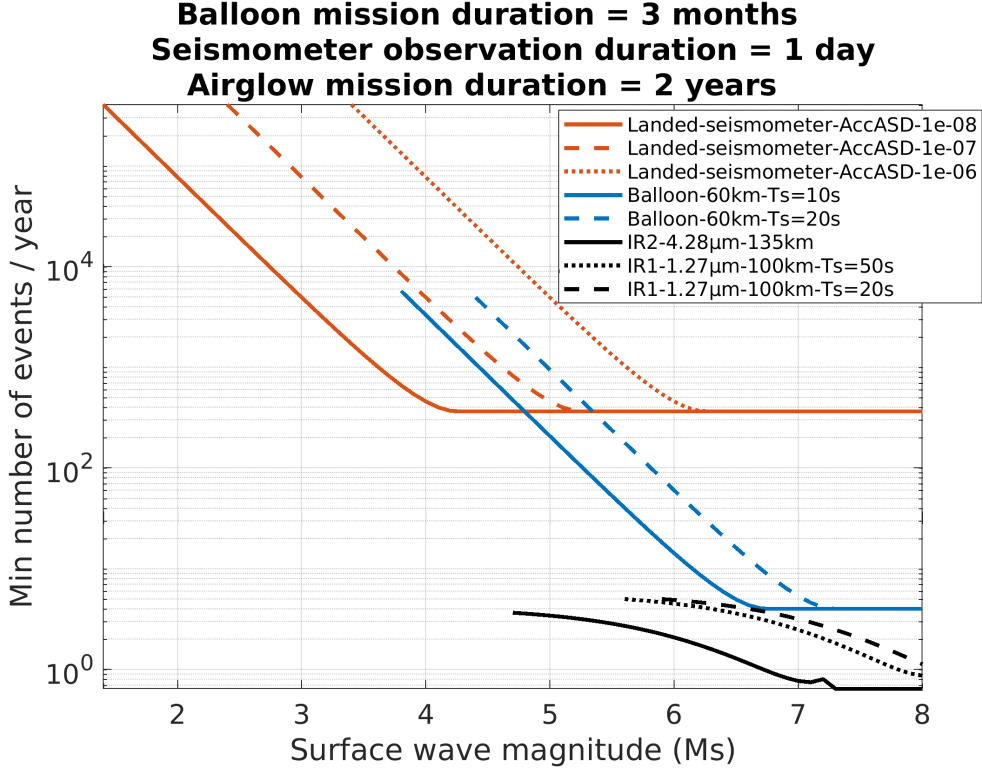


**Figure 7.** Minimum number of events per year as a function of surface wave magnitude required to measure at least one event of this magnitude for all the detection methods. Balloon estimates in blue, landed seismometers in brown, and airglow emissions in black.

494 such observations to track surface wave propagation on the images is opening more op-  
 495 portunities to image lateral variations in the crust and the lithosphere. However, due to  
 496 low-pass effects, induced by the vertical extent of airglow emission peaks and by the re-  
 497 sponse of airglow emissions to acoustic forcing, these observations are probably limited  
 498 to periods larger than 10 s (Lognonné et al., 2016; Sutin et al., 2018).

499 The balloon observations have a detection limit around 4.0–4.5 units of surface wave  
 500 magnitude and can detect all quakes with surface wave magnitude larger than 7. In ad-  
 501 dition, they can detect higher frequency signals, with a usable bandwidth mainly for pe-  
 502 riods between 0.5 s and 20 s. However, this observation mean suffers for its single point  
 503 measurement and from the short mission duration, estimated here to be 3 months.

504 Finally, for short duration deployment of a landed seismometer, the estimates present  
 505 a large variability due to the large uncertainties on the final noise level of such an instru-  
 506 ment. Assuming a noise level between  $10^{-7}$  and  $10^{-6}$   $\text{m/s}^2/\sqrt{\text{Hz}}$  at 20 s period, such  
 507 an instrument can detect all quakes of surface wave magnitude larger than 5 to 6. In ad-  
 508 dition, for small quakes close to the sensor, the bandwidth of such an instrument would  
 509 easily cover the 0.05–20 Hz. However, such a concept is strongly limited by the short ob-  
 510 servation duration, assumed here to be 1 day, such that it would allow us to investigate  
 511 only seismic events that are occurring more than 400 times per Earth year.

### 3 Comparing of detection capabilities with current seismicity estimates

Our estimates of detection capabilities are shown in figure 7 as a function of surface wave magnitude  $M_S$  which was defined following the IASPEI standard and corresponds to the definition of  $M_{S,20}$  by (Bormann et al., 2013). However, seismicity estimates are usually provided as a function of seismic moment magnitude  $M_W$  which is a better representation of the quake physics. In order to convert from  $M_S$  to  $M_W$ , we use the following relation defined by Bormann et al. (2013) for quake moment magnitudes smaller than 6.8 that are of our main interest:

$$M_W = 0.667 M_S + 2.18 \quad (14)$$

The error bar in this conversion is on the order of 0.3 magnitude unit, but even such large errors could in fact be smaller than the error we may have due to the unknown internal structure of Venus. Eventually, the moment magnitude is converted to the seismic moment  $M_0$  (in Nm) by the standard conversion formula  $M_W = \frac{2}{3}(\log_{10}(M_0) - 9.1)$ .

Once  $M_S$  has been converted into  $M_W$  or  $M_0$ , we can directly compare our detection limits of at least one quake with a signal-to-noise ratio larger than 3 over the mission duration with the Venus seismicity estimates by (Van Zelst et al., 2024). This comparison is presented in Figure 8.

The detection limits presented here should be taken with caution for two main reasons. First, the limitations presented in the next section induce an error bar on the order of one order of magnitude on these estimates. Secondly, we investigated mainly seismic signals around the 20 s period whereas the expected bandwidths of the different methods are different with an upper bound frequency of 10 Hz for ground sensors to 0.1 Hz for airglow observations.

Despite these limitations, a few interesting observations can be made in Figure 8. The ground-based sensors can be considered adequate for seismic wave detection if their noise level at 20 s period is below  $10^{-8} \text{ m/s}^2/\sqrt{\text{Hz}}$  and if they are deployed in an active seismic area that would allow us to detect quakes of magnitudes smaller than 4.0. The pressure sensors on balloon platforms allow for probing quake magnitudes in the 5.0 to 7.0 moment magnitude range and mainly for seismic signal frequencies in the 0.05 to 1 Hz range. Lastly, the airglow measurements have the lowest detection limits due to the low noise level and the long duration of the observations. In addition, the output movie of wave propagation would allow for determining the source location and investigating variations in seismic surface speeds over the planet that could be related to lateral heterogeneities in the shallow seismic wave structure of the crust. However, this measurement concept is limited to seismic moment magnitudes larger than 5.5 and to wave periods larger than 5 s.

### 4 Limitations

Our analysis operated under certain assumptions that leave room for future improvements and exploration.

First, the spatial dependence of seismicity estimates is not taken into account in our estimates of quake detectability, despite the likelihood that certain areas on Venus exhibit higher seismic activity compared to others. Even if this issue is not so critical for airglow measurements that will cover a large part of the planet surface, it is obvious that ground sensor deployments should target the most active regions in order to improve their detection capabilities. The balloon missions are also expected to cover more equatorial regions than polar regions due to deployment and mission duration constraints.

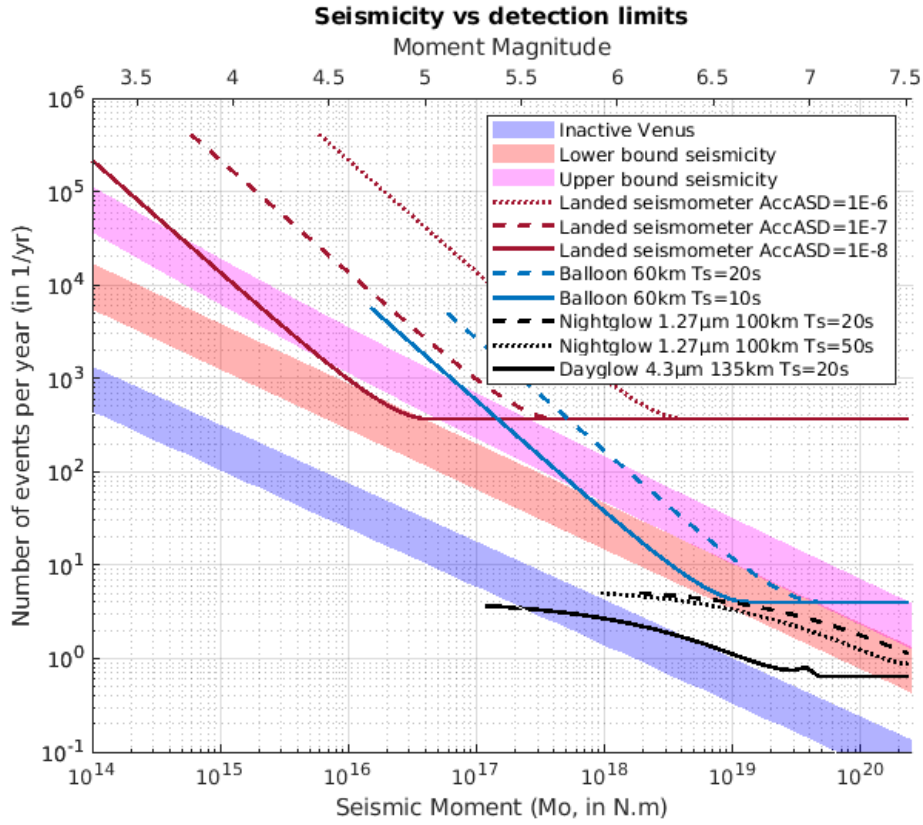


**Figure 8.** Minimum number of events per year as a function of seismic moment (in N·m) on the bottom and moment magnitude on top required to measure at least one event of this magnitude for all the detection methods (lines) compared to end-member Venus seismicity estimates (shaded areas) by Van Zelst et al. (2024): an inactive Venus (blue), lower bound active Venus (red) and upper bound active Venus (magenta). Balloon estimates are in dark blue, landed seismometers in brown, and airglow emissions in black.

557 A second important limitation is the uncertainty on the noise levels of each mea-  
 558 surement concept. Even though we consider reasonable assumptions on these numbers  
 559 and provided estimates for different noise levels, detailed noise models of these measure-  
 560 ment concepts are required to fully validate our analysis. Mimoun et al. (2017) provides  
 561 an example of a detailed noise model for a seismometer instrument. An inherent diffi-  
 562 culty to the noise model exercise is that the mission parameters (lander size, instrument  
 563 performance parameters, etc.) must be known in order for the analysis to be valid.

564 Lastly, the method used to relate ground movements to quake magnitude and the  
 565 frequencies considered here (periods between 10 and 50 seconds) are mainly relevant for  
 566 quake moment magnitudes between 4.0 and 6.8 (Bormann et al., 2013). For quake mo-  
 567 ment magnitudes smaller than 4.0, other methods and frequency ranges should be con-  
 568 sidered.

## 569 5 Conclusion

570 Our study provides a first estimate of the detection capabilities of long period seis-  
 571 mic surface waves on Venus by various measurement concepts: ground sensors includ-  
 572 ing seismometers, DAS, and rotation sensors; infrasound sensors on balloons; and air-  
 573 glow imagers onboard orbiters. We also compare these estimates with recent predictions  
 574 of Venus seismicity. The airglow measurement concept appears to be most relevant in  
 575 light of the current estimates of seismicity, but it is limited to moment magnitudes larger  
 576 than 5.5 and wave periods larger than 5 s. We find that a minimum measurement du-  
 577 ration of two years ensures a good probability to detect large magnitude quakes. Infra-  
 578 sound sensors onboard balloons must ensure an overall noise level below  $10^{-2}$  Pa/ $\sqrt{\text{Hz}}$   
 579 at 10 s period and a measurement duration in the order of a month to obtain a good prob-  
 580 ability of quake detection. The ground sensors are strongly limited by their measurement  
 581 duration but also by their noise, mainly due to instrument self-noise for potential ground  
 582 rotation sensors, and noise induced by the installation or environment for seismometers  
 583 and potential DAS fiber measurements that would be effective only with an overall ac-  
 584 celeration noise level at 20 s period below  $10^{-8}$  m/s<sup>2</sup>/ $\sqrt{\text{Hz}}$ . Uncertainties ranging up to  
 585 one order of magnitude impact these detection limit estimates due to limitations that  
 586 could be improved in various directions by future studies. Potential directions of improve-  
 587 ments would be to take into account the geographical distribution of quakes, a full mod-  
 588 eling of the amplitude of seismic and infrasound waves, detailed noise models of the mea-  
 589 surement concepts... Rather than definitively concluding on one measurement concept,  
 590 our study allows us to enhance the advantages and limitations of each measurement con-  
 591 cept and can drive requirements on future mission concepts that would deploy such mea-  
 592 surement tools.

593 Despite the recent selection of various space missions to Venus, none of these will  
 594 target the detection and characterization of seismic waves to investigate Venus' inter-  
 595 nal structure in better detail. The most realistic programmatic scenario for the imple-  
 596 mentation of any of the measurement concepts described in this study in the next decade  
 597 is therefore the deployment of such concepts by a small satellite as a piggyback payload  
 598 on one of these missions.

## 599 Open Research

600 All the codes and input data used to create the figures in this article are available  
 601 at the following zenodo repository <https://zenodo.org/records/10943310> (DOI: 10.5281/zen-  
 602 odo.10943310).

## Author contributions

Conceptualization: RFG, IvZ, KTS  
 Data curation:  
 Formal Analysis: RFG, SK, TK  
 Funding acquisition: IvZ  
 Investigation: RFG, SPN, QB  
 Methodology: RFG, SS  
 Project administration: IvZ  
 Resources: ML  
 Software: RFG, TK, SK, CMS  
 Supervision:  
 Validation: SPN, ML, CMS, QB  
 Visualization: RFG, SK, CMS, SPN  
 Writing – original draft: RFG, SK, SPN, QB, ML, AH, TK, KTS, CMS  
 Writing – review & editing: AG, SPN, IvZ, BDT, QB, ML, JM, ACP, AH, SS, PL, MP, KTS

## Acknowledgements

This research was supported by the International Space Science Institute (ISSI) in Bern, Switzerland through ISSI International Team project #566: “Seismicity on Venus: Prediction & Detection”, led by Iris van Zelst. RFG acknowledges funding by CNES through APR project “VenusGeox”. IvZ, JM, and ACP acknowledge the financial support and endorsement from the DLR Management Board Young Research Group Leader Program and the Executive Board Member for Space Research and Technology. IvZ also gratefully acknowledges the support by the Deutsche Forschungsgemeinschaft (DFG, German Research Foundation), Project-ID 263649064 – TRR 170. SPN, CMS, and QB acknowledge support from the Research Council of Norway basic research program FRIPRO through the project “Airborne Inversion of Rayleigh waves” under Contract 335903. ML acknowledges funding from the European Union’s Horizon Europe research and innovation program under the Marie Skłodowska-Curie grant agreement 101110489/MuSICA-V. AG acknowledges support by the Swiss National Science Foundation Postdoc Mobility Grant P500PN\_21729 and by the Jet Propulsion Laboratory, California Institute of Technology, under contract (80NM0018D0004) with the National Aeronautics and Space Administration. A.H. is funded by the UK Space Agency under grant numbers ST/W002523/1, ST/W002949/1 and ST/Y005597/1.

## References

- Avduevskii, V. S., Vishnevetskii, S. L., Golov, I. A., Karpeiskii, I. I., Lavrov, A. D., Likhushin, V. I., . . . Pronina, N. N. (1977). Measurement of wind velocity on the surface of Venus during the operation of stations Venera 9 and Venera 10. *Cosmic Research*, *14*(5), 710–713.
- Banfield, D., Spiga, A., Newman, C., Forget, F., Lemmon, M., Lorenz, R., . . . Banerdt, W. B. (2020, February). The atmosphere of Mars as observed by InSight. *Nature Geoscience*, *13*(3), 190-198. doi: 10.1038/s41561-020-0534-0
- Bass, H. E., & Chambers, J. P. (2001, May). Absorption of sound in the Martian atmosphere. *Acoustical Society of America Journal*, *109*(5), 2371–2371. doi: 10.1121/1.4744345
- Bernauer, F., Behnen, K., Wassermann, J., Egdorf, S., Igel, H., Donner, S., . . . Brokesova, J. (2021, January). Rotation, strain, and translation sensors performance tests with active seismic sources. *Sensors*, *21*(1), 264. doi: 10.3390/s21010264
- Bernauer, F., Garcia, R. F., Murdoch, N., Dehant, V., Sollberger, D., Schmelzbach,

- 653 C., . . . de Raucourt, S. (2020, December). Exploring planets and asteroids  
654 with 6DoF sensors: Utopia and realism. *Earth, Planets and Space*, 72(1), 191.  
655 doi: 10.1186/s40623-020-01333-9
- 656 Bernauer, F., Wassermann, J., & Igel, H. (2020, September). Dynamic tilt correc-  
657 tion using direct rotational motion measurements. *Seismological Research Let-  
658 ters*, 91(5), 2872–2880. doi: 10.1785/0220200132
- 659 Bormann, P. (2002). *New manual of seismological observatory practice*. Geo-  
660 Forschungszentrum. doi: 10.2312/GFZ.NMSOP-2\_ch4
- 661 Bormann, P., & Dewey, J. W. (2012). The new IASPEI standards for determining  
662 magnitudes from digital data and their relation to classical magnitudes..
- 663 Bormann, P., Wendt, S., & DiGiacomo, D. (2013). Seismic sources and source pa-  
664 rameters. In *New manual of seismological observatory practice 2 (nmsop2)* (pp.  
665 1–259). Deutsches GeoForschungsZentrum GFZ. doi: 10.2312/GFZ.NMSOP-2  
666 \_ch3
- 667 Brissaud, Q., Krishnamoorthy, S., Jackson, J. M., Bowman, D. C., Komjathy, A.,  
668 Cutts, J. A., . . . Izraelevitz, G. J., J. S. andWalsh (2021). The first detec-  
669 tion of an earthquake from a balloon using its acoustic signature. *Geophysical  
670 Research Letters*, 48(12). doi: 10.1029/2021gl093013
- 671 Byrne, P. K., Ghail, R. C., Şengör, A. M. C., James, P. B., Klimczak, C., &  
672 Solomon, S. C. (2021). A globally fragmented and mobile lithosphere on  
673 venus. *Proceedings of the National Academy of Sciences*, 118(26). doi:  
674 10.1073/pnas.2025919118
- 675 Carrasco, S., Knapmeyer-Endrun, B., Margerin, L., Xu, Z., Joshi, R., Schimmel,  
676 M., . . . Banerdt, W. B. (2023, August). Constraints for the Martian crustal  
677 structure from Rayleigh waves ellipticity of large seismic events. *Geophysical  
678 Research Letters*, 50(16), e2023GL104816. doi: 10.1029/2023GL104816
- 679 Chan, H. M., Parker, A. R., Piazza, A., & Richards, W. L. (2015). Fiber-optic  
680 sensing system: overview, development and deployment in flight at nasa. In  
681 *2015 ieee avionics and vehicle fiber-optics and photonics conference (avfop)*  
682 (pp. 71–73).
- 683 Chen, L., Neudeck, P. G., Meredith, R. D., Lukco, D., Spry, D. J., Nakley, L. M., . . .  
684 Hunter, G. W. (2019). Sixty earth-day test of a prototype Pt/HTCC alumina  
685 package in a simulated Venus environment. *Journal of microelectronics and  
686 electronic packaging*, 16(2), 78–83. doi: 10.4071/imaps.873073
- 687 Cheng, F., Chi, B., Lindsey, N. J., Dawe, T. C., & Ajo-Franklin, J. B. (2021). Uti-  
688 lizing distributed acoustic sensing and ocean bottom fiber optic cables for  
689 submarine structural characterization. *Scientific reports*, 11(1), 5613. doi:  
690 10.1038/s41598-021-84845-y
- 691 Daley, T., Miller, D., Dodds, K., Cook, P., & Freifeld, B. (2016). Field testing of  
692 modular borehole monitoring with simultaneous distributed acoustic sensing  
693 and geophone vertical seismic profiles at Citronelle, Alabama. *Geophysical  
694 Prospecting*, 64(5), 1318–1334. doi: 10.1111/1365-2478.12324
- 695 Drilleau, M., Samuel, H., Garcia, R. F., Rivoldini, A., Perrin, C., Michaut, C., . . .  
696 Banerdt, W. B. (2022, September). Marsquake locations and 1-D seismic  
697 models for Mars from InSight data. *Journal of Geophysical Research (Planets)*,  
698 127(9), e07067. doi: 10.1029/2021JE007067
- 699 Dumoulin, C., Tobie, G., Verhoeven, O., Rosenblatt, P., & Rambaux, N. (2017,  
700 June). Tidal constraints on the interior of Venus. *Journal of Geophysical  
701 Research (Planets)*, 122(6), 1338–1352. doi: 10.1002/2016JE005249
- 702 Durán, C., Khan, A., Ceylan, S., Charalambous, C., Kim, D., Drilleau, M., . . .  
703 Giardini, D. (2022, November). Observation of a Core-Diffracted P-Wave  
704 From a Farside Impact With Implications for the Lower-Mantle Struc-  
705 ture of Mars. *Geophysical Research Letters*, 49(21), e2022GL100887. doi:  
706 10.1029/2022GL100887
- 707 Durán, C., Khan, A., Ceylan, S., Zenhäusern, G., Stähler, S., Clinton, J. F., &

- Giardini, D. (2022, April). Seismology on Mars: An analysis of direct, reflected, and converted seismic body waves with implications for interior structure. *Physics of the Earth and Planetary Interiors*, *325*, 106851. doi: 10.1016/j.pepi.2022.106851
- Garcia, R. F., Brissaud, Q., Rolland, L., Martin, R., Komatitsch, D., Spiga, A., ... Banerdt, B. (2017). Finite-difference modeling of acoustic and gravity wave propagation in Mars atmosphere: application to infrasounds emitted by meteor impacts. *Space Science Reviews*, *211*, 547–570. doi: 10.1007/s11214-016-0324-6
- Garcia, R. F., Drossart, P., Piccioni, G., López-Valverde, M., & Occhipinti, G. (2009, March). Gravity waves in the upper atmosphere of Venus revealed by CO<sub>2</sub> nonlocal thermodynamic equilibrium emissions. *Journal of Geophysical Research (Planets)*, *114*, E00B32. doi: 10.1029/2008JE003073
- Garcia, R. F., Klotz, A., Hertzog, A., Martin, R., G erier, S., Kassarian, E., ... Mismoun, D. (2022, August). Infrasound from large earthquakes recorded on a network of balloons in the stratosphere. *Geophysical Research Letters*, *49*(15). doi: 10.1029/2022gl098844
- Garcia, R. F., Lognonn e, P. H., & Bonnin, X. (2005). Detecting atmospheric perturbations produced by Venus quakes. *Geophysical Research Letters*, *32*(16), 1–4. doi: 10.1029/2005GL023558
- Garvin, J. B., Getty, S. A., Arney, G. N., Johnson, N. M., Kohler, E., Schwer, K. O., ... Zolotov, M. (2022). Revealing the mysteries of venus: The davinci mission. *The Planetary Science Journal*, *3*(5), 117. Retrieved from <http://dx.doi.org/10.3847/PSJ/ac63c2> doi: 10.3847/psj/ac63c2
- G erard, J. C., Saglam, A., Piccioni, G., Drossart, P., Cox, C., Erard, S., ... S anchez-Lavega, A. (2008, January). Distribution of the O<sub>2</sub> infrared night-glow observed with VIRTIS on board Venus Express. *Geophysical Research Letters*, *35*(2), L02207. doi: 10.1029/2007GL032021
- G erard, J. C., Soret, L., Piccioni, G., & Drossart, P. (2014). Latitudinal structure of the Venus O<sub>2</sub> infrared airglow: A signature of small-scale dynamical processes in the upper atmosphere. *Icarus*, *236*, 92–103. doi: 10.1016/j.icarus.2014.03.028
- Gilli, G., Lebonnois, S., Gonz alez-Galindo, F., L opez-Valverde, M. A., Stolzenbach, A., Lef evre, F., ... Lott, F. (2017). Thermal structure of the upper atmosphere of Venus simulated by a ground-to-thermosphere GCM. *Icarus*, *281*, 55–72. doi: 10.1016/j.icarus.2016.09.016
- Gilli, G., Navarro, T., Lebonnois, S., Quirino, D., Silva, V., Stolzenbach, A., ... Schubert, G. (2021). Venus upper atmosphere revealed by a GCM: II. Model validation with temperature and density measurements. *Icarus*, *366*, 114432. doi: 10.1016/j.icarus.2021.114432
- Glass, D. E., Jones, J.-P., Shevade, A. V., Bhakta, D., Raub, E., Sim, R., & Bugga, R. V. (2020). High temperature primary battery for Venus surface missions. *Journal of Power Sources*, *449*, 227492. doi: 10.1016/j.jpowsour.2019.227492
- Gudkova, T. V., & Zharkov, V. N. (2020, March). Models of the internal structure of the Earth-like Venus. *Solar System Research*, *54*(1), 20–27. doi: 10.1134/S0038094620010049
- G ulcher, A. J. P., Gerya, T. V., Mont esi, L. G. J., & Munch, J. (2020). Corona structures driven by plume–lithosphere interactions and evidence for ongoing plume activity on Venus. *Nature Geoscience*, *13*(8), 547–554. doi: 10.1038/s41561-020-0606-1
- Heracle. (2023, 11). *Step Index Multimode Fibers Metal Coated Series: Gold*. Retrieved from <https://www.heracle.de/products/step-index-multimode-fibers-metal-coated-series-gold/?lang=en>
- Herrick, R., & Hensley, S. (2023). Surface changes observed on a Venusian volcano during the Magellan mission. *Science*, *379*(6638), 1205–1208. doi: 10.1126/

- 763 science.abm7735
- 764 Hudson, T. S., Baird, A. F., Kendall, J.-M., Kufner, S.-K., Brisbourne, A. M.,  
765 Smith, A. M., . . . Clarke, A. (2021). Distributed acoustic sensing (DAS)  
766 for natural microseismicity studies: A case study from Antarctica. *Journal of*  
767 *Geophysical Research: Solid Earth*, *126*(7), e2020JB021493.
- 768 Hunter, G., Kremic, T., & Neudeck, P. G. (2021). High temperature electron-  
769 ics for Venus surface applications: A summary of recent technical advances.  
770 In *Bulletin of the american astronomical society* (Vol. 53, p. 399). doi:  
771 10.3847/25c2cfcb.e3883e19
- 772 Jacobsen, W., Soufiane, A., & D’Urso, J. (2018). 500° c-rated optical fibers for high  
773 temperature applications. In *80th eage conference and exhibition 2018* (Vol.  
774 2018, pp. 1–5).
- 775 Jousset, P., Currenti, G., Schwarz, B., Chalari, A., Tilmann, F., Reinsch, T.,  
776 . . . Krawczyk, C. M. (2022). Fibre optic distributed acoustic sensing  
777 of volcanic events. *Nature communications*, *13*(1), 1753. doi: 10.1038/  
778 s41467-022-29184-w
- 779 Kerzhanovich, V. V., & Marov, M. I. (1983). The atmospheric dynamics of Venus  
780 according to Doppler measurements by the Venera entry probes. In *Venus* (pp.  
781 766–778). The University of Arizona Press.
- 782 Kim, D., Banerdt, W. B., Ceylan, S., Giardini, D., Lekić, V., Lognonné, P., . . . Pan-  
783 ning, M. P. (2022, October). Surface waves and crustal structure on Mars.  
784 *Science*, *378*(6618), 417–421. doi: 10.1126/science.abq7157
- 785 Klaasen, S., Paitz, P., Lindner, N., Dettmer, J., & Fichtner, A. (2021). Dis-  
786 tributed acoustic sensing in volcano-glacial environments—Mount Meager,  
787 British Columbia. *Journal of Geophysical Research: Solid Earth*, *126*(11),  
788 e2021JB022358. doi: 10.1029/2021JB022358
- 789 Klaasen, S., Thrastarson, S., Çubuk-Sabuncu, Y., Jónsdóttir, K., Gebraad, L.,  
790 Paitz, P., & Fichtner, A. (2023). Subglacial volcano monitoring with  
791 fibre-optic sensing: Grímsvötn, Iceland. *Volcanica*, *6*(2), 301–311. doi:  
792 10.30909/vol.06.02.301311
- 793 Kremic, T., Ghail, R., Gilmore, M., Hunter, G., Kiefer, W., Limaye, S., . . . Wilson,  
794 C. (2020). Long-duration Venus lander for seismic and atmospheric science.  
795 *Planetary Space Science*, *190*, 104961. doi: 10.1016/j.pss.2020.104961
- 796 Krishnamoorthy, S., & Bowman, D. C. (2023, January). A “Floatilla” of Airborne  
797 Seismometers for Venus. *Geophysical Research Letters*, *50*(2), e2022GL100978.  
798 doi: 10.1029/2022GL100978
- 799 Ksanfomaliti, L. V., Goroshkova, N. V., & Khondyrev, V. K. (1983). Wind velocity  
800 on the Venus surface from acoustic measurements. *Kosmicheskie Issledovaniia*,  
801 *21*, 218–224.
- 802 Ksanfomaliti, L. V., Zubkova, V. M., Morozov, N. A., & Petrova, N. A. (1982). Mi-  
803 croseisms at the Venera 13 and Venera 14 landing sites. *Pisma v Astronomich-*  
804 *eskii Zhurnal*, *8*, 444–447.
- 805 Lebonnois, S., Schubert, G., Forget, F., & Spiga, A. (2018, November). Planetary  
806 boundary layer and slope winds on Venus. *Icarus*, *314*, 149–158. doi: 10.1016/  
807 j.icarus.2018.06.006
- 808 Lefèvre, M. (2022). Venus boundary layer dynamics: Eolian transport and convective  
809 vortex. *Icarus*, *387*, 115167. doi: 10.1016/j.icarus.2022.115167
- 810 Lefèvre, M., Spiga, A., Lebonnois, S., & Forget, F. (2024). Control of the surface  
811 temperature on Venus by slope winds. *To be Submitted*.
- 812 Lindsey, N. J., & Martin, E. R. (2021). Fiber-optic seismology. *Annual Review*  
813 *of Earth and Planetary Sciences*, *49*, 309–336. doi: 10.1146/annurev-earth  
814 -072420-065213
- 815 Lior, I., Sladen, A., Rivet, D., Ampuero, J.-P., Hello, Y., Becerril, C., . . . others  
816 (2021). On the detection capabilities of underwater distributed acoustic sens-  
817 ing. *Journal of Geophysical Research: Solid Earth*, *126*(3), e2020JB020925.

- 818 Lognonné, P., Banerdt, W. B., Clinton, J., Garcia, R. F., Giardini, D., Knapmeyer-  
819 Endrun, B., . . . Pike, W. T. (2023, May). Mars seismology. *Annual*  
820 *Review of Earth and Planetary Sciences*, *51*, 643–670. doi: 10.1146/  
821 annurev-earth-031621-073318
- 822 Lognonné, P., Banerdt, W. B., Giardini, D., Pike, W. T., Christensen, U., Laudet,  
823 P., . . . Wookey, J. (2019, January). SEIS: Insight’s seismic experiment  
824 for internal structure of Mars. *Space Science Reviews*, *215*(1), 12. doi:  
825 10.1007/s11214-018-0574-6
- 826 Lognonné, P., Karakostas, F., Rolland, L., & Nishikawa, Y. (2016, August). Mod-  
827 eling of atmospheric-coupled Rayleigh waves on planets with atmosphere:  
828 From Earth observation to Mars and Venus perspectives. *The Journal of the*  
829 *Acoustical Society of America*, *140*(2), 1447–1468. doi: 10.1121/1.4960788
- 830 López-Valverde, M. A., López-Puertas, M., Funke, B., Gilli, G., Garcia-Comas, M.,  
831 Drossart, P., . . . Formisano, V. (2011, August). Modeling the atmospheric  
832 limb emission of CO<sub>2</sub> at 4.3 μm in the terrestrial planets. *Planetary and Space*  
833 *Science*, *59*(10), 988–998. doi: 10.1016/j.pss.2010.02.001
- 834 Lorenz, R. D. (2012). Planetary seismology—expectations for lander and wind noise  
835 with application to Venus. *Planetary and Space Science*, *62*(1), 86–96. doi: 10  
836 .1016/j.pss.2011.12.010
- 837 Lorenz, R. D. (2016). Surface winds on Venus: Probability distribution from in-situ  
838 measurements. *Icarus*, *264*, 311–315. doi: 10.1016/j.icarus.2015.09.036
- 839 Lorenz, R. D., & Panning, M. P. (2018). Empirical recurrence rates for ground mo-  
840 tion signals on planetary surfaces. *Icarus*, *303*, 273–279. doi: 10.1016/j.icarus  
841 .2017.10.008
- 842 Makela, J. J., Lognonné, P., Hébert, H., Gehrels, T., Rolland, L., Allgeyer, S., . . .  
843 Lamouroux, J. (2011, July). Imaging and modeling the ionospheric air-  
844 glow response over Hawaii to the tsunami generated by the Tohoku earth-  
845 quake of 11 March 2011. *Geophysical Research Letters*, *38*(13), L00G02. doi:  
846 10.1029/2011GL047860
- 847 Margot, J.-L., Campbell, D. B., Giorgini, J. D., Jao, J. S., Snedeker, L. G., Ghigo,  
848 F. D., & Bonsall, A. (2021). Spin state and moment of inertia of venus. *Nature*  
849 *Astronomy*, *5*(7), 676–683. Retrieved from [http://dx.doi.org/10.1038/  
850 s41550-021-01339-7](http://dx.doi.org/10.1038/s41550-021-01339-7) doi: 10.1038/s41550-021-01339-7
- 851 Martinez, A., Lebonnois, S., Millour, E., Pierron, T., Moisan, E., Gilli, G., &  
852 Lefèvre, F. (2023). Exploring the variability of the venusian thermosphere with  
853 the IPSL Venus GCM. *Icarus*, *389*, 115272. doi: 10.1016/j.icarus.2022.115272
- 854 Mimoun, D., Murdoch, N., Lognonné, P., Hurst, K., Pike, W. T., Hurley, J., . . .  
855 Banerdt, W. B. (2017, October). The noise model of the SEIS seismometer of  
856 the InSight mission to Mars. *Space Science Reviews*, *211*(1–4), 383–428. doi:  
857 10.1007/s11214-017-0409-x
- 858 Moroz, V. I. (1983). Summary of preliminary results of the Venera 13 and Venera 14  
859 missions. In *Venus* (pp. 45–68). The University of Arizona Press.
- 860 Nachman, A. I., Smith III, J. F., & Waag, R. C. (1990). An equation for acous-  
861 tic propagation in inhomogeneous media with relaxation losses. *The Journal of*  
862 *the Acoustical Society of America*, *88*(3), 1584–1595. doi: 10.1121/1.400317
- 863 Näsholm, S. P., Iranpour, K., Wuestefeld, A., Dando, B. D., Baird, A. F., & Oye, V.  
864 (2022). Array signal processing on distributed acoustic sensing data: Direc-  
865 tivity effects in slowness space. *Journal of Geophysical Research: Solid Earth*,  
866 *127*(2), e2021JB023587. doi: 10.1029/2021JB023587
- 867 Neudeck, P. G., Spry, D. J., Krasowski, M. J., Prokop, N. F., Beheim, G. M., Chen,  
868 L.-Y., & Chang, C. W. (2018). Year-long 500° C operational demonstration  
869 of up-scaled 4H-SiC JFET integrated circuits. *Journal of Microelectronics and*  
870 *Electronic Packaging*, *15*(4), 163–170.
- 871 Noe, S., Yuan, S., Montagner, J. P., & Igel, H. (2022, May). Anisotropic elastic  
872 parameter estimation from multicomponent ground-motion observations: a

- 873 theoretical study. *Geophysical Journal International*, 229(2), 1462–1473. doi:  
874 10.1093/gji/ggac006
- 875 Occhipinti, G., Coisson, P., Makela, J. J., Allgeyer, S., Kherani, A., Hebert, H., &  
876 Lognonné, P. (2011, July). Three-dimensional numerical modeling of tsunami-  
877 related internal gravity waves in the Hawaiian atmosphere. *Earth, Planets and*  
878 *Space*, 63(7), 847–851. doi: 10.5047/eps.2011.06.051
- 879 Parker, A. R., Chan, H. M., Lopez-Zepeda, J., & Schallhorn, P. A. (2024). Design,  
880 fabrication, testing and validation of a ruggedized fiber optics sensing system  
881 (foss) for launch application. In *Aiaa scitech 2024 forum* (p. 2268).
- 882 Petculescu, A. (2016). Acoustic properties in the low and middle atmospheres of  
883 mars and venus. *The Journal of the Acoustical Society of America*, 140(2),  
884 1439–1446. doi: <https://doi.org/10.1121/1.4960784>
- 885 Peterson, J. (1993). *Observation and modeling of background seismic noise*. U.S.  
886 Geol. Surv. Open-File Rept. 92-322. Albuquerque.
- 887 Reinsch, T., & Hennings, J. (2010). Temperature-dependent characterization of  
888 optical fibres for distributed temperature sensing in hot geothermal wells. *Mea-*  
889 *surement Science and Technology*, 21(9), 094022.
- 890 Samuel, H., Drilleau, M., Rivoldini, A., Xu, Z., Huang, Q., Garcia, R. F., ...  
891 Banerdt, W. B. (2023, October). Geophysical evidence for an enriched  
892 molten silicate layer above Mars’s core. *Nature*, 622(7984), 712–717. doi:  
893 10.1038/s41586-023-06601-8
- 894 Schmelzbach, C., Donner, S., Igel, H., Sollberger, D., Taufiqurrahman, T., Bernauer,  
895 F., ... Robertsson, J. (2018, May). Advances in 6C seismology: Appli-  
896 cations of combined translational and rotational motion measurements in  
897 global and exploration seismology. *Geophysics*, 83(3), WC53–WC69. doi:  
898 10.1190/geo2017-0492.1
- 899 Seiff, A., & Kirk, D. B. (1991). Waves in Venus’ middle and upper atmosphere; Im-  
900 plication of Pioneer Venus probe data above the clouds. *Journal of Geophysical*  
901 *Research*, 96(A7), 11021–11032. doi: 10.1029/91JA01101
- 902 Smrekar, S., Hensley, S., Nybakken, R., Wallace, M., Perkovic-Martin, D., You, T.-  
903 H., ... Mazarico, E. (2022). VERITAS (Venus Emissivity, Radio Science,  
904 InSAR, Topography, and Spectroscopy): A discovery mission. In *2022 ieee*  
905 *aerospace conference (aero)*. IEEE. Retrieved from [http://dx.doi.org/](http://dx.doi.org/10.1109/aero53065.2022.9843269)  
906 [10.1109/aero53065.2022.9843269](http://dx.doi.org/10.1109/aero53065.2022.9843269) doi: 10.1109/aero53065.2022.9843269
- 907 Smrekar, S. E., Ostberg, C., & O’Rourke, J. G. (2023). Earth-like lithospheric thick-  
908 ness and heat flow on Venus consistent with active rifting. *Nature Geoscience*,  
909 16(1), 13–18. doi: 10.1038/s41561-022-01068-0
- 910 Smrekar, S. E., Stofan, E. R., Mueller, N., Treiman, A., Elkins-Tanton, L., Helbert,  
911 J., ... Drossart, P. (2010). Recent hotspot volcanism on Venus from VIRTIS  
912 emissivity data. *Science*, 328(5978), 605–608. doi: 10.1126/science.1186785
- 913 Sollberger, D., Bradley, N., Edme, P., & Robertsson, J. O. A. (2023, July). Efficient  
914 wave type fingerprinting and filtering by six-component polarization analysis.  
915 *Geophysical Journal International*, 234(1), 25–39. doi: 10.1093/gji/ggad071
- 916 Stähler, S. C., Khan, A., Banerdt, W. B., Lognonné, P., Giardini, D., Ceylan, S., ...  
917 Smrekar, S. E. (2021, July). Seismic detection of the martian core. *Science*,  
918 373(6553), 443–448. doi: 10.1126/science.abi7730
- 919 Stevenson, D., Cutts, J., MimounDavid, Arrowsmith, S., Banerdt, B., Blom, P., ...  
920 Tsai, V. (2015, April). *Probing the interior structure of Venus* (Tech. Rep.).  
921 Keck Institute for Space Studies: Venus Seismology Study Team.
- 922 Stolov, A., & OFS. (2019, 1). *Testing Optical Fiber: Undersea and Downhole Ap-*  
923 *plications*. Retrieved from [https://www.photonics.com/Articles/Testing](https://www.photonics.com/Articles/Testing-Optical-Fiber-Undersea-and-Downhole/p5/v170/i1115/a64288)  
924 [\\_Optical-Fiber-Undersea-and-Downhole/p5/v170/i1115/a64288](https://www.photonics.com/Articles/Testing-Optical-Fiber-Undersea-and-Downhole/p5/v170/i1115/a64288)
- 925 Surkov, Y. A., Barsukov, V., Moskalyeva, L., Kharyukova, V., & Kemurdzhian, A.  
926 (1984). New data on the composition, structure, and properties of Venus rock  
927 obtained by Venera 13 and Venera 14. *Journal of Geophysical Research: Solid*

- 928 *Earth*, 89(S02), B393–B402.
- 929 Sutin, B. M., Cutts, J., Didion, A. M., Drilleau, M., Grawe, M., Helbert, J., ...  
 930 Wallace, M. (2018, July). VAMOS: a SmallSat mission concept for re-  
 931 mote sensing of Venusian seismic activity from orbit. In M. Lystrup,  
 932 H. A. MacEwen, G. G. Fazio, N. Batalha, N. Siegler, & E. C. Tong (Eds.),  
 933 *Space telescopes and instrumentation 2018: Optical, infrared, and millimeter*  
 934 *wave* (Vol. 10698, p. 106985T). doi: 10.1117/12.2309439
- 935 Tian, Y., Herrick, R. R., West, M. E., & Kremic, T. (2023). Mitigating Power and  
 936 Memory Constraints on a Venusian Seismometer. *Seismological Research Let-*  
 937 *ters*, 94(1), 159–171. doi: 10.1785/0220220085
- 938 Trahan, A. J., & Petculescu, A. (2020). Absorption of infrasound in the lower and  
 939 middle clouds of Venus. *The Journal of the Acoustical Society of America*,  
 940 148(1), 141–152. doi: 10.1121/10.0001520
- 941 Van Zelst, I. (2022). Comment on “Estimates on the frequency of volcanic erup-  
 942 tions on Venus” by Byrne & Krishnamoorthy (2022). *Journal of Geophysical*  
 943 *Research: Planets*, 127(12), e2022JE007448. doi: 10.1029/2022JE007448
- 944 Van Zelst, I., Maia, J., Plesa, A.-C., Ghail, R., & Spühler, M. (2024). Estimates on  
 945 the possible annual seismicity of Venus [preprint]. *EarthArXiv*. doi: 10.31223/  
 946 X5DQ0C
- 947 Walter, F., Gräff, D., Lindner, F., Paitz, P., Köpffi, M., Chmiel, M., & Fichtner,  
 948 A. (2020). Distributed acoustic sensing of microseismic sources and wave  
 949 propagation in glaciated terrain. *Nature communications*, 11(1), 2436. doi:  
 950 10.1038/s41467-020-15824-6
- 951 Wang, H. F., Zeng, X., Miller, D. E., Fratta, D., Feigl, K. L., Thurber, C. H., &  
 952 Mellors, R. J. (2018). Ground motion response to an ML 4.3 earthquake using  
 953 co-located distributed acoustic sensing and seismometer arrays. *Geophysical*  
 954 *Journal International*, 213(3), 2020–2036. doi: 10.1093/gji/ggy102
- 955 Widemann, T., Straume-Lindner, A. G., Ocampo, A., Voirin, T., Carter, L., Hens-  
 956 ley, S., ... Dumoulin, C. (2022). EnVision: a nominal science phase spanning  
 957 six Venus sidereal days (four earth years). In *Agu fall meeting abstracts* (Vol.  
 958 2022, pp. P55B–05).
- 959 Wilson, C. F., Zetterling, C.-M., & Pike, W. T. (2016). Venus long-life surface pack-  
 960 age. White paper submitted in response to ESA’s call for new scientific ideas.  
 961 *arXiv e-prints*, arXiv:1611.03365. doi: 10.48550/arXiv.1611.03365
- 962 Xu, Z., Broquet, A., Fuji, N., Kawamura, T., Lognonné, P., Montagner, J.-P., ...  
 963 Banerdt, W. B. (2023, April). Investigation of Martian regional crustal struc-  
 964 ture near the dichotomy using S1222a surface-wave group velocities. *Geophysi-*  
 965 *cal Research Letters*, 50(8), e2023GL103136. doi: 10.1029/2023GL103136
- 966 Zhan, Z. (2020). Distributed acoustic sensing turns fiber-optic cables into sensitive  
 967 seismic antennas. *Seismological Research Letters*, 91(1), 1–15. doi: 10.1785/  
 968 0220190112
- 969 Zharkov, V. N. (1983, October). Models of the internal structure of Venus. *Moon*  
 970 *and Planets*, 29(2), 139–175. doi: 10.1007/BF00928322